Engineering J-Aggregate Cavity Exciton-Polariton Devices

by

M. Scott Bradley

S.B., Massachusetts Institute of Technology (2004)
M.Eng., Massachusetts Institute of Technology (2006)

Submitted to the Department of Electrical Engineering and Computer Science
in partial fulfillment of the requirements for the degree of

Doctor of Philosophy in Electrical Engineering

at the

MASSACHUSETTS INSTITUTE OF TECHNOLOGY

June 2009

Author . . . . . .
Department of Electrical Engineering and Computer Science
May 5, 2009

Certified by . . . . . .
Vladimir Bulović
Associate Professor
Thesis Supervisor

Accepted by . . . . . .
Terry P. Orlando
Chair, Department Committee on Graduate Students

Engineering J-Aggregate Cavity Exciton-Polariton Devices

by

M. Scott Bradley

Submitted to the Department of Electrical Engineering and Computer Science
on May 5, 2009, in partial fulfillment of the
requirements for the degree of
Doctor of Philosophy in Electrical Engineering

Abstract

Research efforts in solution-based dye lasers and organic light-emitting devices (OLEDs) have led to advances in materials engineering and fabrication technology, propelling the field of organic solid-state photonics. Active areas of photonic research in organic systems include solid-state lasers (in both VCSEL and DFB form factor), low-threshold optical switches, and photodetectors. In all of these areas, thin films of "Jelley aggregates," or J aggregates, offer a promising materials platform thanks to their narrow linewidth and high oscillator strength at room temperature, properties resulting from delocalization of excitations across multiple strongly-coupled molecules. By placing these films in an optical microcavity, the aggregates exhibit additional strong-coupling to the cavity electric field, creating light-matter quasi-particles known as exciton-polaritons, even at room temperature. In this thesis, I discuss my research on the properties of J-aggregate thin films and on advancing the device and materials engineering of strongly-coupled devices based on J-aggregate thin films to the level of those in inorganic semiconductor systems. Exciton-polariton systems have been extensively studied at cryogenic temperatures in II-VI and III-V semiconductor quantum well systems in the past two decades as potential low-threshold VCSELs. J-aggregate-based exciton-polaritons systems, however, offer many device and engineering challenges, including: understanding the role of inhomogeneous vs. homogeneous broadening in the J-aggregate optical response, fabricating higher-quality microcavities with the ability to pump the polaritons at high intensities, and lateral patterning on the single-micron scale of organic microcavities. These topics are addressed and the outlook of organic exciton-polariton device research discussed.

Thesis Supervisor: Vladimir Bulović
Title: Associate Professor

Acknowledgments

The funding for the work in this thesis was provided by a National Defense Science and Engineering fellowship, seed grants from DARPA, funding from the MIT Institute for Soldier Nanotechnologies, and NSF MRSEC grants. In addition to the growth and testing facilities of the Bulović group (Lab of Organic Optics and Electronics, or LOOE), the shared analytical labs of the Center for Materials Science and Engineering (CMSE) were utilized extensively along with the facilities of the Microsystems Technology Labs (MTL) at MIT.

First, I would like to thank my thesis committee members, Prof. Franz Kaertner and Prof. Rajeev Ram, for their valuable feedback in the course of preparing this thesis. I would like to thank the members of the Bulović group with whom I have worked over the last several years for their feedback and friendship; I could not have hoped for a better group of colleagues. I am deeply indebted to Dr. Jonathan Tischler, my predecessor, mentor, and colleague who established this project in the LOOE group and helped in my transition from UROP to graduate student; he has always been ready to share some scientific insight to inform my engineer's perspective and engage in spirited discussions about strong coupling. I am additionally grateful to my advisor, Prof. Vladimir Bulović, who I have known since my undergraduate years at MIT and have been fortunate to assist as a teaching assistant; he has a contagious passion for creativity and curiosity, which I hope to emulate.

Additionally, I am grateful to Lisa Marshall and Sid Creutz of the Bawendi group for helping me with initial attempts at collecting angle-resolved photoluminescence with their custom microscope setup and Elizabeth Young of the Nocera group for the variable pump-power measurements in Chapter 4. I would like to thank Prof. Arto Nurmikko's group at Brown University for their fruitful collaboration early on in investigating J-aggregate dynamics, especially Dr. Qiang Zhang and Tolga Atay who collected the pump-probe data as noted in Chapter 2. Kurt Broderick at the MTL provided considerable help in making PDMS molds, and Libby Shaw in the CMSE was of great help in advising AFM and spectrometer use for the J-aggregate

thin film measurements.

Finally, on a personal note, none of this could have been even remotely possible without the support and love over the years of my family. My parents may not have understood what I've been studying the last decade and a half or so since I started algebra, but their support has been unwavering and their own intellectual enthusiasm a model that I hope to pass on to my children; I love them dearly and will carry their spirit with me for the rest of my life. I thank my brother and grandparents for reminding me of what's really important in life. And lastly, I want to thank my wife, Corinne, the love for whom I cannot really put into words. I am so grateful to have had her with me on the journey through MIT and look forward to our future adventures together; her intellectual strength and perspective keep me looking ahead and trying to be a better person.

Contents

List of Figures

Chapter 1

Introduction: Device Physics and Theory of Operation

This thesis explores the engineering of solid-state photonic devices based on organic active layers. Specifically, organic photonic devices utilizing a material known as "J aggregates" of cyanine dyes are demonstrated and characterized, their potential for use as lasers is investigated, and patterning methods are developed that enable the integration of organic active materials in photonic systems.

Since the invention of the laser in the 1960s, the field of photonics has undergone many phases of development as new technologies were invented and some inevitably discarded or sidelined. In the 1970s, considerable research in solution-based dye lasers led to the development of laser dyes covering the visible spectrum and possessing remarkable quantum efficiencies (i.e., efficiency of converting input pump power into luminescence) and stabilities. The shortcomings of solution-based dye lasers are mostly in construction and limitations on stability due to the use of solvents. The use of solution-based dye limits construction to free-space tabletop setups, and the use of solvents significantly limits packaging options to eliminate photodegradation due to oxidation. Nevertheless, today one can still purchase laser dye systems for use in research in spectroscopy, ultrashort laser pulse generation, or other applications where large gain bandwidth is desirable.

In the later development of organic light-emitting devices (OLEDs) in the 1980s

and 1990s, the laser dyes developed for solution-based lasers would find commercial applications in the solid state (i.e., in thin films) as light-emitting dopants, capturing energy from excitons formed at organic heterojunctions through Förster resonant energy transfer (FRET). A thorough review of the materials science and physics of organic optoelectronics, including the physics of Frenkel excitons in organic materials and FRET, can be found in Pope and Swenberg [148].

Concurrent with the development of OLED technology, solid-state photonics based on inorganic semiconductors saw rapid development. Microfabrication technologies such as molecular beam epitaxy enable ultrapure, precise-thickness layers of inorganic semiconductors to be grown in device structures (in this thesis referred to as "inorganic" to distinguish from the organic semiconductors used in OLEDs). These development efforts have enabled electrically-pumped diode lasers based on quantum wells of inorganic semiconductors at many wavelengths from the visible to infrared. Many excellent texts reviewing the physics of semiconductor photonics exist, two of which are Coldren and Corzine [39] and Chuang [37].

Beginning in 1992, Weisbuch *et al.* initiated a new phase of research in solid-state lasers based on the phenomenon of strong coupling of light and matter [196]. This research was itself motivated by the investigation of strong light-matter coupling between atoms and cavities in the 1980s [88]. Weisbuch *et al.* demonstrated that when layers of inorganic semiconductors were deposited between two highly reflective mirrors in a monolithic stack (i.e., a "microcavity," or a cavity on the size scale of one or a few wavelengths of light), the usual single reflectivity dip of the cavity changed to a doublet, indicating that the Wannier-Mott exciton transition in the semiconductor was strongly coupled to the microcavity electric field. In the past decade, the efforts spurred by the results of Weisbuch *et al.* realized the first demonstrations of lasers based on cavity exciton-polariton states in inorganic systems [15, 35, 36, 50, 76]. Except for the GaN inorganic systems, the II-VI systems (CdTe) and III-V systems (GaAs) demonstrated both require cryogenic temperatures due to the low binding energy of excitons in those systems (i.e., at 300 K, $k_BT \approx 26$ meV, which is higher than the binding energies of excitons in CdTe and GaAs). This was noted by Saba *et al.*

[154] in a discussion of potential platforms for realizing room-temperature exciton-polariton parametric amplification.

One such potential platform is based on organic materials, where the Frenkel model is used to describe excitons as opposed to the Wannier-Mott model in inorganic systems. Since Frenkel excitons are localized to a molecule, their binding energy is considerably higher than room temperature. Since the demonstration of Lidzey *et al.* [104] of strong coupling in a microcavity containing a solid-state organic dye, efforts have been underway, of which this thesis is a part, to make exciton-polariton devices in organic systems, where the strong coupling is between the microcavity electric field and the Frenkel excitons in the organic active material.

Since the work of Lidzey *et al.* [104], the most significant breakthrough in the field of organic exciton-polariton devices was the demonstration of electroluminescence (EL) from exciton-polaritons in the work of Tischler *et al.* [189], which was the first demonstration of EL from any exciton-polariton device, organic or inorganic (the first inorganic exciton-polariton EL was not demonstrated until several years later). Overall, though, research efforts in organic exciton-polariton systems have been mostly focused on demonstrating reflectivity or PL from microcavities with very low to low quality factors (Q on the order of 10-200, leading to cavity photon lifetimes in the range of tens to a few hundreds of femtoseconds) and using different organic materials. The cavity designs utilized have been limited almost exclusively to all-metal or metal-DBR planar microcavities, where one of the mirrors is metallic and the other composed of a dieletric Bragg reflector (DBR) [63–65, 105, 107, 189]. In addition, in the few cases where a double-DBR microcavity was used, the devices still suffered from inhomogeneities due to the thick active layer used, which causes broadening of the polariton linewidths due to the different spatial overlap of the cavity electric field with the active material in the cavity [40, 83]. Finally, the choice of active material, and type of J aggregate in particular, has been largely arbitrary, without much consideration of how to pump the finished devices or how to minimize photobleaching of the active layer.

In this thesis, the above device and materials engineering issues will be addressed

in order to bring organic exciton-polariton device engineering onto the same technical level as that of inorganic exciton-polariton devices. By advancing these aspects of device and materials engineering of organic exciton-polaritons, I will demonstrate how the same analytical tools (detailed angular-resolved PL, high pump powers) can be applied to organic exciton-polariton devices and yield information about the dynamics of exciton-polaritons in organic systems. Chapters 2 and 3 will investigate the optical and morphological properties of J-aggregate thin films and the linear optical properties of J-aggregate exciton-polariton microcavity devices in order to determine the extent of inhomogeneous vs. homogeneous broadening in the linewidths of the J-aggregate and exciton-polariton optical response, which is a key figure in simulating the dynamics of microcavity exciton-polaritons. Chapter 4 will demonstrate the steps taken to address the device and engineering issues discussed above, and finally, in Chapter 5, a method will be demonstrated for lateral patterning of organic microcavities on the single-micron scale, which will enable the fabrication of 0D organic exciton-polariton devices, similar to those recently demonstrated for inorganic exciton-polaritons [12, 55, 56, 184].

In the next sections of this chapter, the strong coupling of light and matter in solid-state systems will be discussed, leading to the specific case of strong coupling in organic systems using "J aggregates" of cyanine dyes. Following that section, the physics of "J aggregates" will be covered, leading finally to a discussion of the theory of operation of exciton-polariton lasers.

1.1 Exciton-Polaritons

The physical theory behind exciton-polaritons is itself not recent. The exciton-polariton description of light in a semiconductor was first described by Hopfield in 1958 [67]. Since the research on cavity exciton-polaritons initiated by Weisbuch *et al.* was itself an offshoot of atomic research, where the splitting of the cavity mode due to interactions with atomic transitions is referred to as "normal-mode coupling," or NMC, exciton-polariton phenomena in solid-state systems are sometimes referred to

in literature as NMC (e.g., see Khitrova *et al.* [86, 87]). This distinction is becoming more important as true strong coupling between a single solid-state transition dipole (e.g., that of a quantum dot) and a microcavity electric field has been recently demonstrated [57]. Nevertheless, the use of the more strict term in atomic physics of "strong coupling" is often used interchangeably with NMC in exciton-polariton literature, and in this thesis the term "strong coupling" will be used to refer to exciton-polariton phenomena. The brief review that follows will give a general description of polaritons, focusing specifically on those formed by the coupling of two-level systems with an electric field, followed by a discussion of the specific properties of exciton-polaritons in cavities that are of interest in device applications and the current state of research in the field.

1.1.1 Single Two-Level System Interacting with the Electric Field

Let use first consider the interaction of a single two-level system with an electric field. The Hamiltonian describing this interaction was first outlined by Jaynes and Cummings [71]. Using the notation from Kimble [88], the Hamiltonian of an electric field coupled to N_s two-level systems is:

$$\hat{H}_s = \hat{H}_A + \hat{H}_F + \hat{H}_I$$

where the two-level system ($\hat{H}_A$), electric field ($\hat{H}_F$), and interaction ($\hat{H}_I$) Hamiltonians are (using the rotating wave approximation, meaning that non-energy-conserving terms are neglected [38, 79]):

$$\hat{H}_A = \frac{\hbar\omega_A}{2}\sum_{\ell=1}^{N_s}\hat{\sigma}_\ell^z$$

$$\hat{H}_F = \hbar\omega_{cav}\hat{a}^\dagger\hat{a}$$

$$\hat{H}_I = i\hbar\sum_{\ell=1}^{N_s}\left[g\left(\vec{r_\ell}\right)\hat{a}^\dagger\hat{\sigma}_\ell^- - g^*\left(\vec{r_\ell}\right)\hat{a}\hat{\sigma}_\ell^+\right]$$

The resonant frequencies of the two-level system and electric field (for our purposes, usually a cavity) are ω_A and ω_{cav}, respectively. $\hat{\sigma}_\ell^z$, $\hat{\sigma}_\ell^+$, and $\hat{\sigma}_\ell^-$ are the population inversion, raising, and lowering Pauli operators for the ℓ^{th} two-level system (i.e., each of which is fermionic). The creation and annihilation operators for the electric field are $\hat{a}^\dagger$ and $\hat{a}$, respectively. Finally, the coupling term for each two-level system to the electric field is given by g, where for a single two-level system:

$$g\left(\vec{r_\ell}\right) = \left(\frac{\mu^2 \omega_{cav}}{2\hbar\epsilon_0 V_m}\right)^{\frac{1}{2}} \psi\left(\vec{r_\ell}\right) \equiv g_0 \psi\left(\vec{r_\ell}\right)$$

Kimble [88] includes in the above definition of the coupling term a cavity-mode function, $\psi\left(\vec{r_\ell}\right)$, that provides a spatial dependence of the coupling, which is normalized such that the cavity modal volume is equal to the integral of this spatial function in three dimensions ($V_m = \int \left|\psi\left(\vec{r}\right)\right|^2 dV$). This function is especially important in atom cavity systems where a gas of atoms is placed into a macroscopic spherical microcavity. In solid-state microcavity systems, this parameter is still important since the active layer (i.e., quantum wells or organic molecules) may vary slightly in position from sample to sample, which would ultimately affect the degree of coupling of the light-matter system.

It is important to note that although many two-level systems (N_s) are present in the above Hamiltonian, they are considered to be acting separately without any *cooperativity*, meaning they are not forming any coherent polarization. When this Hamiltonian is diagonalized, the eigenfrequencies of this Hamiltonian are dependent on the number of photons present in the modal volume. Inside each manifold of states, which are centered around the total number of excitations (in the resonant case where $\omega_A = \omega_{cav} = \omega_0$, these are $n\hbar\omega_0$, where n is the number of photons), the sublevels are separated by $\sqrt{n}\hbar g_0$. Therefore, when considering the optical response of such a coupled system, four possible transition frequencies are available from one manifold to another; two of these, however, are nearly degenerate, leading to the observation of the "Mollow triplet" in the optical response [79]. The "Mollow triplet" has been recently observed in single-molecule resonance fluorescence in the solid state [199].

Physically, as more excitations are placed into the electric field, the electric field exchanges energy with the single dipole at a faster and faster rate. This rate of energy exchange is known as the "Rabi frequency," named after the physicist I.I. Rabi and the semiclassical model developed for the interaction of a classical electric field with a quantum two-level system [62]. It is important to note that Rabi oscillations will only occur if the rate of energy exchange between the electric field and single two-level system is faster than the rate at which coherence is lost by the electric field (e.g., in a cavity, this is the rate at which photons escape through the mirrors) or by the two-level system (e.g., through collisions with phonons in solid-state systems–especially in solid-state systems, this coherence lifetime is rarely set by the energy decay rate from the two-level system, but instead the lifetime is limited by interactions within the environment of the solid). In the notation of Kimble [88], the cavity loss rate is given by κ and the decoherence rate of the two-level system by the parameter γ; the condition of strong coupling for a single two-level system requires $g_0 \gg \kappa, \gamma$. Recently, the Jaynes-Cummings ladder was directly probed for a superconducting qubit placed into a planar waveguide resonator in a setup that has been dubbed circuit quantum electrodynamics (QED) [59].

1.1.2 Multiple Two-Level Systems Interacting Cooperatively with the Electric Field

Next, let us consider what happens when instead of having a single transition dipole forming a polarization response, there are a very large number of dipoles. Just as the Rabi frequency increased when multiple photons were placed in the electric field, the Rabi frequency also increases when multiple transition dipoles are present in the same electric field mode acting cooperatively. The Jaynes-Cummings Hamiltonian was first considered in the many-two-level-system case by Tavis and Cummings [185]. Simply put, when multiple two-level systems are present in the modal volume of the electric field, they form a coherent polarization response that is the sum of all of the individual polarizations. The effect on the coupling parameter, g, is that it is

increased by the number of two-level systems, N_s present:

$$g = \left(\frac{N_s \mu^2 \omega_{cav}}{2\hbar\epsilon_0 V_m}\right)^{\frac{1}{2}} = \sqrt{N_s} g_0$$

The resulting eigenvalues for the first manifold's energies (assuming zero detuning, meaning that $\omega_A = \omega_{cav} = \omega_0$, are [88]:

$$\omega_{\pm} = \omega_0 - i\left(\frac{\kappa + \gamma}{2}\right) \pm \left[g_0^2 N_s - \left(\frac{\kappa - \gamma}{2}\right)^2\right]^{\frac{1}{2}} \tag{1.1}$$

These levels are split by the "vacuum Rabi splitting," which derives its name from the fact that even with only one photon the energy levels are split.

In the limit of very large N_s, the presence of one or a few photons (n small) does little to affect the light-matter coupling since $N_s \gg n$, despite the fact that the individual matter components of the coupled system are saturable. In essence, instead of acting as fermions, where adding excitations would lead to energy-level changes through Pauli exclusion, the two-level systems in this limit are bosonic. The result of this bosonic behavior is that the manifolds for one or a few photons contain states that are equally separated in energy. The allowed transitions between manifolds in the bosonic limit therefore consist only of two energies (since the splitting is determined only by N_s), leading to a "Rabi doublet" in the optical response of the coupled system [79]. Physically, the electric field is interacting with all of the transition dipoles present within the modal volume simultaneously, and as more dipoles are present, the rate of exchange of energy between the dipoles and the electric field increases. Figure 1-1 summarizes the ladder of states in the two limits.

An important detail of this interaction is that the energy exchange between the dipoles and electric field is occurring simultaneously amongst all of the transition dipoles–the energy is delocalized amongst all of the dipoles that are coherently coupled to the electric field. This polarization wave in the material is in essence a particle whose size is dictated by the modal volume of the electric field. Due to this energy delocalization, the quasi-particle that consists of the electric field mode (i.e., the photon) coupled to the numerous transition dipoles is referred to as a "polariton." In

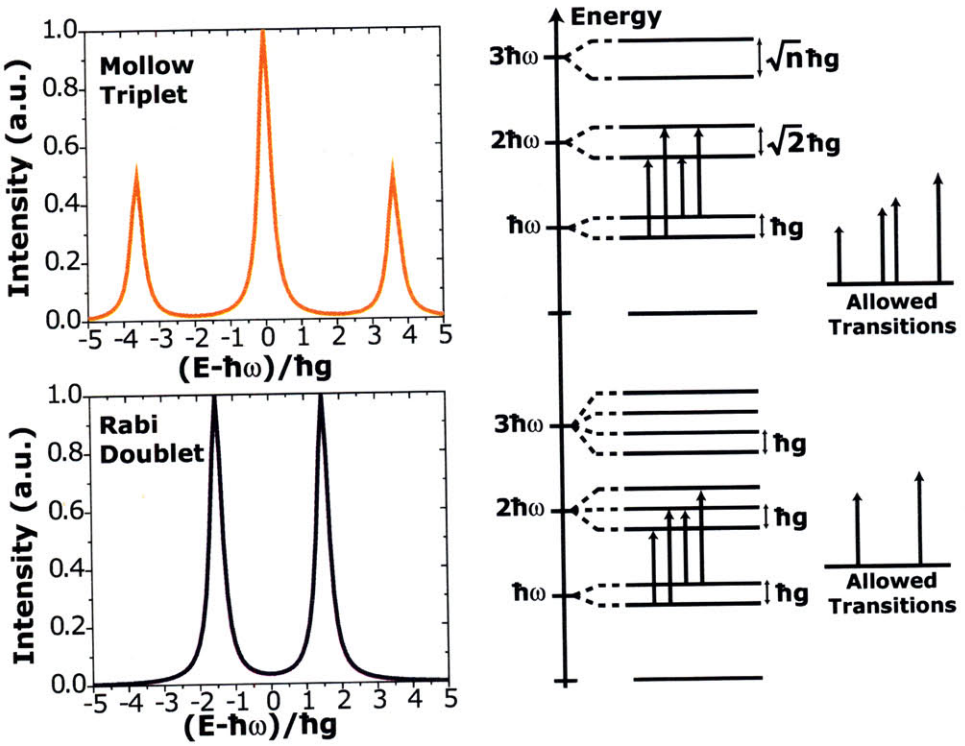

Figure 1-1: Ladder of energies and allowed transitions for limit of single two-level system (fermionic, top) and very large number of two-level systems (bosonic, bottom) [79].

general, the polariton picture of light interacting with many transition dipoles does not require that the transition dipoles be saturable (i.e., two-level systems). Any type of dipole in a medium can serve as the matter part of a polariton. In this thesis, the topic of discussion will specifically be "exciton-polaritons," where the matter component of the polariton is comprised of exciton transition dipoles (which often can be modeled as two-level systems). The saturable nature of the matter component of a polariton only affects the behavior of the polaritons at high densities (i.e., in the nonlinear regime).

1.1.3 The Polariton Picture

Looked at from the perspective of Maxwell's equations, a polariton is simply quantum mechanical quasi-particle that represents a quantum of the polarization of light in a medium. Specifically, a polariton picture describes the limiting case in which the interaction of light with the medium is stronger than the dephasing processes which would otherwise destroy the light-matter coherence. It is important to note here that the matter component of the polariton *does not have to be a two-level system.* The example described above of a polariton comprised of light and N two-level systems (e.g., transitions in atoms or molecules) is merely a subset of the many types of polaritons that are possible.

When an electromagnetic (EM) wave is incident upon a medium, a polarization in the medium is created that opposes the applied electric field. If the medium has a strong response to the incident wave (i.e., dipoles in the medium are resonant or nearly resonant with the incident EM wave, and the combined strength of the dipoles is large enough), there will be a large polarization induced in the medium. However, this varying polarization in the medium will itself produce a magnetic field, as described by Ampere's law, which then in turn creates an electric field via the coupling in Maxwell's equations. If the response of the medium is not too dephased from the incident field by other interactions with the environment, the medium will coherently radiate its energy back into the exciting field, which then induces a polarization in the medium, and so on. Essentially, the material absorbs, reemits, and then reabsorbs

the same photon. Since an observer cannot state definitively whether the energy in the system exists as a photon or as polarization in the medium, the energy is instead stored in both at the same time, creating a quasi-particle consisting of part photon and part material polarization, a polariton.

Notably, any electric dipole in a material can comprise part of a polariton as long as the conditions referred to above are met: the combined strength of the medium's electric dipoles must be large enough such that their interaction with light occurs faster than competing dephasing processes in the material. Aside from the transition dipole in excitons, other examples of dipoles which can comprise part of a polariton are optical phonons (e.g., in sodium chloride salt crystals, if Na and Cl ions move in opposite directions within the unit cell, then they form an optical dipole which can interact with an EM wave) and plasmons (e.g., surface plasmons in silver films). Due to the strong coupling between light and matter, a band gap in the optical dispersion relation opens at the resonance frequency of the material's dipole [58, 141]. Figure 1-2 shows a typical dispersion relation for a bulk polariton, where the unconfined electric field interacts with a dipole in a material [52]. Specifically, the dispersion relation shown is that of a phonon-polariton. This dispersion relation is the result of coupling two harmonic oscillators (i.e., mathematically the same in the linear regime as the bosonic limit of the coupled light and N two-level systems described above). The two resonances that result from the coupling of the transverse optical phonon to light are (in cgs units)[52]:

$$\omega_{\pm}^2 = \frac{1}{2\epsilon(\infty)}\left(\omega_T^2\epsilon(0) + c^2K^2\right) \pm \left(\frac{1}{4\epsilon(\infty)^2}\left(\omega_T^2\epsilon(0) + c^2K^2\right)^2 - \omega_T^2K^2\frac{c^2}{\epsilon(\infty)}\right)^{\frac{1}{2}} \quad (1.2)$$

where $\omega_{\pm}$ are the frequencies of the phonon-polariton modes, ω_T is the frequency of the transverse optical phonon (which is coupling to the light), $\epsilon(\infty)$ and $\epsilon(0)$ are the permittivities of the material at DC and higher frequencies, respectively, K is the momentum of the photon/polariton (which gives the light line in the material according to the adjusted dispersion relation $\omega = \frac{cK}{\sqrt{\epsilon(\infty)}}$), and c is the speed of light.

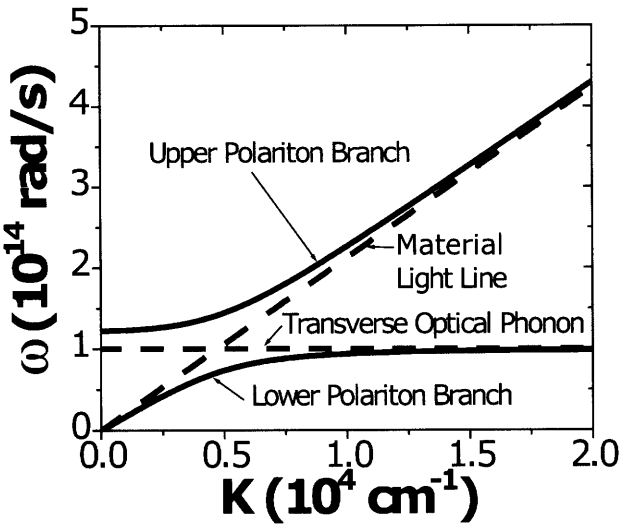

Figure 1-2: Dispersion of phonon-polariton energy vs. momentum [52]. $\epsilon(0) = 3$, $\epsilon(\infty) = 2$, and $\omega_T = 10^{14}$ rad/s. The light line in the material is $\omega = \frac{cK}{\sqrt{\epsilon(\infty)}}$.

Anti-crossing occurs around the dipole resonance as the light line approaches the resonance frequency, resulting in lower and upper branches of the polariton dispersion separated by a band gap.

Cavity polaritons (sometimes termed microcavity polaritons in the case of wavelength-sized cavities to distinguish them from larger free-space configurations) share many of the same characteristics as bulk polaritons, but the adjusted dispersion relation of the electric field due to the cavity results in some important distinctions in the polariton dispersion. These distinctions affect the dynamics of cavity polaritons and therefore the types of devices that can be built with cavity polaritons. Most importantly, the photonic part of the polariton differs in the case of cavity polaritons from the case of bulk polaritons.

In a bulk polariton, the matter is coupled to unconfined light, which has a linear dispersion relation extending to zero energy (the light line is given by $\omega = ck$ in free-space or $\omega = \frac{c}{n}k$ in a material with index of refraction n). The boundary conditions imposed by the cavity, however, introduce a cutoff frequency in the photonic part of a cavity polariton, meaning that when a cavity polariton relaxes, it will settle to

a minimum energy in the lower branch as opposed to continuously relaxing to zero energy. Additionally, the lower polariton branch, due to this minimum in the cavity energy, will have a portion that is inside the light line, meaning that excitations from the lower polariton branch are accessible externally (one of the consequences of this is that cavity exciton-polaritons in the lower branch can radiate either within the cavity or into free space, whereas bulk exciton-polaritons from the lower branch must somehow scatter into a state within the light line that can then radiate into free space or even into the bulk). Mathematically, the dispersion of planar cavity energies versus angle is that of a parallel-plate waveguide; for a mode to be supported in the waveguide, the constructive interference condition in the direction normal to the plates must be maintained. The wave-vector of light in the cavity can be broken down into components perpendicular and parallel to the mirrors:

$$\left|\vec{k}\right|^2 = k_{\parallel}^2 + k_{\perp}^2$$

The perpendicular component of the wave-vector and total magnitude of the wave-vector can be be related to the normal-mode cavity resonance energy and resonance energy at a given angle, respectively. Assuming that the effective index of refraction of the cavity is n_{cav} and making these substitutions gives:

$$\frac{\omega(\theta)n_{cav}}{c} = k_{\parallel}^2 + \frac{\omega(0°)n_{cav}}{c}$$

The parallel component of the wave-vector can be related to the external angle at which a cavity is probed (e.g., in a reflectance measurement). In the coupled light-matter system, the in-plane wave-vector (or momentum) of the polariton likewise can be related to the angle of light incident upon the system (where the angle, θ, is measured from the surface normal) through the same equation:

$$\hbar k_{\parallel} = \hbar k_0 \sin\theta = \frac{\hbar\omega(\theta)}{c}\sin\theta \tag{1.3}$$

Plugging this into the equation relating $\omega(\theta)$ and $\omega(0°)$ and solving for $\omega(\theta)$ gives:

$$\omega(\theta) = \frac{\omega(0^\circ)}{\sqrt{1 - \frac{\sin^2\theta}{n_{cav}^2}}} \tag{1.4}$$

Eq. 1.4 is then plugged into a solution similar to Eq. 1.1 [79]:

$$E_L^U(\theta) = \frac{1}{2}\left(E_{ex} + E_{cav}(\theta)\right) \pm \frac{1}{2}\sqrt{[E_{ex} - E_{cav}(\theta)]^2 + 4\hbar^2 g} \tag{1.5}$$

where g is the coupling between cooperative exciton transitions and cavity photons. Comparing Eq. 1.5 to the semiclassical results of light coupled to a two-level system, the Rabi frequency Ω_R is related to the coupling coefficient g by $\Omega_R = 2g$. We can then write a generalized Rabi frequency $\Omega^2 = (\Omega_R^2 + (\omega_{ex} - \omega_{cav})^2)$ and incorporate the homogeneous linewidths of the cavity and exciton, γ_{cav} and γ_{ex}, respectively, into the equation as the imaginary parts of the respective energies, resulting in the general dispersion of the modes that is the same as for the multi-two-level-system case in Eq. 1.1 [79]:

$$E_L^U(\theta) = \frac{1}{2}\left(E_{ex} + E_{cav}(\theta) - i\gamma_{cav} - i\gamma_{ex}\right) \pm \frac{1}{2}\sqrt{\hbar^2\Omega^2 - (\gamma_{cav} - \gamma_{ex})^2} \tag{1.6}$$

The significance of the above expression is that having a continuum of electric field modes results in a continuum of coupled systems; each mode is coupled independently to the excitonic resonance, and the two branches are simply the two continuums of coupled states differing slightly in energy and momentum. As will be discussed later in the context of exciton-polariton lasers, once an exciton-polariton is formed in one of the polariton branches, the excitation can scatter from coupled system to coupled system along the branch and even into uncoupled excitonic states (which are present in the polaritonic bandgap between the two branches). Figure 1-3 shows a typical angular dispersion relation for cavity exciton-polaritons, where the exciton energy vs. momentum dispersion is assumed to be flat and the cavity dispersion is that derived in Eq. 1.4 (the two branches are given by Eq. 1.6).

Due to the minimum in energy in the cavity dispersion (i.e., light modes below

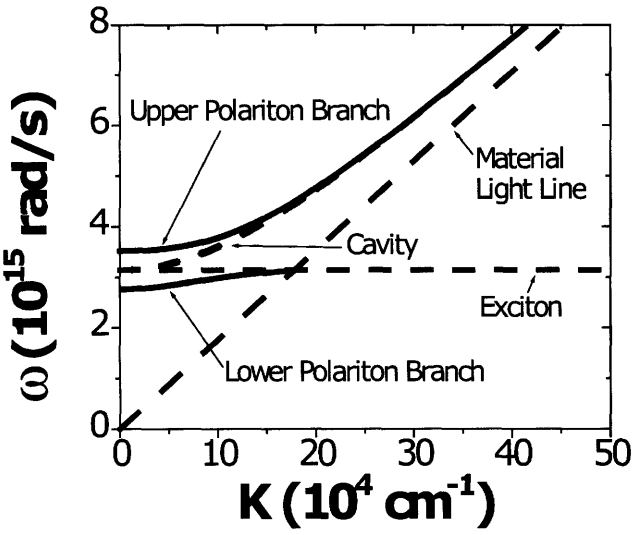

Figure 1-3: Dispersion of microcavity exciton-polariton energy vs. momentum. Rabi splitting $\hbar\Omega_R = 250$ meV, exciton resonance free-space wavelength $\lambda = 600$ nm, and background index of refraction of the cavity material $n_{cav} = 1.7$. The light line in the cavity material is $\omega = \frac{cK}{n_{cav}}$.

a certain energy, or frequency, do not exist in the cavity), the dispersion of cavity polaritons also has a minimum in energy. The result of this minimum energy in the system is that the cavity polariton population might be able to form a quasi-thermal-equilibrium condensate if intrabranch relaxation rates are fast enough. The use of this phenomenon as a potential source of coherent light will be discussed in Section 1.2.

1.2 Theory of Operation: Exciton-Polariton Laser

Shortly after the first report of strong coupling in a microcavity by Weisbuch *et al.* [196], Imamoglu *et al.* [70] suggested that a new type of laser could be made that utilized the bosonic properties and relatively large spatial extent (or low effective mass) of exciton-polaritons. This laser would take advantage of a "boser" effect in which a build-up of population in the lower-branch minimum at $k = 0$ would stimulate the relaxation of other exciton-polaritons into the same state. The result

of this "final-state stimulation" would be a massive, coherent population of exciton-polaritons at the lower-branch minimum; due to the coherence of the population, any light decaying out of this massive population through the cavity mirrors would by definition be coherent, thus resulting in the same type of coherent light output provided by a traditional laser. The threshold of such a laser would be very low due to the need to only maintain excitation within the coherence domain of the photon. Very soon after the prediction by Imamoglu *et al.* [70], Pau *et al.* [144] presented evidence of something like polariton lasing that was later identified by Cao *et al.* [30] and Kira *et al.* [90] to be a photon laser in weak coupling (beyond the exciton saturation density at which a system switches from strong coupling to weak coupling) [11, 26].

While the above motivation for an exciton-polariton laser was developed with inorganic semiconductor quantum-wells in mind as the active medium, the same argument applies to making a laser in an organic exciton-polariton system, but the performance comparison should be made with other solid-state organic dye lasers instead of inorganic lasers.

In this section, we will review the fundamentals of a four-level laser and then of an exciton-polariton laser and compare the potential performances of both based on current literature. To maintain an even comparison, the traditional lasers considered will be restricted to those with a vertical-cavity surface-emitting laser (VCSEL) structure.

1.2.1 A Four-Level Laser

In order to make the most relevant comparison between the two types of lasers, we will specifically focus on four-level lasers, which dye lasers most closely resemble. Figure 1-4 shows a schematic of the theory of operation of a traditional, optically pumped laser.

A high-energy pulse resonant with the absorption line of a molecular gain medium pumps excitations from the molecular ground state. These excitations quickly relax to a lower-energy, long-lived excited state on the picosecond or sub-picosecond time

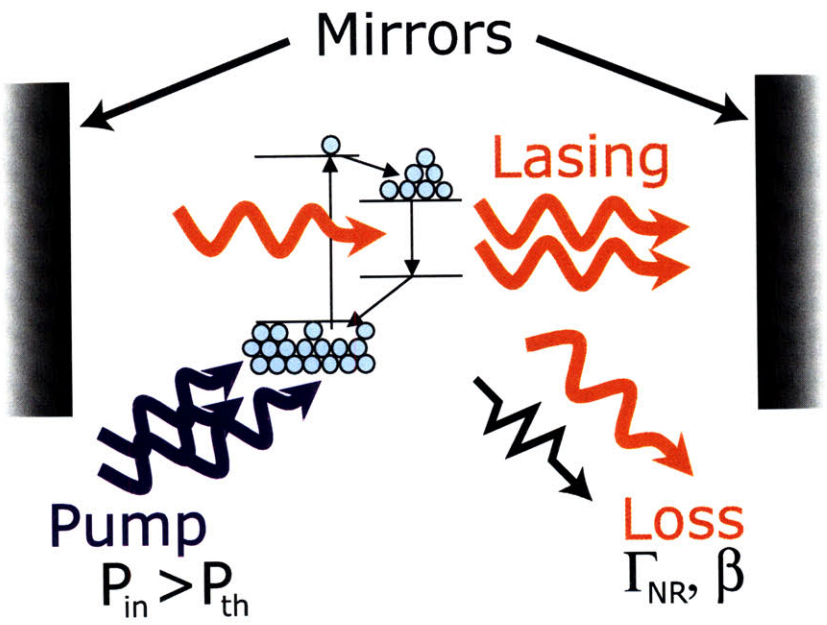

Figure 1-4: Schematic of theory of operation of a conventional, optically-pumped laser. When the gain medium (here a four-level system) is pumped at an input power greater than threshold ($P_{in} > P_{th}$), a lasing mode is established. The threshold is set by the mirror losses, gain provided by the laser medium, and internal losses due to non-radiative relaxation of excitations via heat (i.e., phonons, characterized by the rate Γ_{NR}) and radiative spontaneous emission into modes other than the lasing mode (characterized by the coefficient β; $\beta = 1$ means that all spontaneous emission goes into the lasing mode, whereas $\beta < 1$ means other modes exist for spontaneous emission).

scale via the release of phonons (or in the case of molecules, emit vibrations as a molecule undergoes a reorientation). The "ground state" associated with the reoriented molecule is at a slightly higher energy than the molecular ground state of the relaxed molecule and is therefore unpopulated except for thermal excitations. Thus, even for a single excitation, the four-level system is essentially inverted–if a photon in the cavity encounters the excitation, the excitation will be stimulated into the lasing photon mode. As mentioned earlier in the chapter, considerable research in the 1970s led to a large number of solvent-based dye lasers covering the entire visible spectrum, first operating as pulsed lasers and then even in CW (continuous wave). Peterson *et al.* [145] provides one of the first studies on calculating the laser threshold of an organic dye laser.

As shown in Figure 1-4, two important parameters in the analysis of laser structures and gain materials are β, the spontaneous emission coefficient, and Γ_{NR}, which is the rate of non-radiative losses in the gain material. The spontaneous emission outside of the lasing mode and non-radiative losses can be lumped together in Γ_{NR} to refer to any loss of excitation outside of the lasing mode, instead writing $\Gamma_{NR} = 1/\tau_{nr} + (1-\beta)\Gamma_s$, where τ_{nr} is the non-radiative lifetime due to non-radiative loss processes (e.g., phonons), and Γ_s is the spontaneous emission rate of the gain material [77].

The gain provided by the medium must overcome these material losses as well as cavity losses, which are caused by emission through the mirrors (the reflectivity of the mirrors must be balanced between keeping losses low but also allowing the generated light to exit the cavity; see Chuang [37] and Coldren and Corzine [39] for more on such design considerations).

For the purposes of comparing a traditional four-level laser to an exciton-polariton laser, we are most interested in comparing the threshold dependence of the two, and in computing the threshold, we especially want to know in what variable(s) the two systems differ. We begin with a greatly simplified model of the four-level system. For a more detailed model taking account of the dye self-absorption, see Peterson *et al.* [145]. In a cavity with $Q \leq 1000$ (typical for a planar cavity, especially if a metal

mirror is used), the lifetime of a photon is on the order of 1 ps or less due to mirror loss. Since the competing loss processes in the material are much slower (spontaneous and non-radiative processes in dye molecules at room temperature are usually on the order of 1 ns), we can assume all losses are due to the mirrors. The generation process can be approximated first by assuming a quantum efficiency $\eta = 100\%$, which assumes all pumped excitations arrive at the lasing transition upper level. With these two simplifications, the threshold is given by the pump power at which generation and mirror loss are equal [94, 155]:

$$1 = \frac{1/\tau_{cav}}{\sigma c N_{th}}$$

where τ_{cav} is the cavity lifetime, σ is the stimulated-emission cross-section of the dye molecules, ℓ is the length of the gain medium in the cavity, c is the speed of light, and N_{th} is the threshold density of excitation. Rearranging for N_{th}:

$$N_{th} = \frac{1}{c\tau_{cav}\sigma} \tag{1.7}$$

which says that the intensity required to achieve lasing depends inversely on the stimulated-emission cross-section of the dye molecule that comprises the gain medium and the loss rate of the cavity. To find the incident energy per area needed by an exciting laser, assuming that all light is absorbed, we first find the density of excitations needed per unit area by multiplying by the thickness of gain material used, ℓ. We then need to multiply by the pump photon energy, $\hbar\omega_P$, giving:

$$E_{th} = N_{th}\ell\hbar\omega_P = \frac{\hbar\omega_P\ell}{c\tau_{cav}\sigma} = \frac{\hbar\omega_P\ell 2\pi}{\lambda_0 Q\sigma} \tag{1.8}$$

where the substitutions $\tau_{cav} = Q/\omega$ and $\omega = c\frac{2\pi}{\lambda_0}$ were made, where λ_0 is the cavity (lasing) wavelength [192]. For a traditional four-level laser, such as the VCSEL dye laser demonstrated by Bulović *et al.* [25] utilizing the laser dye DCM doped into the host Alq_3, the threshold is set by the cross-section of the dye and the Q of the cavity. In the case of the structure shown by Bulović *et al.* [25], we can make a back-of-the-envelope calculation for the theoretical threshold in such a device. The

DCM emission cross-section was measured by Tagaya *et al.* [176] to have a peak of about $\sigma_{em} = 3 \times 10^{-16}$ cm^2. The cavity demonstrated had measured reflectances of $R_{DBR} = 0.995$ and $R_{Ag} = 0.91$, which with the assumed cavity length of $(5/2)\lambda_0/n$, gives a quality factor [39]:

$$Q = \frac{\omega L}{v_g \ln(1/R_1R_2)} = \frac{\omega(5/2)\lambda_0/n}{c/n \ln(1/R_1R_2)} = \frac{2\pi(5/2)}{\ln(1/R_1R_2)} \approx 160$$

Plugging these values into Eq. 1.8 gives an estimate for the threshold density for a pump at $\lambda_P = 337$ nm:

$$E_{th} \approx 110\ \mu\text{Jcm}^{-2}\text{pulse}^{-1}$$

which is near the observed threshold energy of 300 μJcm^{-2}pulse^{-1}. The additional energy is likely due to pump and relaxation losses not accounted for in the simple model (e.g., losses to other modes, amount of pump actually absorbed in film, etc.). The above calculation demonstrates that in comparing threshold densities of a traditional organic VCSEL to a potential exciton-polariton VCSEL, Eq. 1.7 can provide a reasonable threshold density for a traditional organic laser.

1.2.2 Exciton-Polariton Laser

Initial experiments in pursuing exciton-polariton lasers were concerned with bypassing the "bottleneck" present on the lower branch of the dispersion caused by the diminishing excitonic part of the quasi-particle (since only the excitonic part can interact with the environment to dissipate energy and cause the polariton to relax) [120, 173, 179, 182]. These experiments included resonantly pumping the lower branch in order to excite the state at $k = 0$ and a higher energy state and then observing amplification from the $k = 0$ state when a probe beam was applied [16, 17, 27, 153, 159, 166, 172, 183]. Additionally, nonlinear photoluminescence was observed from microcavity exciton-polariton systems when excited nonresonantly, suggesting the presence of stimulated relaxation processes [20, 21, 43, 164, 180, 181]. Together, these experiments provided strong evidence for the stimulated relaxation predicted by

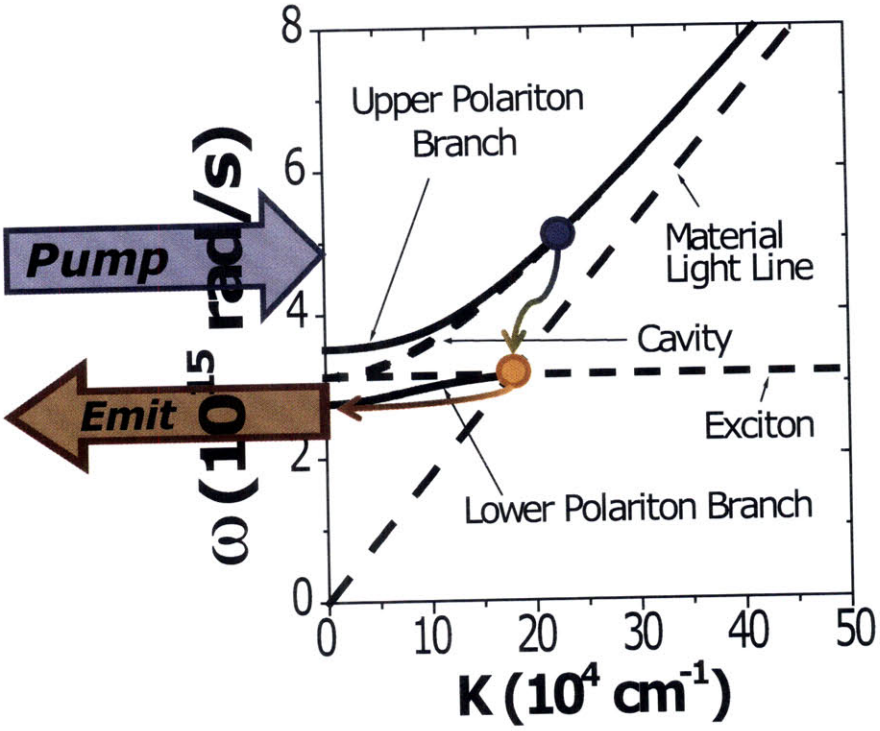

Figure 1-5: Schematic of theory of operation of non-resonantly-pumped exciton-polariton laser. Excitations are injected at high energy, after which they relax into an exciton reservoir from which the lower-branch exciton-polariton is excited. When the number of excitations at the $k = 0$ minimum in the lower branch is on average at least one, stimulated scattering into this mode produces a massive coherent population, the decay of which out of the cavity produces coherent light emission.

Imamoglu *et al.* [70] and motivated continued research to achieve exciton-polariton lasing.

Figure 1-5 shows a schematic of how a non-resonantly-pumped exciton-polariton laser operates.

The system is pumped far above the shared resonance of the cavity and exciton. These excitations can exist either as upper-branch exciton-polaritons or simply as uncoupled excitons. These excitations quickly relax via emission of phonons to the "exciton reservoir," which consists of uncoupled or only slightly coupled, large wavevector excitons. From this reservoir, excitons relax into the exciton-polariton lower branch and relax via phonon emission or polariton-polariton scattering to the $k = 0$ state. When the occupation of the $k = 0$ state becomes populated on average with at

least one excitation for all time, final-state stimulated scattering of exciton-polaritons into the lower branch massively populate the $k = 0$ state, creating a "polariton laser" (i.e., coherent light is emitted via decay of the coherent polariton population at $k = 0$).

In the past decade, two groups of theoretical physicists have led the way in studying the many-body physics of polariton lasing. Early on, Eastham and Littlewood [54] used the Dicke model, which considers a collection of fermionic two-level systems, to demonstrate that a polariton laser could in fact be the result of a Bose condensate of exciton-polaritons. Since then, Littlewood's group at the University of Cambridge has used their Dicke model to explore many topics in the dynamics of exciton-polaritons; a recent review of their work can be found in Keeling *et al.* [82], and a demonstration of their condensate modeling and comparison with experimental results can be found in Marchetti *et al.* [124]. Approaching the exciton-polariton system using the model of a weakly-interacting Bose gas has been another group of theorists in Europe. Their predictions of polariton lasing and polariton superfluidity were published by Malpuech *et al.* [119] and recently as a book [79]. The comparison of both models was done by Marchetti *et al.* [123]. The latter group, in addition to applying their models to the cryogenic II-VI (CdTe) and III-V (GaAs) systems examined experimentally, has also published several works with predictions of polariton lasing in room-temperature systems based on bulk GaN cavity exciton-polaritons, where the exciton binding energy is on the order of 40 meV, significantly above $k_B T$ at room temperature [75, 78, 118, 167]. Due to the similarities of bulk GaN and J-aggregate cavity exciton-polaritons at room temperature in terms of Rabi splitting and linewidths, we'll focus on the weakly-interacting Bose gas model since we can use the GaN predictions as a starting point for our threshold estimates and specifically point out what changes would need to be made in the model for J aggregates.[1]

[1]It should be noted that since the first demonstration of organic exciton-polariton devices by Lidzey *et al.* [104], several authors have attempted to model organic exciton-polariton systems, both based on J aggregates and based on organic crystals such as anthracene [2–4, 13, 34, 72, 108–110, 112–114, 129–133, 203]. The models in those studies are certainly significant to considerations regarding the actual relaxation dynamics of exciton-polaritons in organic systems, but aside from the efforts of Litinskaya and Reineker [111], none of the cited works considered the theoretical threshold for organic exciton-polariton lasers. One place where some of the cited works do overlap with literature from the inorganic exciton-polariton community is in considerations of the effects of photonic disorder

Summarizing the discussion in Kavokin *et al.* [79], an exciton-polariton laser can be considered an instance of a non-equilibrium Bose-Einstein condensate, or more specifically, a non-equilibrium superfluid. Since microcavity exciton-polaritons are 2D systems, a Bose-Einstein condensate is not possible since the sum of possible states into which a particle can be placed does not converge for a 2D system.

As formulated first by Bose and translated and added to by Einstein, Bose-Einstein condensation is the result of filling all possible thermodynamic states in a bosonic system; once these states are filled, the chemical potential of the system (initially negative) reaches 0, meaning that all additional particles added simply enter the ground state (this insight was Einstein's particular contribution to the theory). This phase transition from a collection of a thermal distribution of particles to a single coherent state is referred to as Bose-Einstein condensation. Mathematically, the number of bosons can be represented as the number of particles in the ground state plus the sum of particles in all of the other states, the distribution of which is given by the Bose-Einstein distribution function:

$$f_B(\mathbf{k}, T, \mu) = \frac{1}{e^{\left(\frac{E(\mathbf{k})-\mu}{k_B T}\right)} - 1} \tag{1.9}$$

We can write the density of particles as:

$$n(T, \mu) = \lim_{R\to\infty} \frac{N(T, \mu)}{R^d} = n_0 + \frac{1}{(2\pi)^d} \int_0^\infty f_B(\mathbf{k}, T, \mu) d\mathbf{k} \tag{1.10}$$

where R is the size of the system, d the dimensionality, and n_0 the density of particles in the ground state. When the integral in Eq. 1.10 reaches its maximum value, (i.e., $\mu = 0$), then all other particles are accounted for in the n_0 term, in which case the ground state is the Bose-Einstein condensate. This maximum value is referred to as the critical density. When the dimensionality is $d \leq 2$, the integral in Eq. 1.10 diverges, so no critical density can be reached, and therefore a strict Bose-Einstein

(which includes excitonic disorder in terms of variations in the index of refraction, or polarization density, of the medium). Specifically, when the critical concentration of exciton-polaritons required to reach superfluidity is limited not by thermal fluctuations but rather by disorder, then a *Bose glass* state consisting of localized condensed states can be formed [121, 122, 167].

condensate cannot exist in a low-dimensional system [79].

What can occur in 2D systems, specifically when the bosons are weakly interacting, is a transition to a superfluid state, in which two points within the superfluid are connected by a definite phase (i.e., they are coherent). This is not the same as a Bose-Einstein condensate, strictly speaking, since in a BEC not only are the properties of a superfluid present, but they exist over all space (i.e., there is a delta function in the momentum distribution at the ground state, so the spatial extent is infinite). In the case of the superfluid, the spatial extent can be limited. The possibility of a superfluid state in a 2D system was first suggested by Kosterlitz and Thouless [95]. The properties of a superfluid were explained by Landau in 1941 and then extended by Bogoliubov in 1947; the motivation for such work was an attempt to explain the properties of helium-4, in which the helium atoms are weakly-interacting bosons.

As given in Bogoliubov's treatment and explained in Kavokin *et al.* [79], the physics of a superfluid are characterized by the following parameters. First is the superfluid density given by:

$$n_s = \frac{2mk_BT_{KT}}{\pi\hbar^2} \tag{1.11}$$

where m is the mass of the particle (for polariton, $m \approx 10^{-5}m_e$) and T_{KT} is the temperature of the Kosterlitz-Thouless phase transition (i.e., transition to the superfluid state). The total density of particles includes both the superfluid density and the normal density:

$$n = n_n + n_s \tag{1.12}$$

and the normal density is given by the sum over the available states:

$$n_n = \frac{1}{(2\pi)^2}\int E(\mathbf{k},T,\mu)\left(-\frac{\partial f_B(E_{Bog}(\mathbf{k},T,0))}{\partial E_{Bog}(\mathbf{k})}\right)d\mathbf{k} \tag{1.13}$$

The sum in Eq. 1.13 is similar to that in Eq. 1.10, but instead of simply summing over the Bose-Einstein distribution, the distribution is modified to take into account the interparticle interactions. These interactions are represented by a modified par-

ticle energy dispersion, known as the *Bogoliubov dispersion*:

$$E_{Bog(\mathbf{k})} = \sqrt{E(\mathbf{k})[E(\mathbf{k}) + 2\mu]} \tag{1.14}$$

where the chemical potential representing adding additional particles to the ground state is given by:

$$\mu = NV_0 \tag{1.15}$$

For Wannier-Mott excitons treated by the authors of Kavokin *et al.* [78] (the type of excitons in the quantum well systems), V_0 is proportional to the Bohr radius of the exciton. Using the above framework of a weakly-interacting Bose gas, the authors derive the various phase diagrams given in Kavokin *et al.* [78] and specifically in GaN studies [118, 167]. The most recent study gives a critical concentration for the Kosterlitz-Thouless phase transition at 300 K of $n = 3 \times 10^{13}$ cm^{-2}, corresponding to one excitation per 1.8×1.8 nm^2 [168].

This number is actually a surprisingly high density when compared to the qualitative picture of exciton-polaritons. In that picture, one would expect that only one excitation per photonic state would be required one average to achieve stimulated relaxation. In the organic exciton-polariton literature, this was exactly the picture used by Litinskaya and Reineker [111] in attempting to calculate a threshold for J-aggregate exciton-polariton lasing. In that work, the authors used the photonic density of states as the "size" of the polariton, the result of which was a threshold density on the order of $1/\lambda^2$. The density calculated for the GaN system at room temperature, however, is around four orders of magnitude higher. The discrepancy is obviously due to the use of superfluidity models in the GaN literature, which actually take into account the effects of interparticle interactions on the correlation length of polaritons. The organic literature cited, on the other hand, is simply assuming a correlation length on the size of the photon mode.

If one were to model the J-aggregate system with the superfluidity models, two significant parameters would change compared to those in the GaN models. For

Frenkel excitons such as those in J aggregates, the exciton interparticle interaction energy V_0 may be dominated by other interactions since Frenkel excitons have a much higher binding energy and lower radius (i.e., they are isolated on single molecules). A different V_0 would affect the Bogoliubov dispersion and therefore the phase transition temperature and concentration. Also, the Rabi splitting in J-aggregate systems is usually on the order of about 100 meV or more, whereas in bulk GaN systems the Rabi splitting is at most 2/3 of that value and usually closer to 1/2 or less. This will likely have a significant effect on the derived phase diagram for J-aggregate exciton-polaritons since the trap caused by the Rabi splitting ($\approx \Omega_R/2$) in J-aggregate systems is considerably deeper than k_BT at room temperature, whereas the trap depth for the bulk GaN systems is on the same order as the trap depth. The different trap depth would manifest in the $E(\mathbf{k})$ dispersion of the lower branch, from which is derived the Bogoliubov dispersion.

Comparing the density predicted for GaN to that calculated via Eq. 1.7 for a traditional solid-state organic dye laser, we find that for the same quality factor cavity ($\tau_{cav} \approx 1$ ps), the traditional solid-state organic dye laser will likely have a lower threshold energy than that calculated for the bulk GaN exciton-polariton due to the relatively large stimulated emission cross-section that most organic laser dyes have ($\sigma \approx 10^{-16}$ cm^2). Furthermore, to actually calculate the *intensity* needed to reach exciton-polariton lasing, one must also include the lifetime of exciton-polaritons, since the lifetime will give the decay rate and therefore injection rate necessary to reach and maintain the critical concentration of phase transition. The equation used to model such dynamics is the Boltzmann transport equation:

$$\frac{dn_k}{dt} = P_k - \Gamma_k n_k - n_k \sum_{k'} W_{k\to k'} + \sum_{k'} W_{k'\to k} n_{k'} \tag{1.16}$$

where P_k is the pumping rate of the state k, the W's are the scattering rates into and out of the state k, and the n's are the populations of the states denoted. Adjusted for boson statistics, the *semiclassical Boltzmann equation* is:

$$\frac{dn_k}{dt} = P_k - \Gamma_k n_k - n_k \sum_{k'} W_{k\to k'}(1+n_{k'}) + (1+n_k)\sum_{k'} W_{k'\to k} n_{k'} \qquad (1.17)$$

The only difference between Eq. 1.16 and Eq. 1.17 is the additional n terms which account for stimulated scattering into and out of states. When the average population of a state k is $n_k \geq 1$, then stimulated scattering takes precedence over spontaneous scattering, allowing for massive population build-ups such as occurs in a traditional laser in a photon mode and in an exciton-polariton laser in an exciton-polariton state (in particular, the state at $k = 0$).

When considering a simplified picture of the traditional laser and exciton-polariton laser, the issue of excited state lifetime comes into play, since the lifetime of excitations gives the minimum intensity for pumping to maintain a coherent state. In the example dye laser shown in the previous section, the excited state lifetime of DCM molecules was on the order of nanoseconds. In a typical planar cavity of $Q \sim 1000$, though, the lifetime of the cavity photon is only about a picosecond. *This means that if the density of excitations in the traditional and polariton lasers needed to achieve coherence were equal, the traditional laser's threshold would be* ***three orders of magnitude less*** *than that of the exciton-polariton laser.* Therefore, if the exciton-polariton threshold calculations for bulk GaN are on the same order of magnitude as those for J-aggregate exciton-polaritons, then the threshold at room temperature for a J-aggregate exciton-polariton laser may be no better, if not worse, than that of a state-of-the-art organic VCSEL. Clearly, the density of excitation required for a superfluid phase transition in a J-aggregate exciton-polariton system is an important parameter that requires further study, especially considering the alternative solid-state dye laser thresholds already achievable in organic systems.

So why continue to study exciton-polaritons in organic systems if their technological benefit is uncertain at best? For starters, the use of strong coupling of Wannier-Mott excitons to Frenkel excitons through exciton-polaritons to bypass the electrical injection problems of solid-state organic dye lasers (e.g., see Kozlov *et al.*

[96] and Baldo *et al.* [14] and citing articles for more discussion on issues preventing electrically-pumped organic laser diodes) is one motivation among others for such a structure that has been discussed in literature [1, 66, 106, 198]. Secondly, the use of microcavity exciton-polaritons as parametric amplifiers continues to be an area of interest, and only one attempt has thus far been made at achieving parametric amplification in organic exciton-polariton systems [160].[2] Additionally, the physics of macroscopic coherent states and superfluids is an ongoing area of interest, and as the temperature is lowered, the correlation length for J-aggregate exciton-polaritons (i.e., "cross-section") would almost certainly increase, leading to lower lasing thresholds and other superfluid phenomena. And lastly, as noted above, the considerably larger Rabi splitting of the J-aggregate exciton-polariton system may in fact lead to a much larger coherence domain than calculated for bulk GaN at room temperature, and until the issue is tackled by the theoretical community, the room temperature threshold of J-aggregate exciton-polariton lasing remains an open question. And even if exciton-polariton lasers in J-aggregate organic systems remain elusive due to the underlying physics of the J-aggregate system, this will mean instead that J-aggregate exciton-polaritons will have considerable potential as nonlinear optical switches, since if at moderate excitations the system is sufficiently perturbed to prevent superfluid formation, then a low-power all-optical switch would be the next obvious application.

In the next section, we will explore one of the materials platforms most often used in realizing strongly-coupled light-matter systems at room temperature, that of J aggregates. The physics of J aggregation, which is itself based on near-field strong coupling amongst individual molecules, will be discussed.

[2]In this attempt, the excitonic part of the polariton was the charge-transfer (CT) exciton in a zinc-porphyrin dye, used in order to bypass the photobleaching issues of many cyanine dyes [41, 68, 81, 163, 165, 177, 197]. The CT exciton, however, is *not* the lowest excitonic state in the system; at RT, one would expect fast decay of polaritons due to sub-picosecond relaxation of the excitons toward lower-energy states.

1.3 J Aggregates

J aggregates, short for Jelley aggregates, have found extensive use in industry because of their optical and electronic properties. In the photographic film industry of the 20^{th} century, J aggregates were widely use as sensitizers for silver halides [53, 170, 178]. J aggregates were first reported by Edwin Jelley of Kodak in a letter to the journal *Nature* in 1936 [73]. The materials were further researched by G. Scheibe, and because of his work J aggregates are also at times referred to as Scheibe aggregates [161]. The term "J aggregate" generally refers to any aggregation of molecules in which the transition dipoles of the molecules align in such a way that the transition dipole of the entire aggregate is larger than that of a single molecule (i.e., the aggregates' transition dipole moment is the sum of the dipole moments of the individual molecules comprising the aggregate). Along with this dipole moment summation comes the formation of a band of excited states in the aggregate, resulting in a red-shift and narrowing of the oscillator strength and therefore absorption spectrum of the aggregate compared to that of the molecule [191].

1.3.1 J-Aggregate Physical Model

The physical model explaining the optical properties of J aggregates can be built up from an understanding of the interaction of just two dye molecules. When two cyanine dye molecules are in close proximity their transition dipoles will couple, producing new energy levels of the system and causing a mixing of the excited states of the uncoupled molecules. The interaction energy for two dipoles is orientation dependent. The reason for this orientation dependence is depicted qualitatively in Figure 1-6. If the two molecules are aligned tip to tail, then the energy is higher when the transition dipoles are out of phase; in this state, the oscillator strength is 0 since the dipole moments cancel. On the other hand, if the transition dipoles are in phase, the energy is lowered and the net transition dipole moment is enhanced by a factor of $\sqrt{2}$ [187].

A similar picture emerges for a J aggregate where there are N molecules in a row, with transition dipoles strongly coupled to one another. The lowest energy

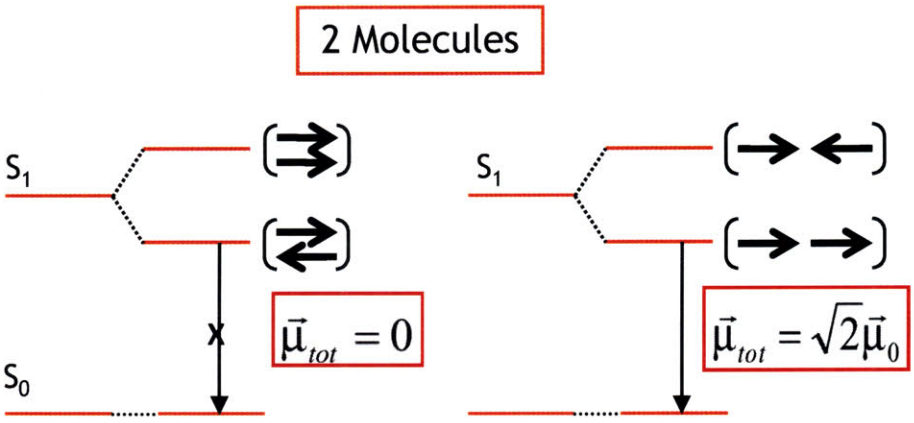

Figure 1-6: Schematic of effect of dipole alignment on energy levels [187].

excited state corresponds to all molecules coupling in phase, with the excitation delocalized over all N molecules, and this state also possesses an enhanced transition dipole moment [191]. The redistribution of oscillator strength towards lower energy explains why the J-aggregate absorption peak is significantly red-shifted relative to the monomer, typically 50 to 60 nm, and also why the absorption spectrum is asymmetric and spreads out towards higher energy. van Burgel *et al.* [191], using a 1D coupled exciton model (the Frenkel-exciton model), shows the derivation of a band of states for the one-exciton band of N coupled molecules. The coupled molecules are modeled using the Frenkel exciton Hamiltonian:

$$\hat{\mathcal{H}} = \hbar \sum_{n=1}^{N} \omega_n (\hat{b}_n^\dagger \hat{b}_n) + \hbar \sum_{\substack{n,m=1 \\ n \neq m}}^{N} V_{nm} (\hat{b}_n^\dagger \hat{b}_m + \hat{b}_m^\dagger \hat{b}_n) \tag{1.18}$$

where ω_n is the transition frequency of the n^{th} molecular dipole (usually the lowest singlet exciton state), $\hat{b}$ and $\hat{b}^\dagger$ are the Pauli annihilation and creation operators, respectively, and V_{nm} is the coupling between the n^{th} and m^{th} molecules. For J-aggregates, only nearest-neighbor coupling is used, meaning $V_{n,n\pm1} = V$ and the other V's are 0. Diagonalizing the Hamiltonian with only the nearest-neighbor coupling gives the eigenfrequencies of the one-exciton band, which are [191]:

$$\Omega_k = \omega + 2V\cos\left(\frac{\pi k}{N+1}\right) \tag{1.19}$$

where $k = 1 \ldots N$ is the quantum number of each coupled state (not to be confused with momentum, though a correlation could likely be made since an effective mass could likely be assigned to each state) and Ω_k its corresponding frequency, ω is the single molecule transition frequency, and V is the nearest-neighbor coupling.

The oscillator strength of each transition dipole from the ground state to k^{th} state is given by [191]:

$$\mu_{k,g} = \mu_{mon}\sqrt{\frac{2}{N+1}}\frac{1-(-1)^k}{2}\cot\left[\frac{\pi k}{2(N+1)}\right] \tag{1.20}$$

For large N, Eq. 1.20 simplifies to the following for the $k = 1$ state, which will be referred to from here on as the "J-aggregate state" [191]:

$$\mu^2_{J-Agg} \approx 0.81(N+1)\mu^2_{mon} \tag{1.21}$$

Figure 1-7 plots the distribution of oscillator strength and the eigenstates for a J aggregate with $N = 16$, $E_{mon} = 2.39$ eV, and $\hbar V = -0.15$ eV.

Eq. 1.21 indicates that given a large number of molecules coherently coupled in the J aggregate, most of the oscillator strength will be concentrated in the lowest energy eigenstate, accounting for both the red-shift and narrowing of the J-aggregate resonance compared to that of a single molecule. An additional consequence of Eq. 1.21 is that since the the spontaneous emission rate scales as μ^2, the radiative rate of the J-aggregate state is roughly N times faster than that of the monomer. Finally, because of the large red-shift of the J-aggregate state from the monomer resonance, the J-aggregate state overlaps with the lower tail of the density of states of the monomer, meaning that the Stokes shift in fluorescence is small or non-existent as there are few if any localized trap states into which the J-aggregate state could relax [19].

For all of the reasons cited above, Lidzey *et al.* [105] was able to demonstrate strong coupling of J-aggregate excitons to a microcavity. This demonstration followed on

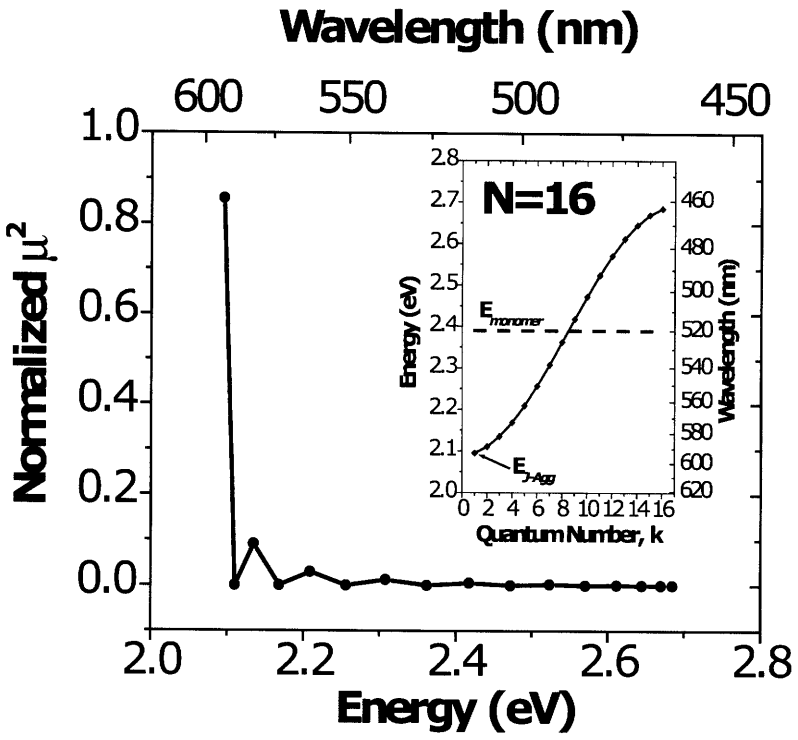

Figure 1-7: Distribution of oscillator strength and eigenenergies for a J aggregate with $N = 16$, $E_{mon} = 2.39$ eV, and coupling constant $\hbar V = -0.15$ eV.

a demonstration a year earlier which utilized excitons in porphyrin molecules [104]. Although there are several examples in literature of strong coupling to an organic resonance in absorption, in general, most organic molecules have too large of a Stokes shift for the strong coupling to also be seen in luminescence (i.e., excitations relax from the strongly coupled polariton state into uncoupled, Stokes-shifted localized excitonic states) [64, 65, 84].

The Rabi splitting due to J-aggregate excitons is typically 1 to 2 orders of magnitude higher than those using excitons of most other material systems. For example, when J aggregates were incorporated in a metal mirror microcavity, polariton emission peaks were separated in energy by more than 300 meV, which corresponds to record high coupling strengths an order of magnitude larger than any Rabi splitting achieved with inorganic semiconductors [63]. Also, the first reported observation of room temperature polariton photoluminescence utilized J aggregates as the exciton material in the microcavity. This observation was possible because the Rabi splitting is much larger than room temperature thermal noise ($\sim$ 26 meV), and because J-aggregate excitons remain bound at 300 K, unlike most inorganic excitons (e.g., in GaAs or CdTe), which ionize into free electrons and holes well below this temperature (as a comparison, the Rabi splitting achieved in a CdTe-quantum-well system was 20 meV at 100 K) [105, 153].

1.3.2 J-Aggregate Thin Films

J-aggregate thin films are commonly formed using one of three techniques: Langmuir-Blodgett, spin-casting in a polymer matrix, and layer-by-layer (LBL) deposition [60, 134, 138]. The last technique is the newest, having first been reported by Fukumoto and Yonezawa in 1998.

The LBL deposition method has been an active field of materials science research in the past decade since it was first reported by Decher *et al.*[5, 44–48, 60, 80, 136, 146] A basic LBL process consists of dipping a substrate in alternating polycation and polyanion solutions. Substrates undergo these sequential immersions in cationic and anionic solutions (SICAS) in order to build up a thin film, one layer of polymer at a

time. The polycations and polyanions can be either strong or weak. This classification refers to the pH-sensitivity of the polyelectrolytes. Strong polyelectrolytes are not pH sensitive, whereas the charge on weak polyelectrolytes depends on the pH of the solvent. Between dips in the polycation and polyanion solutions, the substrates are rinsed, typically in the same solvent used for the polycation and polyanion, in order to remove excess polymer that has not been ionically bonded to the substrate. The substrate must be prepared in some manner that allows the first adsorption step to occur. For glass substrates, an oxygen plasma treatment generally leaves enough negative charge on the surface (assuming the polycation solvent is a weak acid or base) such that enough polycation can adsorb for the build-up process to start.

While the LBL process was developed with polycations and polyanions as the thin film constituents, further work in the 1990s showed that one of the polyelectrolytes could be replaced by a dye molecule or other small, charged component [5]. The only requirement of the charged component was that enough of the component adsorb in the LBL process to reverse the charge on the surface of the substrate. This requirement is easily satisfied if the charged component is multivalent or if the charged component will form aggregates. Fukumoto and Yonezawa showed that, by using J-aggregating cyanine dyes as one of the charged components, thin films of J aggregates could be built using the LBL process.

In Chapter 2, the optical and morphological properties of LBL thin films of J aggregates will be examined during the LBL growth cycles. Understanding these properties will assist in the engineering of microcavity exciton-polariton devices in which an LBL J-aggregate thin film is strongly coupled to an optical microcavity.

Chapter 2

Optical Properties of J-Aggregate Thin Films

As a first step in engineering cavity exciton-polariton devices utilizing thin films of J aggregates of cyanine dyes, the optical and morphological properties of the active layer need to be thoroughly investigated. Compared to exciton-polariton devices utilizing quantum wells of inorganic semiconductors, the active layer in organic exciton-polariton devices is significantly more disordered, being comprised of a thin film of randomly-oriented molecules. Additionally, since organic exciton-polariton devices are generally operated at room temperature, the homogeneous broadening of the exciton transition will be significantly greater than in the case of inorganic semiconductor quantum-well devices operated at cryogenic temperatures. For these reasons, thin films of J aggregates are grown and their linear optical and morphological properties characterized during the growth process. Additionally, these thin films are then investigated through incoherent pump-probe spectroscopy to determine the transient behavior of excitons in J-aggregate thin films as well as the coherence length of the J aggregates at room temperature down to cryogenic temperatures.[1]

[1]The film deposition and analysis efforts detailed in the linear optical and morphological characterization were carried out at MIT by myself and co-authors in the study Bradley *et al.* [23]. The films examined in the pump-probe experiments were fabricated at MIT, and the pump-probe spectroscopy was done by our collaborators at Brown University in Professor Arto Nurmikko's group, Qiang Zhang and Tolga Atay; the analysis of the pump-probe results presented was contributed to by both groups at MIT and Brown. The figures in the nonlinear optical properties section are based

2.1 J-Aggregate Thin Film Linear Optical Response

In this section, the characterization of the linear optical properties of layer-by-layer (LBL) J-aggregate thin films is described. J-aggregate LBL thin films are found to have a peak thin film absorption constant of $\alpha = (1.05 \pm 0.1) \times 10^6$ cm^{-1}, one of the highest reported for a neat thin film. As noted in Chapter 1, such highly absorptive materials embedded in a matched optical microcavity recently enabled demonstrations of the strong coupling limit in the form of microcavity exciton-polaritons and the demonstration of room-temperature operation of exciton-polariton optoelectronic devices [73, 104, 105, 162, 189, 195, 196], which were not achieved in inorganic exciton-polariton systems until 2008 [10, 85, 156, 190]. The use of LBL to create thin films of J-aggregated dyes has been established for almost a decade [5, 49, 60, 80, 136, 146, 151, 152]. Previous analyses of LBL J-aggregate films, however, did not report the thin film optical constants, the real and imaginary components of the index of refraction ($\tilde{n} = n + i\kappa$), in the context of a materials investigation [22]. Here, by combining data from morphological and optical measurements, the optical constants of LBL TDBC J-aggregate films are determined. As will be shown in later chapters, these optical constants are key parameters in engineering the linear optical properties of devices for room-temperature strong-coupling applications.

2.1.1 Materials and Experimental Procedure

LBL thin films of TDBC (5,6-dichloro-2-[3-[5,6-dichloro-1-ethyl-3-(3-sulfopropyl)-2(3H)-benzimidazolidene]-1-propenyl]-1-ethyl-3-(3-sulfopropyl) benzimidazolium hydroxide, inner salt, sodium salt) J-aggregates deposited on glass are used to probe optical and morphological properties. Figure 2-1 shows a schematic of the sample structure and the molecular diagrams of the thin film constituents.

The samples are prepared in an LBL process in which samples undergo sequential immersion into cationic and anionic solutions (SICAS). In our process, samples are immersed in polycationic PDAC (poly(diallyldimethylammonium chloride)) and

on figures by Tolga Atay and Qiang Zhang, which were presented in [7] and [8].

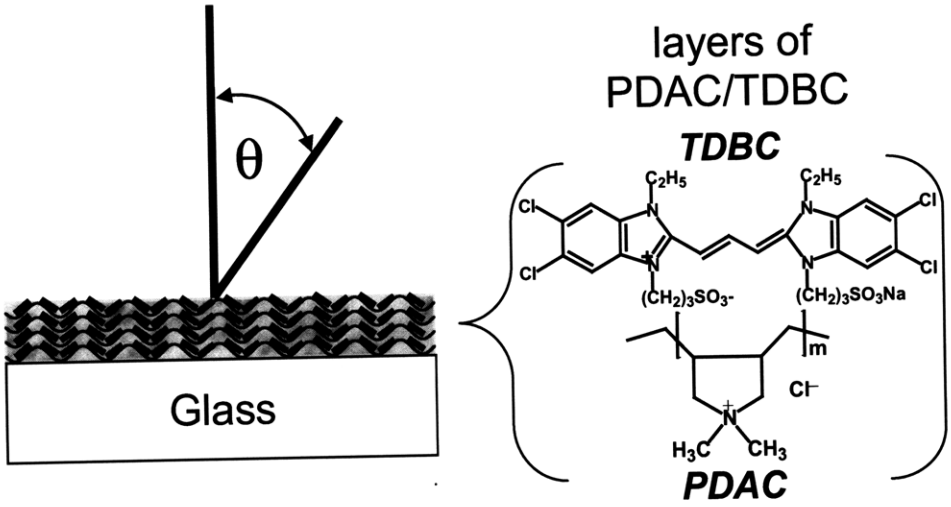

Figure 2-1: Layer constituents and sample structure. The polycation used in the LBL growth is PDAC, and the anion is TDBC, a J-aggregate-forming cyanine dye. Optical measurements are taken with the LBL-film side of the sample facing the light beam at a specified angle θ away from the normal.

anionic TDBC, a J-aggregate-forming cyanine dye. Layers of polyelectrolyte and J-aggregate-forming dye were alternately adsorbed onto glass slides. Figure 2-2 shows a schematic of the adsorption of film constituents as the substrate undergoes each SICAS.

The dye used was obtained from Nippon Kankoh Shikiso Kenkyusho Co., Ltd. (CAS 28272-54-0). While this dye will be referred to as "TDBC" throughout this thesis, in literature it is also often referred to as "BIC." TDBC is often used interchangeably, though more accurately TDBC actually refers to the form of the same molecule with sulfobutyl, not sulfopropyl, side groups–this distinction, though, has often been confused in literature. The polyelectrolyte used was PDAC, 20% by weight in water, $M_w = 4 - 5 \times 10^5$, obtained from Sigma-Aldrich (CAS 26062-79-3). The dye solvent and rinses for the dye adsorption step were approximately pH 9 solutions of deionized (DI) water plus sodium hydroxide. The effect of pH on TDBC has been documented [174]. The sodium hydroxide was obtained from EM Science. The polyelectrolyte solvent and rinses for the polyelectrolyte adsorption step were DI

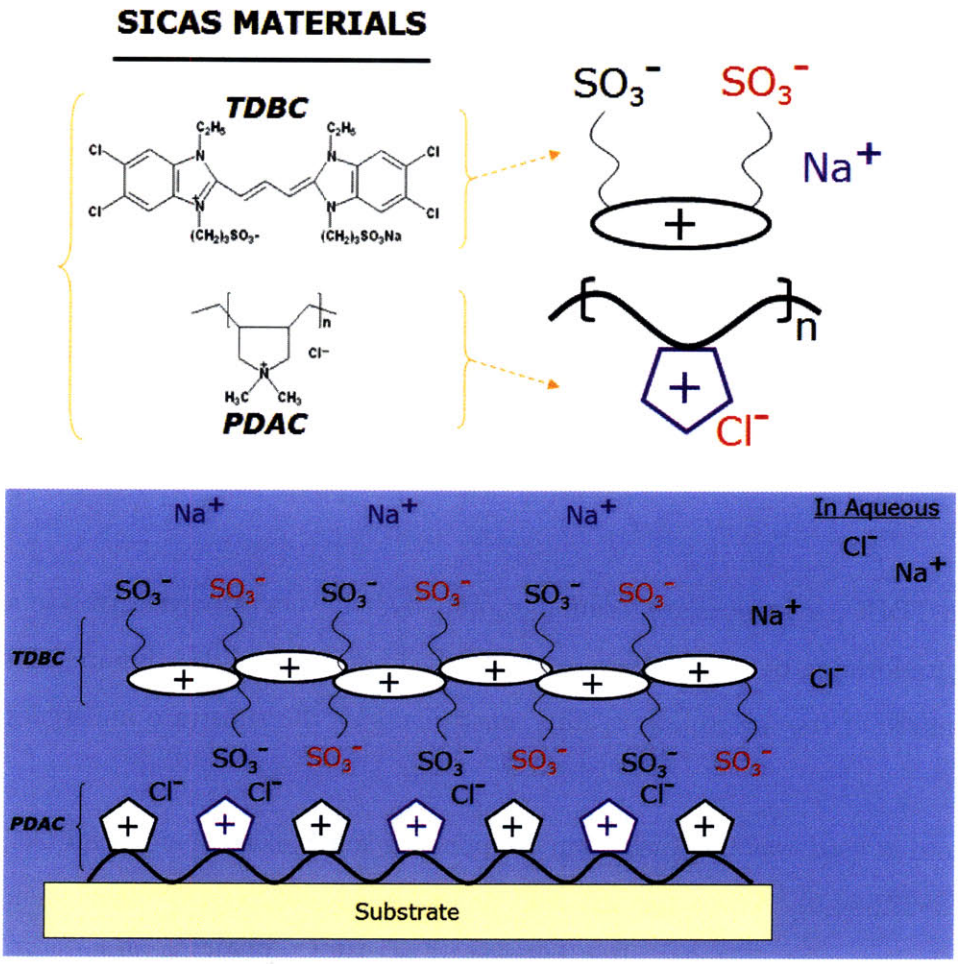

Figure 2-2: Schematic of counterion adsorption in each of the substrate's sequential immersions in cationic and anionic solutions (SICAS) in the layer-by-layer (LBL) process. In the case of PDAC/TDBC J-aggregate thin films, the TDBC dye is the anion and PDAC the polycation.

water.

A standardized routine was used to prepare the dye and polyelectrolyte solutions. The dye solution was approximately 5×10^{-5} M. Once the dye was added to the dye solvent, the dye bucket was placed in an ultrasonic cleaner to sonicate for 30 minutes. The dye was then mixed with a one-inch magnetic spin bar for 10 minutes, sonicated for 20 minutes, mixed for 5 minutes, and finally sonicated for 5 minutes. The polyelectrolyte solution was approximately 3×10^{-2} M, prepared by adding 10 mL of polyelectrolyte to 390 mL of DI water. The polyelectrolyte solution was prepared using the same time intervals for mixing/sonication as the dye solution preparation, except sonication and mixing at each step were swapped. Care was taken throughout the deposition to shield the dye solution and samples from light.

Prior to the deposition, the glass slides were cleaned with a detergent solution (Micro-90), acetone, and isopropanol. The acetone, isopropanol, and methanol used in this study were OmniSolv-brand solvents made by EMD Chemicals. The slides were then treated with oxygen plasma for six minutes in a Plasma Preen system. The layer-by-layer deposition was performed using an automated Leica Autostainer XL. The polyelectrolyte adsorption step consisted of dipping the slides in polyelectrolyte solution for 15 minutes and in the three rinses for two minutes, two minutes, and one minute, respectively. The dye adsorption step used the same time intervals as those used in the polyelectrolyte adsorption step. In later experiments using PDAC/TDBC LBL thin films performed after the experiments in this section were published in Bradley *et al.* [23], the dye and polyelectrolyte dipping times were reduced to 5 minutes to reduce total deposition time with no noticeable change in J-aggregate properties or film thickness.

Upon removal from the stainer, each sample was blown dry using nitrogen gas. For each sample, the sample face that was not treated with oxygen plasma prior to deposition was cleaned using methanol to remove deposited layers. Measurements for this study were performed in the MIT Center for Materials Science and Engineering Shared Analytical Lab. The atomic force microscopy (AFM) data were collected on a Digital Instruments D3000 Scanning Probe Microscope in tapping mode using

phosphorus-doped silicon tips from Veeco. The optical data were collected using a Cary 5E UV-Vis-NIR spectrophotometer. The transmission data were collected with the light beam at normal incidence, $\theta = 0°$. The reflectance data were collected in a V-W setup with the light beam incidence at $\theta = 7°$ using the Cary Specular Reflectance Accessory in Absolute Reflectivity mode.

2.2 Morphological Properties

Samples with different numbers of PDAC/TDBC layers were produced in order to observe the thin film structure at various stages of growth using AFM. Figure 2-3 shows AFM images throughout the various stages of growth with histograms showing formation of PDAC/TDBC layers and a plot of RMS roughness versus the number of SICAS.

As shown in the AFM images for 1.5 SICAS and 2.0 SICAS compared to blank glass, the layered structure of the PDAC/TDBC J-aggregate films does not appear until the second dye immersion. This delay is likely caused by the lack of a precursor layer or surface treatment on the glass support. The images show that layered growth is still dominant at 4.5 SICAS, but at 6.5 SICAS and 10.5 SICAS the growth has shifted to a Stransky-Krastanov (SK) type of process, forming large islands of material. To quantify the growth trend, RMS roughness is measured from 16 μm^2 AFM images of films that underwent 3.5 SICAS to 10.5 SICAS. The plot in Figure 2-3 shows that a mostly constant RMS roughness in the range of 1.4 to 2.0 nm persists through the first 5.5 SICAS, indicating layered growth, but beyond 6.5 SICAS, the roughness increases, indicating the shift to SK-type growth.

2.2.1 Linear Optical Measurements and Modeling

The thickness data obtained from the AFM measurements are combined with optical transmittance and reflectance data to extract the optical constants of the LBL PDAC/TDBC J-aggregate films. Figure 2-4 shows a photograph of substrates that underwent different numbers of SICAS of PDAC/TDBC. The purple color in trans-

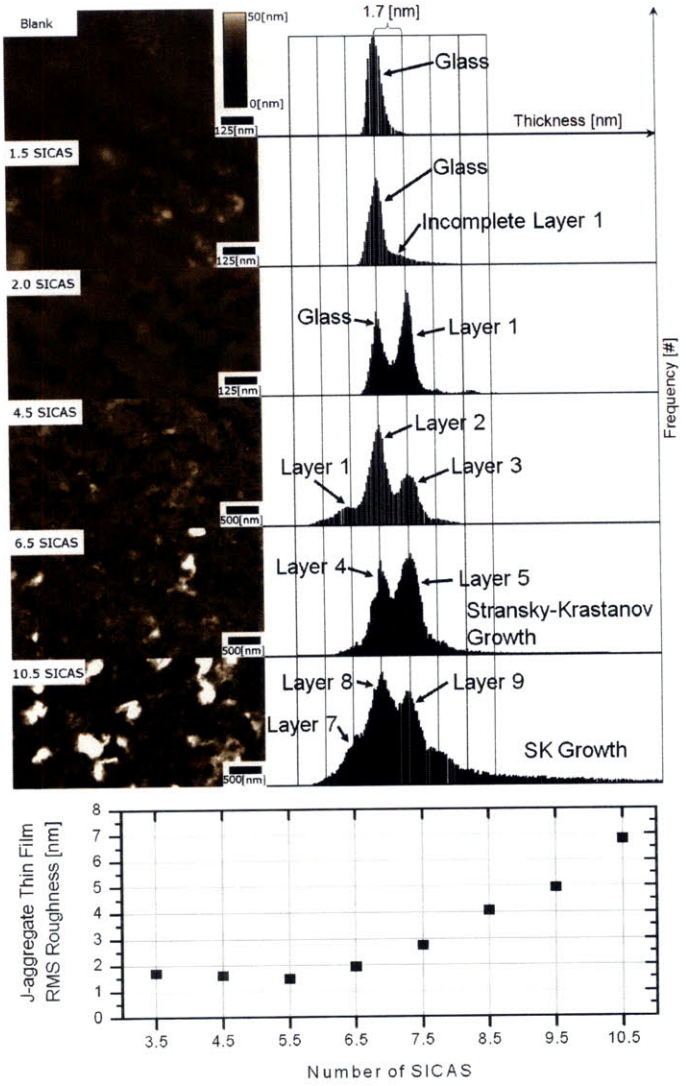

Figure 2-3: Atomic force microscope (AFM) images of LBL J-aggregate growth with histograms of thickness frequency. Each sequential immersion in cationic and anionic solution (SICAS) consists of a PDAC adsorption step followed by a TDBC adsorption step, with $N.5$ SICAS referring to N SICAS followed by an additional PDAC adsorption step. The AFM images show samples that underwent the indicated number of SICAS. The top three images show that significant PDAC/TDBC layered growth is not evident until 2.0 SICAS. The bottom three images show the build-up of thick layers. The histograms are lined up at the dominant film thicknesses to show that each layer is about 1.7 nm thick, the estimate used when modeling the optical constants of the films. The histograms are created from the full 1 μm^2 and 16 μm^2 images for the first three and last three films shown, respectively. The layer numbers indicated in the histograms are based on the progression of layer growth observed in AFM images. The plot shows the roughness profile of films from 3.5 to 10.5 SICAS. The roughness is nearly constant until 6.5 SICAS, when the dominant growth regime changes from layered to Stransky-Krastanov (SK) type. All images have a vertical scale of 50 nm.

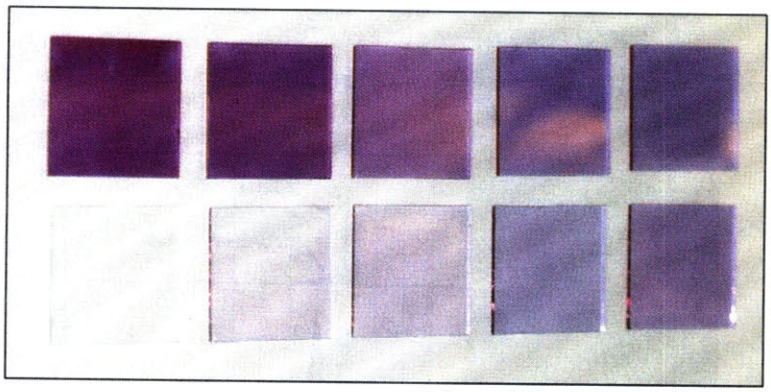

Figure 2-4: Photograph of a series of LBL PDAC/TDBC J-aggregate thin films of increasing numbers of SICAS, which results in increasing thickness of J-aggregate thin film deposited.

mission results from the absorption/reflection of the J-aggregate thin film of light in the green/orange region of the spectrum (540-600 nm). Figure 2-5 plots measured optical data.

Light propagation through the sample is modeled using propagation and interface matching matrices (also known as *transfer matrices* or *linear dispersion theory (LDT)*), with film thicknesses as inputs to the model and refractive indices as fitting parameters. For numerical calculations, we modeled the films using propagation and matching matrices:[194]

$$\begin{bmatrix} E_{1a}^{+} \\ E_{1a}^{-} \end{bmatrix} = \begin{bmatrix} e^{-i\beta} & 0 \\ 0 & e^{i\beta} \end{bmatrix} \begin{bmatrix} E_{1b}^{+} \\ E_{1b}^{-} \end{bmatrix} \tag{2.1}$$

$$\begin{bmatrix} E_{1b}^{+} \\ E_{1b}^{-} \end{bmatrix} = \frac{1}{t} \begin{bmatrix} 1 & r \\ r & 1 \end{bmatrix} \begin{bmatrix} E_{2b}^{+} \\ E_{2b}^{-} \end{bmatrix} \tag{2.2}$$

Eq. 2.1 shows a propagation matrix equation, which relates the forward and reverse traveling electric field amplitudes at boundary (a) to the amplitudes at boundary (b). The medium (1) is modeled by the parameter $\beta = \frac{2\pi\tilde{n}d}{\lambda}$, where $\tilde{n}$ is the complex index of refraction of the medium, $\tilde{n} = n + i\kappa$, and d is the thickness of the layer. Eq. 2.2 shows a matching matrix equation, which matches the forward and reverse traveling electric field amplitudes at boundary (b). r and t are respectively the reflection

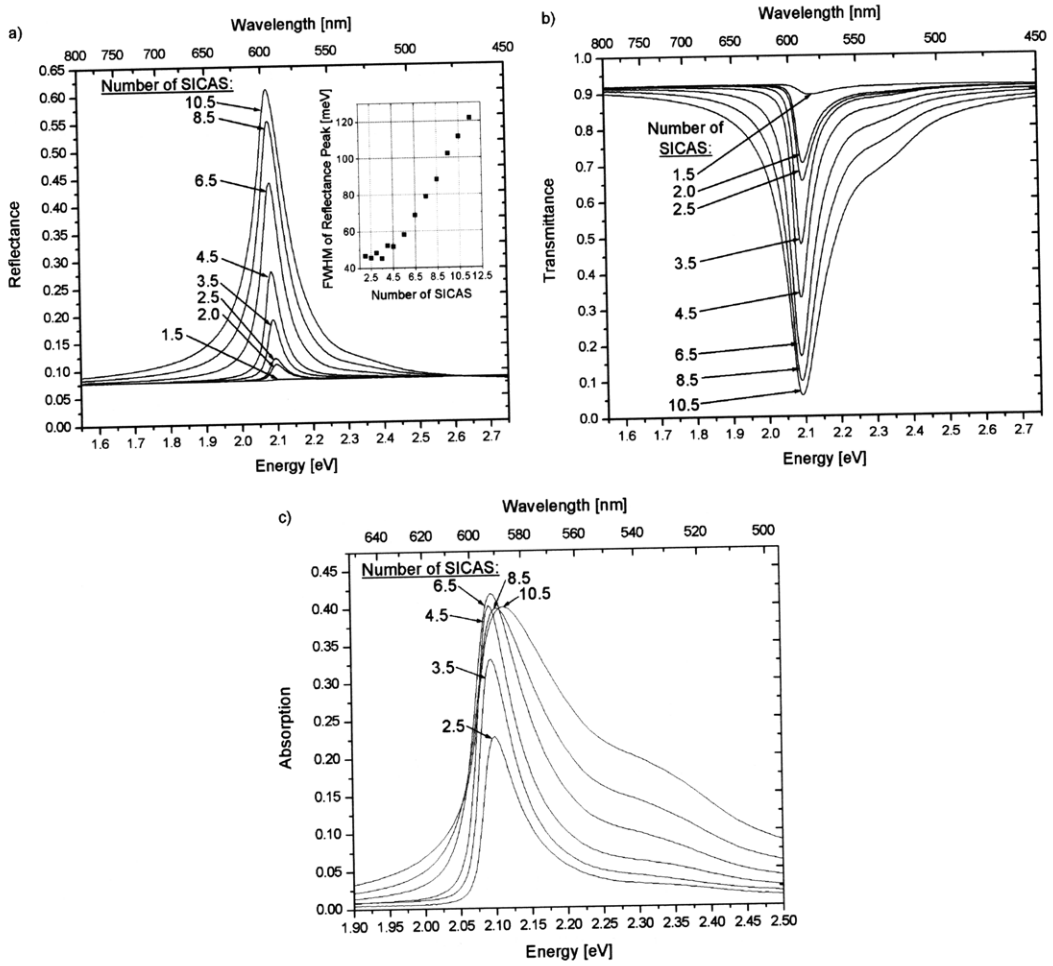

Figure 2-5: Optical data and characterization of optical properties for LBL PDAC/TDBC J-aggregate films. Plots (a) and (b) show reflectance, R, at $\theta = 7°$ and transmittance, T, at $\theta = 0°$ for a series of samples that underwent different numbers of SICAS. Plot (a, inset) shows the FWHM of the reflectance peak as a function of number of SICAS. Plot (c) shows absorption for the same samples given by $1-R-T$.

and transmission Fresnel coefficients for a wave incident from medium (1) to medium (2). The parameters β, r, and t must be modified slightly to model non-normal incidence [194]. Our model calculated transmittance at $\theta = 0°$ and reflectance at $\theta = 7°$ based on the light traveling through air ($\tilde{n} = 1$), an LBL PDAC/TDBC J-aggregate film, the glass slide ($\tilde{n} = 1.5$), and then air ($\tilde{n} = 1$). From the AFM data, the thickness of deposited physical layers was observed to vary from about 1.4 nm to 2.0 nm per adsorbed layer. Because the glass substrate thickness, d_s, is very large in the wavelength range of interest ($\frac{d_s}{\lambda} \gg 1$), we modeled the glass as 1 mm thick and averaged the calculated transmittance and reflectance for 100 glass thickness variations comprising a phase change of 0 to 2π at the wavelength of interest in order to remove interference effects in the substrate. For near-normal incidence calculations, the light from the spectrometer was assumed to be half TE-polarized and half TM-polarized.

2.2.2 Determining the Thin Film Index of Refraction

Two methods are employed in calculating the (n,κ) values. In the first method, the (n,κ) values are obtained by minimizing the sum of least-squared errors of the calculated transmittance and reflectance for the first four sample thicknesses. This approach is similar to that described by Djurišić *et al.*, however in our method we perform a single (n,κ) fit and do not incorporate the use of a penalty function in calculating the least-squared errors [51]. In the first method, we assume that the absorption constant in the layered growth regime does not change as more PDAC/TDBC layers are deposited. The ranges in n and κ values are $[0.05, 5]$ and $[0, 6]$, respectively, with a resolution of 0.05 in both. It should be noted that since no PDAC/TDBC layer is evident for the first 1.5 SICAS, the transmittance and reflectance data for the first layer correspond to what we refer to as the 2.5 SICAS sample. Numerical fits to the thickness dependent reflectance and transmittance data at wavelength $\lambda = 596$ nm based on the first method are shown in Figure 2-6(a) for complex index of refraction with a real part, n, between 1.55 and 1.85 and an imaginary part, κ, between 4.65 and 5.60. The high extinction coefficient, κ, corresponds to an absorption constant of the film of $\alpha = \frac{4\pi\kappa}{\lambda} = (1.05 \pm 0.1) \times 10^6$ cm^{-1} at $\lambda = 596$ nm. In our analysis we

assume complete layer coverage in contrast to the partial coverage observed in Figure 2-3. This assumption underestimates the κ values for the thin film.

The second method employed in calculating the (n,κ) values is based on the Kramers-Krönig (KK) transformations, which relate the real and imaginary parts of the index of refraction. The Kramers-Krönig (KK) regressions for finding (n,κ) were based on the method outlined by Nitsche and Fritz [137]. The propagation and matching matrix model described above was used to calculate the reflectances and transmittances used in the KK regression. However, to minimize convergence errors introduced by interference in the substrate, 100 glass variations are used, comprising a phase change of 0 to 2π at the wavelength of interest. The following approximation of the KK transformation given by Nitsche and Fritz relating n and κ is utilized:

$$n(\omega_j) \cong n_{offset} + \frac{2}{\pi} P \int_{\omega_L}^{\omega_U} \frac{\omega \kappa(\omega)}{\omega^2 - \omega_j^2} d\omega, \quad \omega_L \leq \omega_j \leq \omega_U \tag{2.3}$$

The background contributions of frequencies outside of the measured spectrum are approximated through the use of the n_{offset} term in Eq. 2.3. For the regressions, $n_{offset} = 1.7$ is used based on the assumption that PDAC and TDBC resemble many other organic materials outside of the visible spectrum. Like in the algorithm by Nitsche and Fritz, a Levenberg-Marquardt algorithm is used for optimizing κ [125]. The maximum step size at each iteration was 0.01, which ultimately dictated the resolution of the resulting κ spectra. The Cauchy principal value in Eq. 2.3 was approximated using Maclaurins Formula [139].

The "quasi" aspect of the quasi-Kramers-Krönig regression method comes from only allowing the imaginary part of the extinction coefficient, κ, to change by at most a small amount in each iteration (this is the maximum step size referred to above). Since κ only changes by a small amount at any given time, the Kramers-Krönig relations are still satisfied within a certain tolerance, which is the reason for the name quasi-Kramers-Krönig. If κ were allowed to vary by large amounts, the regression would become unstable due to the violation of the Kramers-Krönig relations which enforce the physical condition of causality in the derived index of refraction.

Figure 2-6 shows the results of the two methods.

2.2.3 Discussion of Linear Optical Properties

For samples that underwent 2.5 SICAS (estimated as 1 complete layer) to 5.5 SICAS (estimated as 4 complete layers), the (n,κ) spectra for each sample are calculated from the sample's reflectance spectrum. Plots 2-6(b) through 2-6(d) show the results of the KK regressions. Plot 2-6(b) shows the measured transmittance and reflectance for the 3 layer (5.1 nm thick) film along with the reflectance and transmittance calculated from the (n,κ) spectra in Plot 2-6(c). The transmittance calculated from the KK regression is in good agreement with the measured transmittance. Plot 2-6(d) shows the peak in κ for 1 layer (1.7 nm thick) to 4 layer (6.8 nm thick) films calculated using the KK regressions as well as the movement of the peak in κ to lower energies as the number of layers increases. The results of the KK regression confirm the high magnitude of the absorption constant of the film found through the first method.

Several trends are noticeable in the optical data as samples undergo more SICAS. The reflectance data in Figure 2-5(a) show that the peak in reflectance moves to lower energy and the full-width at half maximum (FWHM) increases. In addition, Figure 2-5(c) shows the onset of a high energy peak in absorption. Lastly, the KK regression results plotted in Figure 2-6(d) show the peak κ value increasing with the number of SICAS. We have considered two approaches in explaining these trends.

The first explanation is based on the changing morphology of the thin films. Our assumption of complete layer coverage in numerical analysis could be responsible for the apparent increase in κ plotted in Figure 2-6(d). In addition, the increase in reflectance FWHM may be due to a weak microcavity caused by SK growth or increasing inhomogeneous broadening. Lastly, the onset of the high energy peak could be attributed to vibronic states in the J aggregate, as noted in previous studies of J-aggregate monolayer films deposited using a Langmuir-Blodgett technique [97, 140].

An alternative explanation is based on strong coupling of the J-aggregate excitons to the electromagnetic field in the form of exciton-polaritons [42, 67, 147, 147, 171]. The effects of strong coupling will be more pronounced as the number of excitons

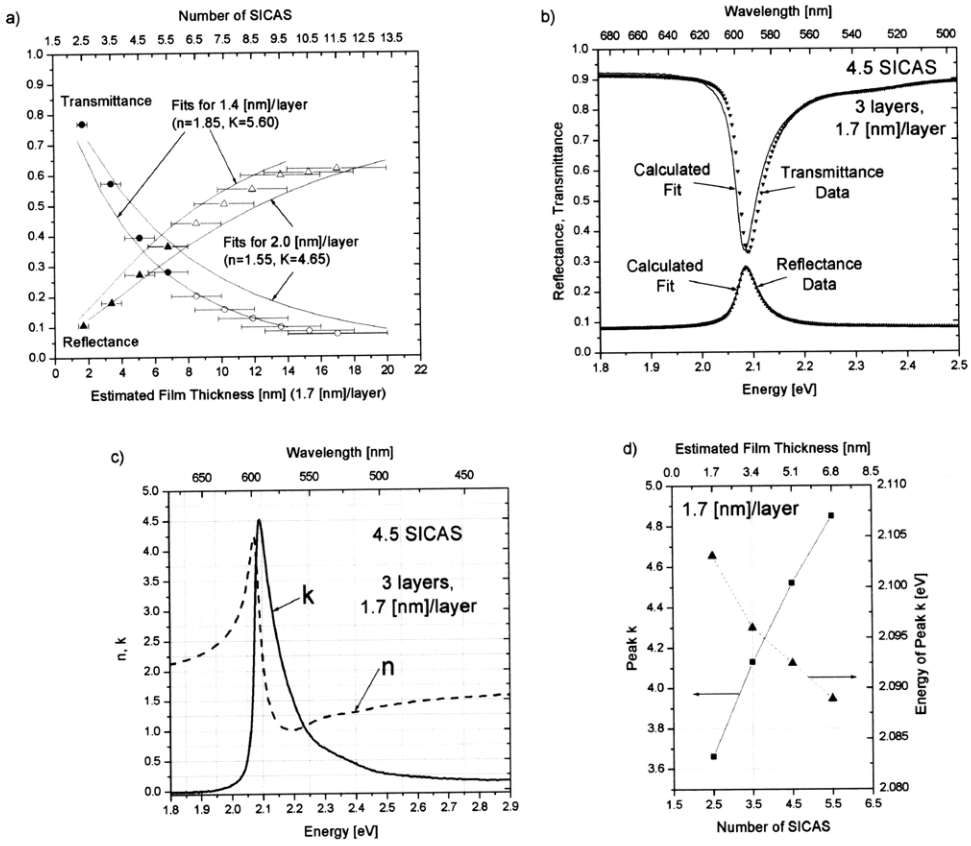

Figure 2-6: Plot (a) shows the transmittance and reflectance data at wavelength $\lambda = 596$ nm plotted versus film thickness, along with fits from the LDT model. The fits are based exclusively on the first four (filled) data points where layered growth is the dominant mode of film formation. Consequently, for thicker films (outlined data points) where SK-type growth is dominant, the thickness shown along the x-axis is to be interpreted as the AFM determined thickness estimate for the layered portion, and not the SK portion, of the film. The two fits plotted show the range in the complex index of refraction. Plot (b) shows measured reflectance and transmittance for 4.5 SICAS (5.1 nm thick film, 3 layers with 1.7 nm per layer) and calculated spectra using the (n,κ) shown in Plot (c). Plot (c) shows (n,κ) for the 4.5 SICAS film in (b) obtained through a Kramers-Krönig regression based on reflectance data. Plot (d) shows the range of the peak in κ for 2.5 SICAS to 5.5 SICAS films using Kramers-Krönig regression as well as the position of the peak in κ versus energy, assuming a thickness of 1.7 nm per layer.

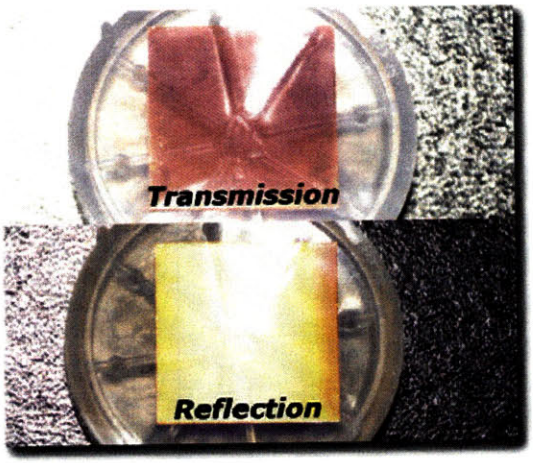

Figure 2-7: Photograph of a > 25 SICAS (thickness $d \approx 50$ nm) film of PDAC/TDBC J-aggregates in transmission and reflection.

increases, resulting in a higher κ for the films as more layers are added. Additionally, a larger reflectance FWHM will result from an increase in the splitting between the exciton-polariton longitudinal and transverse modes. Lastly, the high energy peak in absorption could be attributed to the exciton-polariton longitudinal mode. The observed trend in Figure 2-5(a) of the peak in reflectance moving to lower energy is consistent with both explanations. A weak cavity effect due to SK growth may be responsible for the small shift in the peak reflectance to lower energy as the cavity thickness increases. As Figure 2-7 shows, for a > 25 SICAS film (thickness $d \approx 50$ nm), the reflectance of the PDAC/TDBC J-aggregate thin film appears almost metallic due to the appearance of a polaritonic bandgap around the J-aggregate resonance frequency ($\lambda = 596$ nm (orange)).

In addition to the trends described above, another important piece of analysis is to determine how many TDBC dye molecules are present per unit volume in the LBL film. Based on the very large peak absorption constant derived, one can already conclude that a very high density of dye molecules must be present to provide such an amount of extinction. Using the Kramers-Krönig derived index of refraction, a variation of the sum rule for oscillator strength can be applied by comparing the integral of the extinction coefficient for the thin film to that of a known concentration

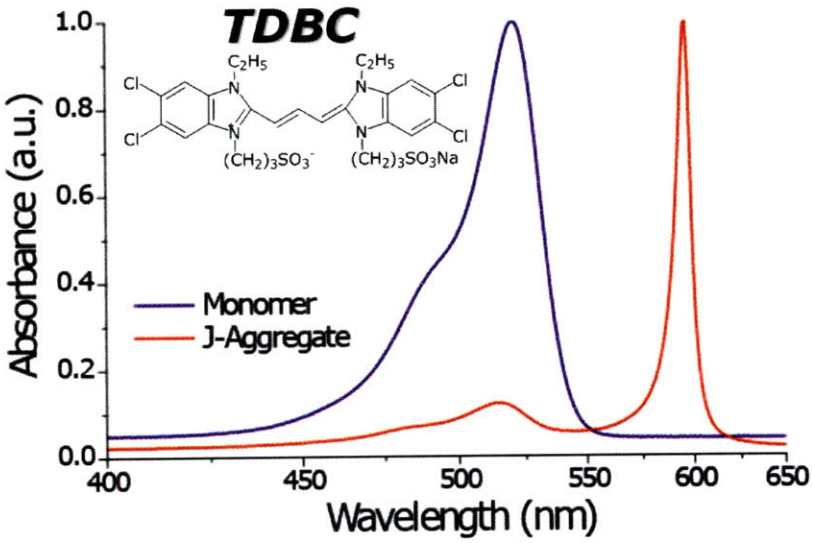

Figure 2-8: Absorbance of TDBC monomer and J-aggregate.

of monomeric dye in solution.[2] Figure 2-8 shows the absorbance spectrum of TDBC monomer and J-aggregate (absorbance is given by the Beer-Lambert Law, $Abs = \alpha L = \log_{10}(100/T)$, where T is the transmittance in %, α the absorption constant in cm^{-1}, and L the path length of light in cm).

First, we relate the absorption constant to the molecular absorption cross-section through:

$$\alpha(\omega) = N\sigma(\omega)$$

where N is the density of molecules per unit volume and $\sigma(\omega)$ the absorption cross-section (which has units of area). We find $\alpha(\omega)$ for the monomer by measuring a known concentration of TDBC monomer (e.g., in methanol or ethanol, TDBC does not aggregate, allowing for a simple absorbance measurement in a spectrometer). From the Kramers-Krönig regressions for the thin film, we can calculate $\alpha(\omega)$ using the relation $\alpha(\omega) = \frac{2\omega\kappa(\omega)}{c}$. With these two spectra in hand, we calculate the molecular density in the J-aggregate thin films by making the assumption from the sum rule

[2]One way of interpreting the oscillator strength sum rule is that oscillator strength is conserved as long as the transition dipole has not fundamentally changed. Interactions with the environment and other physical processes merely spread out the oscillator strength over a wider set of frequencies.

that $\int \sigma_{mon}(\omega)d\omega = \int \sigma_{J-Agg}(\omega)d\omega$:

$$N_{J-Agg} = \frac{N_{mon} \int \alpha_{J-Agg}(\omega)d\omega}{\int \alpha_{mon}(\omega)d\omega} \tag{2.4}$$

Carrying out the calculation in Eq. 2.4 indicates that the density of TDBC molecules in the LBL J-aggregate thin films is on the order of one to two molecules per cubic nanometer. Since organic dye molecules in an amorphous, thermally-evaporated film are usually assumed to be on the size scale of one cubic nanometer, such a density indicates that the J-aggregated TDBC molecules comprise a very high portion of the LBL thin film. This, ultimately, is advantageous from the perspective of strongly coupling these J-aggregates to a microcavity electric field to form exciton-polaritons since all of the J-aggregate dipoles can be placed at the microcavity anti-node and see the same electric field magnitude, reducing inhomogeneities caused by different amounts of coupling in different parts of the film.

LBL assembled thin films of PDAC/TDBC J-aggregates possess remarkable morphological and optical properties that make them well suited for use in strong coupling optoelectronic applications, enabling the creation of exciton-polariton optoelectronic devices that operate at room-temperature [189]. With LBL, J-aggregates form nanometer-scale physical layers, allowing highly absorbing thin films to be assembled with precision thickness control. Moreover, the high absorption constant of the PDAC/TDBC films, $\alpha = (1.05 \pm 0.1) \times 10^6$ cm^{-1} at $\lambda = 596$ nm, is a lower limit, as even higher absorption constant values could be obtained by developing full coverage of the substrate surface with similarly directed J-aggregate domains. In the next section, we will examine the transient properties of excitons in these LBL J-aggregate thin films through incoherent pump-probe measurements.

2.3 J-Aggregate Thin Film Nonlinear Optical Response

Throughout the 1990s and into the 2000s, the nonlinear optical response of J aggregates has attracted considerable attention in the research community due to the rich physics of exciton dynamics within the aggregates and interest in what energy transfer in J-aggregate systems might be able to teach us about the processes involved in photosynthesis in analogous biological systems [91, 92]. Additionally, in order to engineer organic exciton-polariton devices based on J-aggregates, we need to understand exciton dynamics in J-aggregate devices in order to predict the dynamics of exciton-polaritons (e.g., how exciton-polaritons will relax in the lower branch). Two experiments that afford considerable insight into the dynamics of excitons in J-aggregates are temporally-resolved photoluminescence at various temperatures and room-temperature incoherent pump-probe. Temporally-resolved photoluminescence (PL) versus temperature sheds light on the relaxation processes affecting excitons in LBL thin films of J aggregates and how the size of the coherence domain (N described in Section 1.3.1) changes as the temperature is changed. Incoherent pump-probe also provides insight into the relaxation dynamics of excitons, and additionally, as explained by van Burgel *et al.* [191], can be used to determine at a given temperature what the coherence domain is. By combining the two sets of data, the coherence domain can be determined at room temperature and extrapolated to lower temperatures based on the quantum efficiency and photoluminescence lifetime data provided by temporally-resolved photoluminescence measurements.

2.3.1 Setup of Spectroscopy Experiments

Figure 2-9 shows a diagram of the setup used for temporally-resolved PL measurements. The sample is placed in a cryostat, allowing the temperature to be swept from 300 K down to 5 K, and excited at an angle by a $\lambda = 532$ nm laser with pulse length 7 ps. The luminescence at normal angle is collected by a lens and passed through a

beam splitter, sending half of the emitted signal to a spectrometer and half to the streak camera. Prior to being focused onto the streak camera, the luminescence signal is reflected off of a grating, which spreads out the wavelengths of emitted light, allowing for both time and wavelength to be recorded by the streak camera. A similar setup is used in the pump-probe experiments, but in those experiments no cryostat is used, and the pump and probe beams are normally incident to the sample in a transmittance setup (i.e., the beams pass through the sample and are then collected). The pump pulse has a 100 fs pulse width and is centered at $\lambda = 545$ nm with a photon flux of 10^{14} cm^{-2} focused into a spot $10 - 100$ μm in diameter. The probe pulses used are of similar length as the pump, created from a white light source which is passed through a monochromator in order to enable scanning at different wavelengths. Due to the photobleaching of the TDBC molecules during the collection, the sample was scanned manually during the collection process to maintain sufficient signal.

Samples used in these measurements were produced using the same procedure outlined in Section 2.1.1. The measurements were performed without any additional package steps for the films, which for the pump-probe measurements would have provided a barrier to oxygen from the environment but not prevented bleaching due to oxygen dissolved in the remaining moisture in the films (i.e., strong polyelectrolytes such as PDAC are very hygroscopic, meaning that even after blow-drying samples with nitrogen considerable moisture remains in the film).

2.3.2 Temporally-Resolved Photoluminescence versus Temperature

The temporally-resolved PL is measured for a variety of temperatures from 5 K up to room temperature, 300 K, for a 6.5 SICAS PDAC/TDBC thin film. Figure 2-10 shows the spectrally-integrated PL intensity plotted versus time at the two extreme temperatures, 5 K and 300 K, along with a plot of the excitation response, showing the resolution available on the streak camera. The two decay curves show a bi-exponential form with almost identical time constants of 10 ps and 70 ps for the fast

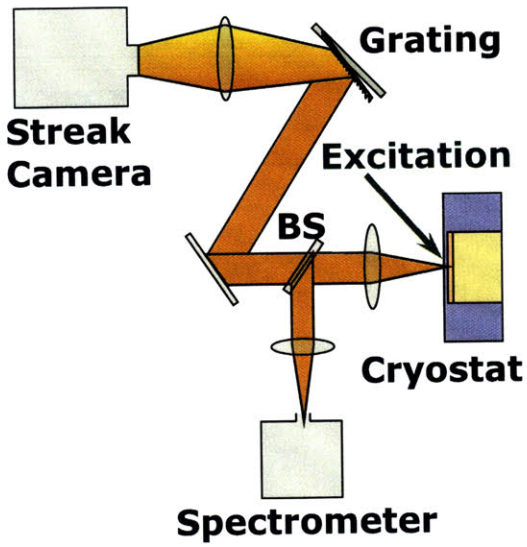

Figure 2-9: Temporally-resolved photoluminescence (PL) versus temperature setup. The sample is excited at an angle and the PL collected at normal. A beamsplitter (BS) is used to send half of the signal to a spectrometer and half to a streak camera. The emitted light is reflected off of a grating prior to entering the streak camera to enable both time and spectrally resolved measurement.

and slow components, respectively.

Figure 2-11 shows the measured time constants of the bi-exponential decay curves for the spectrally-integrated PL at temperatures between the two extremes shown in Figure 2-10. As suggested by the results shown in Figure 2-10, the time constants remain essentially unchanged regardless of temperature, and the ratio of the fast and slow exponentials also remains unchanged with varying temperature.

Varying the temperature of the sample does affect the temporally-resolved emission when spectrally-resolved, however, and additionally, the quantum efficiency of the J aggregates does vary with temperature, which is apparent when the PL intensities for different temperatures at the same input power level are plotted.

Figure 2-12 shows the temporally and spectrally-resolved PL measured at 5 K and 300 K. Additionally, the emission at the indicated wavelengths (denoted by $\lambda_{A...C}$ for the 5 K measurements and $\lambda_{D...F}$ for the 300 K measurements, respectively) is plotted versus time, showing that at low temperature a pronounced red-shift in emission takes place in the span of about 10 ps, whereas at room temperature this shift is immediate

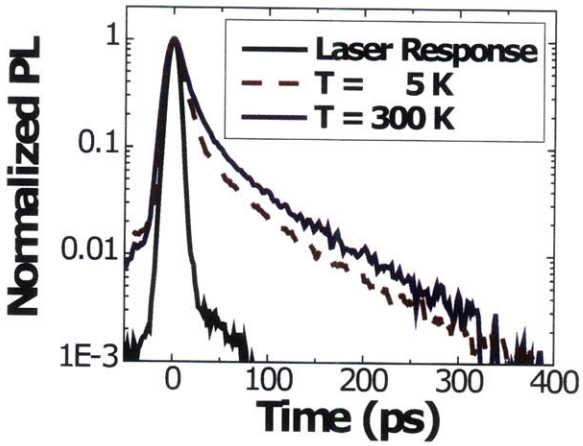

Figure 2-10: Normalized, spectrally-integrated PL decay for a 6.5 SICAS PDAC/TDBC thin film excited at $\lambda = 532$ nm. The 7 ps excitation, decay at 5 K, and decay at room temperature, 300 K, are plotted. The bi-exponential decay curves have time constants of 10 ps and 70 ps for the fast and slow components, respectively.

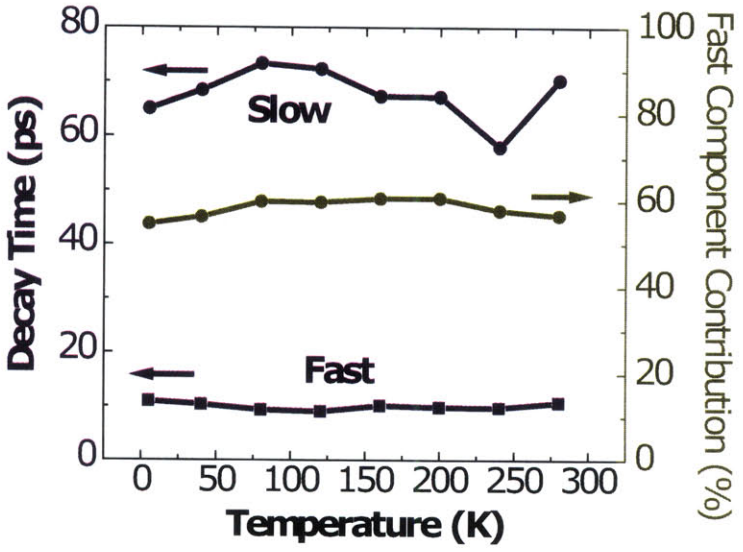

Figure 2-11: Time constants of bi-exponential decay of spectrally-integrated PL for 6.5 SICAS film at temperatures from 5 K up to room temperature, 300 K. The fast and slow components do not vary with temperature, and the ratio of the two emission components remains unchanged with varying temperature.

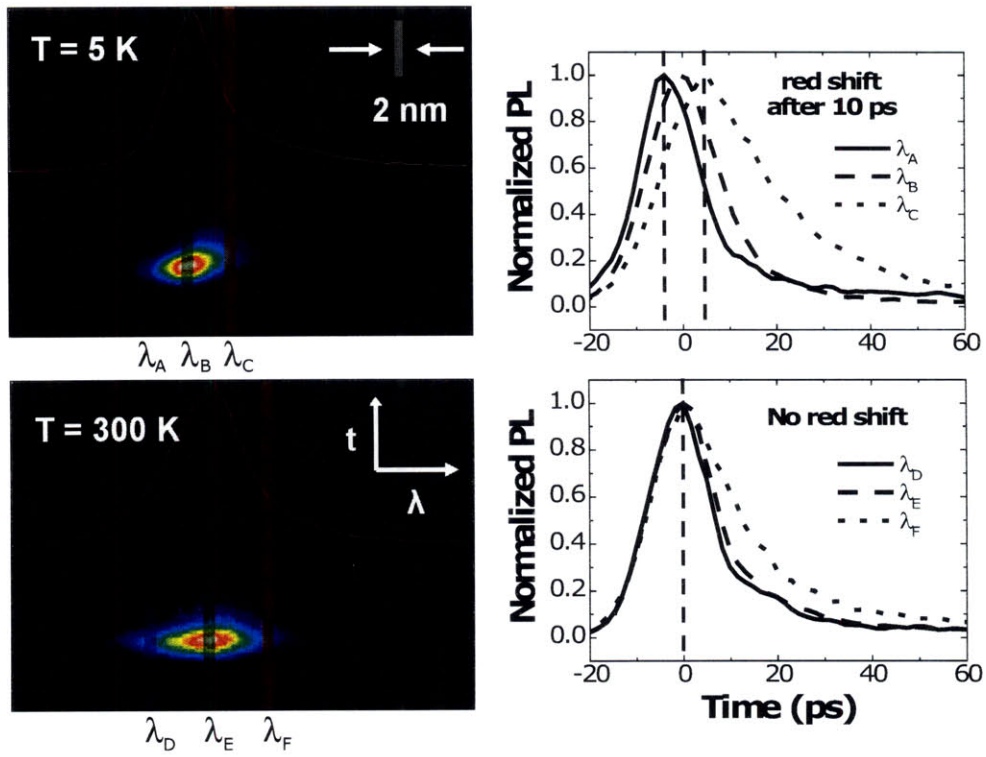

Figure 2-12: Temporally and spectrally-resolved PL at 5 K and 300 K. The PL at low temperature red-shifts considerably in a time span of roughly 10 ps. The PL at room temperature does not shift, but rather it overlaps both the initial and red-shifted PL at low temperature, indicating that any shift present is occurring under the resolution of the streak camera.

(i.e., under the resolution of the measurement setup); the PL at room temperature overlaps the initial and red-shifted emission at low temperature.

Finally, Figure 2-13 shows the measured spectrally-resolved intensity of PL over a range of temperatures at a constant input power. As the temperature is decreased, the PL intensity rises dramatically, indicating that the quantum efficiency of the J aggregates in the film is increasing.

2.3.3 Incoherent Pump-Probe Spectroscopy of Thin Films

Relating J-Aggregate Coherence Length to Transient Absorption Spectra

In their study of the 1D J-aggregate exciton model described in Section 1.3.1, van Burgel *et al.* [191] describes how incoherent pump-probe spectroscopy can be used to

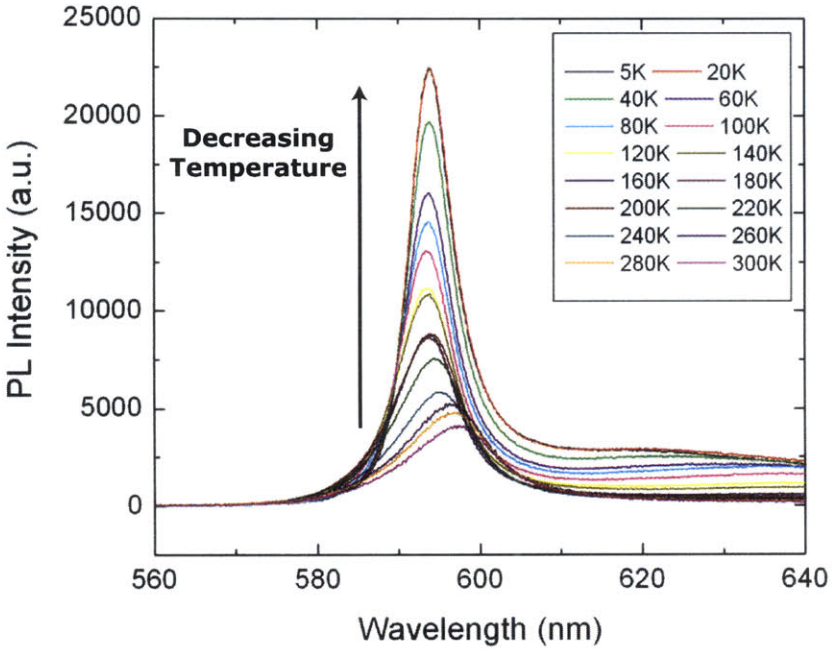

Figure 2-13: Spectrally-resolved PDAC/TDBC thin film photoluminescence intensity over a range of temperatures. An increase of the intensity and blue-shift of the PL peak occurs as the temperature is decreased from room temperature down to 5 K.

determine the coherence length of J aggregates (i.e., number of coherently coupled monomers in a J-aggregate, N). In the above study, the authors point out that due to Pauli exclusion, a second excitation on a given J aggregate cannot be placed in the same quantum state as the first excitation (i.e., with quantum number $k = 1$ the bottom of the J-aggregate band of states, the next excitation cannot also be placed in $k = 1$; instead, the lowest possible state of the second excitation is $k = 2$, the resulting state of which we will term $k_{ex1} = 1, k_{ex2} = 2$ to denote the presence of two excitons on a single aggregate).

Therefore, as per Eq. 1.19, the energy of the one-exciton to two-exciton (also referred to as a bi-exciton) transition will be higher than the ground state to one-exciton transition, the energy difference of which is given by [191]:

$$\Delta E_{abs} = E_{bleach} - E_{absorption} = 2V\left[\cos\left(\frac{\pi}{N+1}\right) - \cos\left(\frac{2\pi}{N+1}\right)\right] \approx \frac{3\pi^2 V}{(N+1)^2} \tag{2.5}$$

where E_{bleach} and $E_{absorption}$ are the bleached ground state to $k = 1$ absorption and induced $k = 1$ to $k_{ex1} = 1, k_{ex2} = 2$ absorption, respectively, and recalling that V, the nearest-neighbor coupling of the monomers, is negative for J aggregates. The above equation assumes that the k quantum states are orthogonal (i.e., non-interacting). One interesting interpretation of Eq. 2.5 comes from taking the limit of large N. As N becomes large, the change in energy ΔE_{abs} vanishes, meaning that the excitonic states of the J aggregate become more bosonic in character.

Utilizing Eq. 2.5, the coherence number N can be derived by measuring ΔE_{abs} from transient absorption spectra (i.e., incoherent pump-probe spectroscopy) and V from solution and/or thin film linear optical spectroscopy of monomeric and J-aggregated dye molecules. The resulting equation for N is:

$$N \cong \sqrt{\frac{3}{2}\pi^2 \frac{E_{J-Agg} - E_{mon}}{\Delta E_{abs}}} - 1 \tag{2.6}$$

where we have substituted for V through the relation $E_{J-Agg} \cong E_{mon} + 2V$. In the following section, the data from incoherent pump-probe spectroscopy of PDAC/TDBC

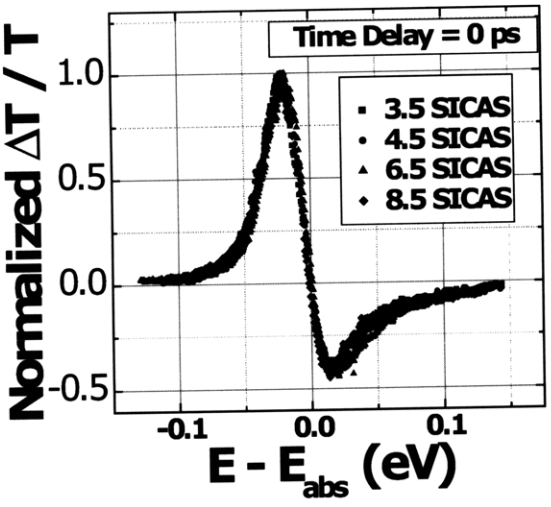

Figure 2-14: Normalized fractional change in transmittance, $\Delta T/T$, for a series of thicknesses of PDAC/TDBC LBL thin films. The widths and peaks of the induced and bleach absorption do not change with thickness, indicating that the energy levels in the J-aggregate exciton band in samples that underwent different numbers of SICAS are identical.

LBL thin films at room temperature will be presented, and N will be calculated using Eq. 2.6.

Results of Incoherent Pump-Probe Spectroscopy

Figure 2-14 shows the fractional change in transmittance, $\Delta T/T$, measured versus center wavelength of the probe pulse for a series of different thicknesses of PDAC/TDBC films.

The plots in Figure 2-14 indicate that the widths and peaks of the induced and bleached absorption in the $\Delta T/T$ response of different film thicknesses are nearly identical, from which we can conclude the the energy levels of the J-aggregate exciton band in films of different thicknesses are identical. For this reason, we will focus on analyzing the transient absorption spectra for the 4.5 SICAS sample.

Figure 2-15 shows the time decay of the $\Delta T/T$ signal for the 4.5 SICAS sample plotted for a variety of probe wavelengths and a plot of the time responses at $\lambda =$ 582 nm and $\lambda =$ 592 nm with derived time constants for the two fast components

from bi-exponential fittings.

Using one of the transient absorption spectra at a given time delay, we can fit Lorentzians to the induced and bleached absorption spectrum in order to determine the ΔE_{abs} parameter in Eq. 2.6 from the peaks of the fitted curves. Figure 2-16 shows such a fitting and the derived ΔE_{abs} for the 4.5 SICAS sample at a delay of 4 ps.

Using $\Delta E_{abs} = 16.5\,\text{meV}$ derived from the fittings in Figure 2-16 along with Eq. 2.6, the coherence length of J aggregates in LBL PDAC/TDBC films at room temperature is estimated to be $N \cong 16$, which is consistent with previous studies of similar J aggregates at room temperature [135, 191]. Since the coherence length at room temperature is generally limited by interactions with the environment (e.g., phonons in solid-state media), structural differences between J aggregates in different types of thin films or in solution are not likely to manifest themselves in the coherence length at room temperature. On the other hand, we can combine the measured coherence length at room temperature with the earlier data in Section 2.3.2 from temporally-resolved PL at different temperatures to determine the coherence length versus temperature for these PDAC/TDBC J-aggregate films.

2.3.4 Discussion of Time-Resolved PL and Pump-Probe Results

Calculating the Coherence Length versus Temperature

The time-resolved PL versus temperature data, shown in Figure 2-11, and PL intensity change with temperature data, shown in Figure 2-13, can be combined with the value of N determined at room temperature to estimate $N(T)$, which will indicate the extent of structural disorder in the thin films compared to the disorder in solution measurements from previous studies.

The general expression for quantum efficiency (i.e., fraction of input power radiated) and photoluminescence lifetime are related in that both are dependent on the radiative and nonradiative rates (or lifetimes). The quantum efficiency is given by:

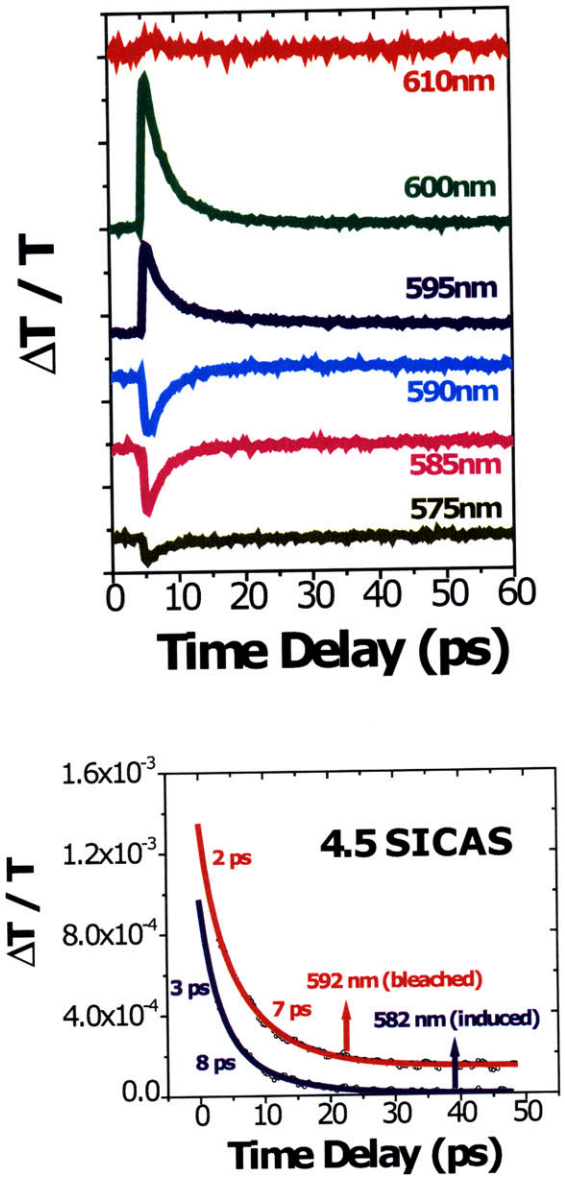

Figure 2-15: (Left) $\Delta T/T$ versus time for a 4.5 SICAS PDAC/TDBC LBL thin film at a variety of probe wavelengths. (Right) The $\Delta T/T$ transients at $\lambda = 582$ nm and $\lambda = 592$ nm, the peaks in induced absorption and bleached absorption, respectively. Fitting the transients with bi-exponentials yields almost identical time constants for the two fast components.

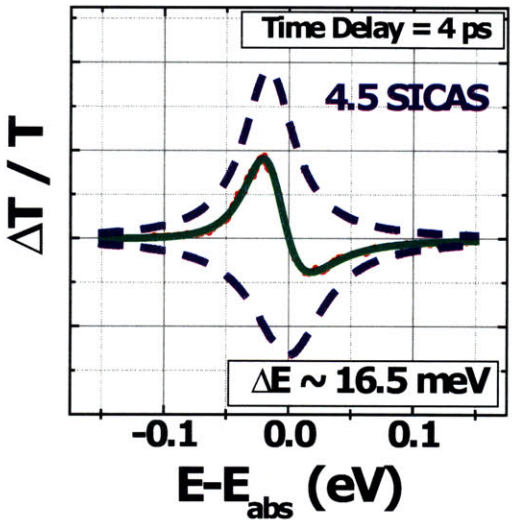

Figure 2-16: $\Delta T/T$ for 4.5 SICAS film at a probe delay of 4 ps. The induced and bleached absorption curves are fit with Lorentzians, the peaks of which give the energy difference ΔE_{abs}, from which the coherence length of the J aggregates at room temperature can be derived.

$$QE = \eta = \frac{\Gamma_R}{\Gamma_R + \Gamma_{NR}} = \frac{1/\tau_R}{1/\tau_R + 1/\tau_{NR}} \tag{2.7}$$

where $\Gamma_{R,NR}$ ($\tau_{R,NR}$) are the radiative and nonradiative rates (lifetimes) of exciton relaxation, respectively. The overall decay rate for exciton relaxation is simply the sum of the radiative and nonradiative rates:

$$\Gamma = \Gamma_R + \Gamma_{NR} = 1/\tau_R + 1/\tau_{NR} \tag{2.8}$$

where Γ is the overall rate that would be measured in temporally-resolved PL (i.e., the PL signal is a reflection of the population of excitons, which are decaying at the rate Γ).

As noted in Section 1.3.1, since the J-aggregate state has an oscillator strength roughly proportional to N, the radiative decay rate also scales directly with N, meaning we can write the radiative decay rate as $\Gamma_R \approx \Gamma_{R,mon} N$, where we have denoted the monomer radiative decay rate as $\Gamma_{R,mon}$. The expression is approximate since the actual expression (Eq. 1.21), although scaling with N, has a more complicated form.

Examining Figure 2-13, at 5 K the PL intensity peak is roughly 22500 counts (halfway between 20000 and 25000), whereas at 300 K the peak is at roughly 3750 counts (halfway between 2500 and 5000). Disregarding the slight peak shift and change in linewidth, the PL intensity at 5 K is roughly six times that at room temperature, which tells us that since we have the same input power, the quantum efficiency is also six times greater.

From Figure 2-11, it is evident that the PL decay rate, Γ, does not vary with temperature. If $\Gamma = \Gamma_R + \Gamma_{NR}$ is constant, then immediately we know from Eq. 2.7 that the radiative rate at 5 K must be six times that at room temperature since the nonradiative rate (which is part of the denominator in Eq. 2.7) factors out in the comparison. From this analysis, by substituting for Γ_R in terms of N, we can relate $N(5\text{ K})$ to $N(300\text{ K})$:

$$\begin{aligned} \Gamma_R(T = 5\text{ K}) &= 6\Gamma_R(300\text{ K}) \\ N(5\text{ K})\Gamma_{R,mon} &\approx 6N(300\text{ K})\Gamma_{R,mon} \\ N(5\text{ K}) &\approx 6N(300\text{ K}) \cong 6 \times 16 = 96 \end{aligned} \tag{2.9}$$

Although it may seem counterintuitive that the lifetime should stay constant despite a faster radiative decay rate at lower temperature, the result is consistent with the increase in quantum efficiency. As the temperature is lowered, the radiative rate does in fact increase, but this decrease in lifetime is countered by the removal of nonradiative pathways caused by decreasing the number of phonons present in the environment. It so happens in this case that the two effects exactly cancel out each other, resulting in a constant PL lifetime versus temperature.

The result of the above derivation is that we find that at 5 K, the coherence length of the aggregates has increased from $N \cong 16$ at room temperature to $N \approx 100$ at 5 K. Assuming each molecule in the film occupies about one cubic nanometer, this corresponds to a cube $3 - 4$ nm on a side.

Time Constants Found from Temporal PL and Pump-Probe Data

Finally, the time constants derived in the temporally-resolved PL and incoherent pump-probe experiments are worth noting. In the PL data, since the pump pulse was 7 ps in length, the only two time constants that could be derived were due to dynamics longer than the pump pulse (due to convolution of other processes with the response to the pump). However, since the pulse in the pump-probe experiments was much shorter, on the order of 100 fs, a third, shorter time constant was recorded.

The three time constants reported between the two sets of data (which we will label from shortest to longest) were $\tau_1 = 2 - 3$ ps, $\tau_2 = 7 - 10$ ps, and $\tau_3 = 70$ ps. The likeliest explanations for these three time constants follow.

Short of knowing a calibrated response time of the streak camera, τ_1, the shortest time constant, must be assumed to be a convolution of both ultrafast processes in the J aggregates and the streak camera response. Coherent processes in the J aggregates at room temperature likely have sub-picosecond decay times, which can be estimated from examining the linewidths of PL and absorption of the thin film. The PL linewidths measured are on the order of 10 nm, and in absorption, at lowest energy of absorption corresponding to the bottom of the J-aggregate band, a linewidth of at least a couple of nanometers is present. At the lower end of the J-aggregate absorption, one would expect a sharp cut-off with a linewidth on the order of the homogeneous linewidth as opposed to at higher energies, where the linewidth would be smeared by inhomogeneous broadening. From these estimates, therefore, the likely decay time of coherent processes in these J-aggregate thin films at room temperature is in the hundreds of femtoseconds at most, and the recorded time τ_1 is likely the contribution of these ultrafast processes combined with the response of the streak camera.

In the case of τ_2, in both the PL and time-resolved measurements this time is slower than any of the components involved in the measurement. One can therefore conclude that the time corresponds to a real physical process that excitons in the J aggregates are undergoing. A clue to the origin of this time constant can be found in Figure

2-12, where at low temperatures a red-shift in PL is observed that occurs on the same time scale as τ_2. If we assume that the red-shift is due to exciton diffusion within the J-aggregate thin film, as has been observed and modeled in other amorphous organic systems, then seeing the same time constant appear in fast exciton decay processes is not just consistent but expected [116]. The same process that allows excitons to hop from one J aggregate to another at slightly lower energy also allows two excitons to meet and annihilate. Therefore, the 10 ps time constant in the PL decay and pump-probe data can be attributed to exciton-exciton annihilation in the J-aggregate thin film.

Finally, this leaves τ_3, which at 70 ps is likely just the lifetime of the J-aggregate exciton. Just as the radiative decay rate at a given temperature will scale with N, the number of coherently coupled monomers in the J aggregate, one would also expect that nonradiative pathways would also have some sort of scaling with N since the nonradiative decay could occur on any of the N molecules over which the excitation is delocalized. Assuming these pathways are independent, the probability of nonradiative decay in a J aggregate would simply be the sum of the probabilities of decay from the individual molecules. With this assumption, Γ, the exciton decay rate would scale with the number of coherently coupled molecules, N, meaning that if $\tau_3 = 70$ ps is the exciton lifetime of a J aggregate, then the lifetime of an exciton for a single TDBC molecule is 16×70 ps, or about $1 - 1.5$ ns, which is consistent with the oscillator strength of a typical organic dye molecule and quantum efficiency of 10% (by comparison, for aluminum tris(8-hydroxyquinoline), a common dye used in OLEDs, the lifetime is slightly longer at a few nanoseconds, but the quantum efficiency is also higher, which is consistent since the higher efficiency indicates that the nonradiative exciton decay rate is smaller).

The measurements of thin film dynamics presented indicate that the structural disorder present in J aggregates in LBL thin films is the same as that seen in solution, where the disorder present in the self-assembly process of molecules in a J aggregate results in structural disorder that limits the coherence length to about 100 molecules, even at lower temperatures [91]. In the next chapter, the linear optical modeling

presented here will be extended to full device structures to determine the contribution of homogeneous versus inhomogeneous broadening to the measured optical response of the LBL J-aggregate films used in exciton-polariton devices.

Chapter 3

Engineering Linear Optical Properties

In the past two decades of research in strongly coupled solid-state devices, linear dispersion theory (LDT) has emerged as a powerful tool for modeling the linear optical response of exciton-polariton systems. LDT has been shown to be capable of accurately predicting the linear optical response of inorganic microcavity devices [18, 142, 195, 202], and while for organic devices some use of LDT has been made, no attempts at modeling the linear optical response included an exact index of refraction for the active layer (i.e., J aggregates, porphyrins, etc.). In this section, LDT is shown to accurately predict the linear optical response of microcavity exciton-polaritons in devices utilizing thin films of J aggregates when a detailed, spectrally-resolved optical response of the J-aggregate resonance is utilized in the model.

Using a model-free, Kramers-Krönig regression the spectrally-resolved index of refraction of the J-aggregate thin film is derived and used in an LDT model (i.e., in propagation and matching matrices, or T-matrices) together with published values for the dielectric functions of microcavity spacer and mirror materials. Agreement of the predicted and measured linear optical response is shown for various thicknesses of J-aggregate thin films matching the exciton-polariton dispersion as a function of the in-plane wave-vector (i.e., corresponding to external probe angle). By numerically simulating cavities with high quality factors and multiple J-aggregate layers, the Rabi

splitting can be made large enough such that the lower-branch (LB) exciton-polariton peak is in the Lorentzian tail of the dielectric function, allowing for an estimate of the minimum linewidth achievable for the LB exciton-polariton in TDBC J-aggregate systems, which is a reflection of the homogeneous linewidth of the J-aggregate excitons [69].

3.1 Linear Dispersion Theory (T-Matrices)

Previous efforts in modeling exciton-polariton systems with LDT have included using an exact dielectric function for an inorganic quantum well system in order to accurately model the effects of structural disorder on the linear optical response [89, 126]. Similarly, prior modeling of the linear optical response of J-aggregate microcavity exciton-polariton devices has largely followed the same LDT methods but never using an exact spectrally-resolved complex dielectric function [29, 187, 189, 193]. An approximate J-aggregate dielectric function was used in fitting the optical spectra of complete devices necessitating that one or multiple artificial "shoulder states" be added to approximate the significant asymmetry of the observed upper-branch (UB) and LB exciton-polariton linewidths [6].

While the use of approximate dielectric functions can be suitable in providing rough guides for device engineering (e.g., for choosing layer thicknesses to achieve a microcavity resonance at the right energy), if one is concerned with finding parameters from linear optical measurements for modeling the dynamics of exciton-polaritons in high-quality cavities, simply fitting one or two dielectric functions to the active layer response can be misleading. This is particularly true for J aggregates, whose oscillator strength, as described in Section 1.3.1, is distributed in such a way that the dielectric response is very asymmetrical (i.e., there is a sharp cut-off in the oscillator strength at low energies and a high-energy tail that significantly broadens the high-energy side of the dielectric response). The overall response is additionally broadened by the presence of inhomogeneities in the thin film; one likely culprit of the inhomogeneous broadening is solid-state solvation, where shifts in exciton transition energy

levels within a solid are caused by each dipole having a slightly different background dielectric due to the random orientation of neighboring dipoles [117].

One can take, for example, the dielectric function from Chapter 2 derived via Kramers-Krönig regression for a 4.5 SICAS PDAC/TDBC film and fit a simple Lorentzian to the response–such a fitting would likely match the result of fitting a Lorentzian to ellipsometry or reflectance/transmittance data from the thin film. Figure 3-1 shows this fitting (dashed line) compared to the imaginary part of the dielectric function calculated from the Kramers-Krönig-derived index (solid line) (i.e., $\epsilon_i = \Im(\epsilon)$, where we calculate the dielectric function from the complex index derived via Kramers-Krönig regression, $\epsilon = (n + i\kappa)^2$).

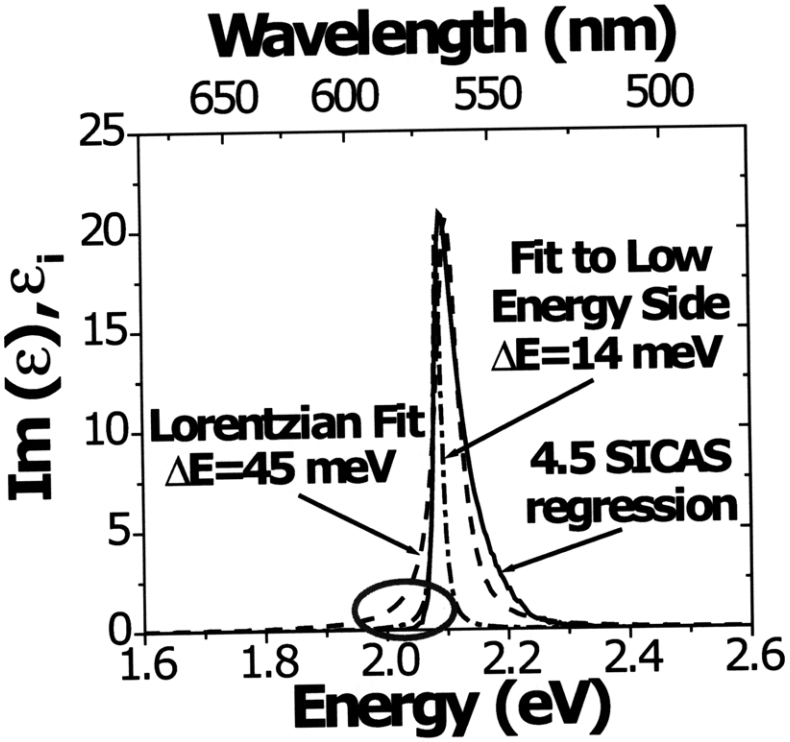

Figure 3-1: Lorentzian fittings to Kramers-Krönig-derived imaginary part of the dielectric function of a 4.5 SICAS film. The dashed line is a fit to the entire imaginary part of the dielectric function, whereas the dash-dot line is a fit only to the low energy side. The gray circle shows the considerable difference on the low energy side of the response between the two fits.

While the fitting seems to be quite good, a few important differences between the two are noticeable, especially on the low-energy side of the J-aggregate response,

and these differences turn out to be quite important when the LB cavity exciton-polariton is the focus, as is almost always the case when trying to build a laser or switch which utilizes the LB exciton-polariton. If we instead fit a Lorentzian only to the low-energy side of the Kramers-Krönig-derived dielectric function, we find that the linewidth of the inhomogeneous broadening captured by the first fitting is much different than the underlying homogeneous linewidth of the aggregate. This fitting is also shown in Figure 3-1 (dash-dot line). The linewidth of the Lorentzian fit to the whole response is 45 meV, which corresponds to about 13 nm, whereas the linewidth of the Lorentzian fit to the low-energy side of the response is about 3 times smaller at 14 meV, which corresponds to about 4 nm. Judging by this difference, we would expect the homogeneous linewidth of the J aggregates to be on the order of a few nanometers, whereas the inhomogeneous linewidth is on the order of $10 - 20$ nm.

With these fittings in mind, having the ability to exactly model the dielectric response of the J-aggregate film not only provides greater accuracy when engineering the linear optical properties of an exciton-polariton device, but in addition important characteristics of the linear response, such as linewidth, of the LB exciton-polariton are correctly modeled.

LDT modeling, as described in Chapter 2 where it was used to derive the index of refraction of a J-aggregate thin film through Kramers-Krönig regression, makes use of the boundary condition present in Maxwell's equations that states that the tangential electric field at a boundary must be continuous. From this boundary condition, the forward and reverse-propagating electric fields can be related to the fields across a boundary and across a film. These relationships are expressed mathematically in matrix form as "matching" matrices and "propagation" matrices, generally referred to at "transfer matrices" or "T-matrices." Figure 3-2 relates the physical elements of a multilayer stack of materials to their mathematical representations in an LDT model.

With a wave incident from the left, numbering layers as $1, 2, \ldots N_{layers}$, the total transfer matrix relating the incident field at the left to that exiting at the right is (the transfer matrices are denoted by $\mathbf{T}$, as opposed to T, which we will use shortly

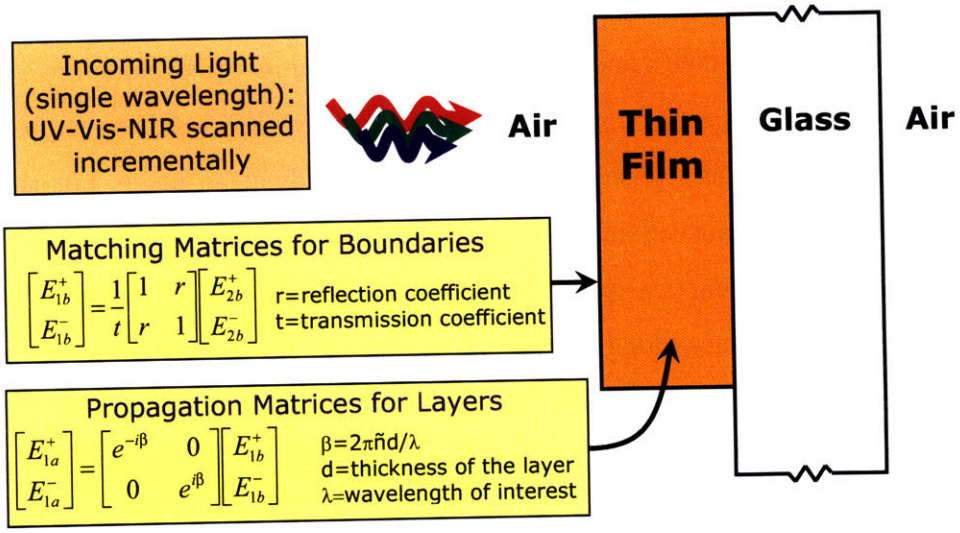

Figure 3-2: Physical elements of a multilayer dielectric stack and their respective T-matrix representation.

to denote transmittance, or transmitted power/intensity):

$$E_1^{\pm} = \mathbf{T}_{total} E_N^{\pm} = \mathbf{T}_{1,2}^{match} \times \mathbf{T}_2^{prop} \times \mathbf{T}_{2,3}^{match} \times \mathbf{T}_3^{prop} \times \ldots \mathbf{T}_{N-1,N}^{match} E_N^{\pm} \tag{3.1}$$

We solve for the field $E_1^{\pm}$ assuming that $E_N^+ = 1, E_N^- = 0$ (arbitrarily setting phase to zero and magnitude of exiting forward wave to 1 and specifying no reverse wave incident on the last layer). We can then calculate reflectance by $R = \frac{|E_1^-|^2}{|E_1^+|^2}$ and transmittance by $T = \frac{\eta_1 |E_N^+|^2}{\eta_N |E_1^+|^2}$, where η is the impedence of the medium in the direction of propagation normal to the dielectric stack. For a normally incident wave to the stack, in layer i, $\eta_i = \sqrt{\frac{\mu_i}{\epsilon_i}}$. The angular correction will be given below.

The variables r and t represent the reflection and transmission coefficients calculated from Fresnel's equations, the various E's are the complex electric field magnitudes (i.e., in phasor form, the complex magnitude contains both the magnitude and relative phase), and $\beta = 2\pi\tilde{n}d/\lambda$ is the complex wave-number lumped together with the thickness of the film through which the wave is propagating.

T-matrices can be made quasi-2D in that they can be made to handle fields im-

pinging on a stack at an angle by adjusting the reflection and transmission coefficients to include angular dependence and adjusting the wave-number to exclude the component of the wave propagating tangential to the boundary. The resulting expressions can be used to obtain the transmitted and reflected fields at an angle, but they do not account for the distance along the boundary that the wave traverses while going through the stack (for practical purposes such as measuring angular reflectance in a spectrometer, this distance along the boundary is small enough for most structures as to be negligible in aligning the setup).

After taking into account the above angular considerations, the resulting adjusted T-matrices for tranverse electric (TE) and transverse magnetic (TM) polarizations are given below, using the notation of Kong [93], assuming that the normal direction to the dielectric stack is $\hat{x}$ and parallel direction is $\hat{z}$, and given that a wave incident on the top of the stack is traveling in the $+\hat{x}$ direction.

The propagation matrix adjusted for angle is:

$$\begin{bmatrix} E_{1a}^{+} \\ E_{1a}^{-} \end{bmatrix} = \begin{bmatrix} e^{-ik_x d} & 0 \\ 0 & e^{ik_x d} \end{bmatrix} \begin{bmatrix} E_{1b}^{+} \\ E_{1b}^{-} \end{bmatrix} \tag{3.2}$$

where for an incident angle from air of θ, $k_x = \sqrt{k^2 - k_z^2} = \sqrt{\tilde{n}^2 k_0^2 - k_0^2 \sin^2\theta}$.

The matching matrix at a boundary has the same form as before:

$$\begin{bmatrix} E_{1b}^{+} \\ E_{1b}^{-} \end{bmatrix} = \frac{1}{t} \begin{bmatrix} 1 & r \\ r & 1 \end{bmatrix} \begin{bmatrix} E_{2b}^{+} \\ E_{2b}^{-} \end{bmatrix} \tag{3.3}$$

but the r's and t's are adjusted for angle and depend on polarization. With the notation of Kong [93] at a boundary where a wave is incident from medium (1) to medium (2):

$$r = \frac{1 - p_{12}}{1 + p_{12}} \tag{3.4}$$

$$t = \frac{2}{1 + p_{12}} \tag{3.5}$$

and p_{12} depends on polarization:

$$p_{12,TE} = \frac{k_{2x}}{k_1 x} \tag{3.6}$$

$$p_{12,TM} = \frac{k_1^2 k_{2x}}{k_2^2 k_{1x}} \tag{3.7}$$

It is important to note that for TM-polarization, the coefficients actually relate magnetic fields, H, and not E fields. For the purposes of calculating power flow (i.e., reflectance, transmittance, absorption), this distinction is irrelevant, but if one is examining specifically the fields in a structure, the E fields in the TM case must be calculated from the H fields given by the T-matrices. Since the transmittance T depends on η in the direction of the normal to the dielectric stack, we can correct transmittance with the following formula (this is only necessary to calculate transmittance when the final and beginning media are not the same):

$$T_{TE\ or\ TM} = p_{1N,TE\ or\ TM} \frac{|E_N^+|^2}{|E_1^+|^2} \tag{3.8}$$

Finally, as described in Chapter 2, to account for the effects of thick, transparent substrates on transmittance measurements, an averaging method was developed to incorporate internal reflections within the substrate that are not dependent on interference effects (e.g., over a millimeter-thick glass substrate, interferences between the two faces of the glass are averaged out in a typical sample spot size due to inhomogeneities in the glass that scramble the phase of the light as it traverses the substrate and to the low coherence length of most incident light sources). To perform this averaging, at each wavelength at which the reflectance and transmittance are computed, multiple computations are made in which the thickness of the substrate is adjusted to give a phase change of 0 to 2π to the light; these reflectances and transmittances are then averaged to give the final result. Using 10 to 100 points of averaging was found to give the best results without too much of a sacrifice in computation time (i.e., greater numbers do not provide much change in the result yet

require more computation time). If the transmittance calculation is insignificant, as is the case for the calculated reflectance dispersions later in this section, this averaging is unnecessary–the substrate can simply be modeled as an infinite medium.

3.2 Experimental Details–Device Structure and Materials

The microcavity exciton-polariton device structures tested in this section are shown in Figure 3-3 together with optical probe geometry.

The structures are grown on 14.5-pair distributed Bragg reflectors (DBRs) on SiO_2 (silica) substrates obtained from Visimax Technologies. The DBRs consist of pairs of plasma-enhanced-evaporated TiO_2 (titania) and SiO_2, starting and ending on TiO_2. The bottom microcavity spacer consists of an RF-sputter-deposited layer of SiO_2 of quarter-wavelength thickness, $\lambda/4n_{SiO_2}$, at the free-space wavelength $\lambda = 595$nm, which corresponds to the main exciton resonance of the TDBC J-aggregate thin film. Using the ellipsometry-measured index of refraction $n_{SiO_2}(\lambda = 633\text{nm}) = 1.456$, the SiO_2 spacer is grown to 102.1nm thick. The J-aggregate thin film is LBL deposited with the substrate undergoing varying numbers of SICAS. The cationic solution is a 30mM solution of PDAC (poly(diallyldimethylammonium chloride), CAS 26062-79-3, obtained from Sigma Aldrich) in deionized water. The anionic solution is a 50μM solution of the J-aggregating cyanine dye TDBC (or BIC) (5,6-dichloro-2-[3-[5,6-dichloro-1-ethyl-3-(3-sulfopropyl)-2(3H)-benzimidazolidene]-1-propenyl]-1-ethyl-3-(3-sulfopropyl) benzimidazolium hydroxide, inner salt, sodium salt, CAS 28272-54-0, obtained from Nippon Kankoh Shikiso Kenkyusho Co., Ltd.). The J-aggregate thin film deposition process and the thin film morphology are detailed in Chapter 2. For different substrates, the number of SICAS is varied from 4.5 (ending with an immersion in PDAC) to 8.5. The top spacer consists of a thermally-evaporated film of Alq_3 (aluminum tris(8-hydroxyquinoline)), a common molecular thin film used in organic light emitting devices. The thickness of Alq_3 depends on the corresponding number of SICAS

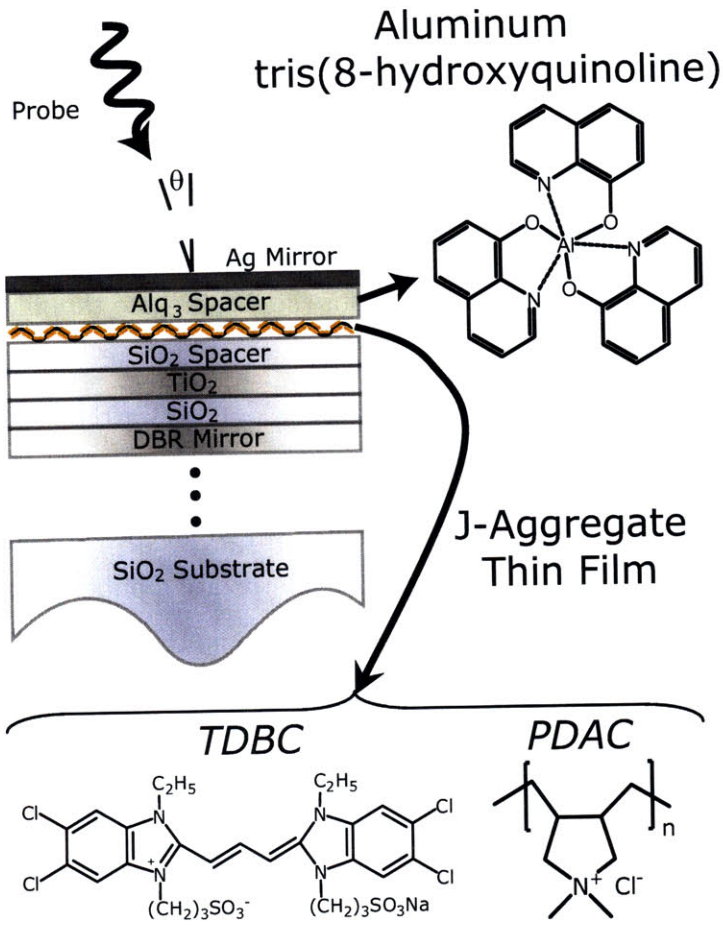

Figure 3-3: Device structure and materials. The microcavity mirrors are comprised of a thin silver mirror on the top of the device through which the optical response is probed and a 14.5 pair TiO_2/SiO_2 (titania/silica) distributed Bragg reflector (DBR). The active layer is a thin (5 – 12nm) layer-by-layer (LBL) film of cationic PDAC and anionic, J-aggregated TDBC. The bottom microcavity spacer is a sputtered SiO_2 film, and the top cavity spacer is an evaporated Alq_3 film.

of J-aggregate film, with (61.5, 59, 56.5)nm used for (4.5, 6.5, 8.5) SICAS, respectively. Finally, the top semi-transparent mirror consists of a 42.5nm, thermally-evaporated film of silver.

The optical constants of the TDBC J-aggregate thin films used in the exciton-polariton devices are measured on glass microscope slides that underwent the same numbers of SICAS concurrently with the microcavity device DBR/SiO_2 substrates. The reflectivity of these J-aggregate films is measured using a Cary 5E UV-Vis-NIR spectrometer and spectral reflectance accessory with film thicknesses based on the

AFM data shown in Chapter 2. The complex spectrally-resolved index of refraction ($\tilde{n} = n + i\kappa$) is then determined using a quasi-Kramers-Krönig regression [23]. The thin film reflectivity measurements and derived indices of refraction for $(4.5, 6.5, 8.5)$ SICAS films are shown in Figure 3-4(a), where the thicknesses used for the three films are $(5.1, 8.5, 11.9)$nm, respectively.

Using the derived indices of refraction for the J-aggregate thin films with varying numbers of SICAS, the linear optical response of the complete microcavity exciton-polariton device can be engineered. We use $n_{SiO_2} = 1.462$ for the SiO_2 layers, both in the DBR and bottom spacer; $n_{glass} = 1.5$ for the substrate; and for the Alq_3 top spacer layer and TiO_2 layer, we use published indices of refraction [31, 115]. The index of refraction for the silver mirror is obtained by interpolating published reference values [103]. The results of our LDT T-matrix simulations and the corresponding reflectivity measurements are shown in Figure 3-4(b) in the region of the UB and LB exciton-polaritons at an angle of $\theta = 7°$.

For the best match between the numerical analysis and the experimental measurements in the T-matrix simulations in Figure 3-4, the Alq_3 thicknesses used are 65, 62.5, and 60nm for the 4.5, 6.5, and 8.5 SICAS samples, respectively. Additionally, a thickness of 32nm is used for the top silver mirror. The discrepancies of 4.5nm in the Alq_3 thicknesses and 10.5nm in the silver thickness are likely due to penetration of the evaporated silver into the Alq_3 layer during growth. Accounting for these discrepancies results in a very good fit of the predicted linear optical response to the measured spectra.

3.3 Predicting Reflectivity Dispersion of J-Aggregate Cavity Exciton-Polaritons

With the derived index of refraction for the J-aggregate thin film and the quality of the linear optical response fit indicated in Figure 3-4, we can calculate detailed microcavity exciton-polariton reflectivity dispersion relations for the TE and TM

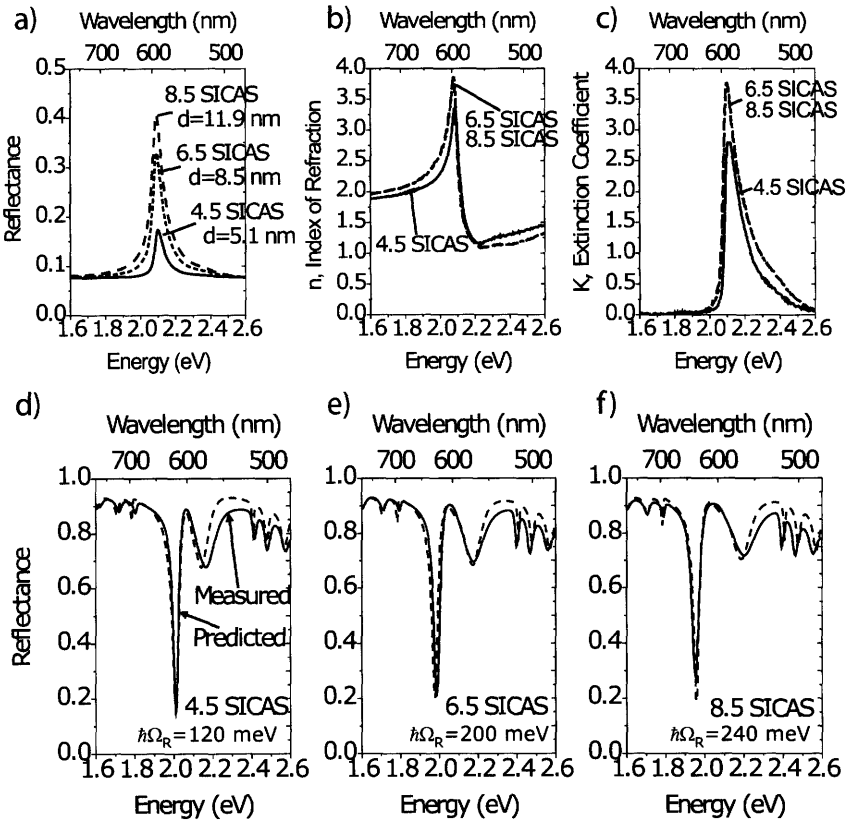

Figure 3-4: (a) Thin film reflectance. (b) Real and (c) imaginary (extinction coefficient) parts of index of refraction of J-aggregate thin films derived using Kramers-Krönig regression. The film thickness estimates, based on a previous study, are indicated [23]. The change in the index of refraction indicates that the dye concentration changes in the film as substrates undergo more SICAS. (d, e, and f) Comparison of measured and predicted reflectance spectra for complete devices using the indicated number of SICAS of PDAC/TDBC as the active layer. The predicted reflectance spectra are calculated using the complex indices of refraction and estimated thicknesses along with published dielectric functions for TiO_2 and Alq_3 and $n_{SiO_2} = 1.462$ [115, 157]. The indicated Rabi splittings are calculated from the coupled harmonic oscillator eigenenergy dispersion given in Eq. 1.6 using the angular dispersion of the predicted reflectance.

modes of the Figure 3-3 devices. The results of these calculations are plotted in Figure 3-5. By comparing the numerically-derived TE plot to the eigenenergies of the strongly-coupled exciton-microcavity system (given by Eq. 1.6 and disregarding

the linewidth terms:

$$E_{\pm} = \frac{E_{cav} + E_{ex}}{2} \pm \frac{1}{2}\sqrt{(\hbar\Omega_R)^2 + (E_{cav} - E_{ex})^2}$$

where E_+ and E_- are the UB and LB exciton-polariton energies, respectively, E_{cav} and E_{ex} are the cavity and exciton energies respectively, and Ω_R is the Rabi splitting), we can derive the value for the Rabi splitting in each system [195]. The cavity energy versus external angle, θ, is given by Eq. 1.4, reproduced here:

$$E_{cav} = \frac{E_{cav}(\theta = 0)}{\sqrt{1 - \frac{\sin^2\theta}{n_{eff}^2}}}$$

where n_{eff} is the effective cavity index of refraction. For the TE fitting in Figure 3-5, $n_{eff} = 1.7$.

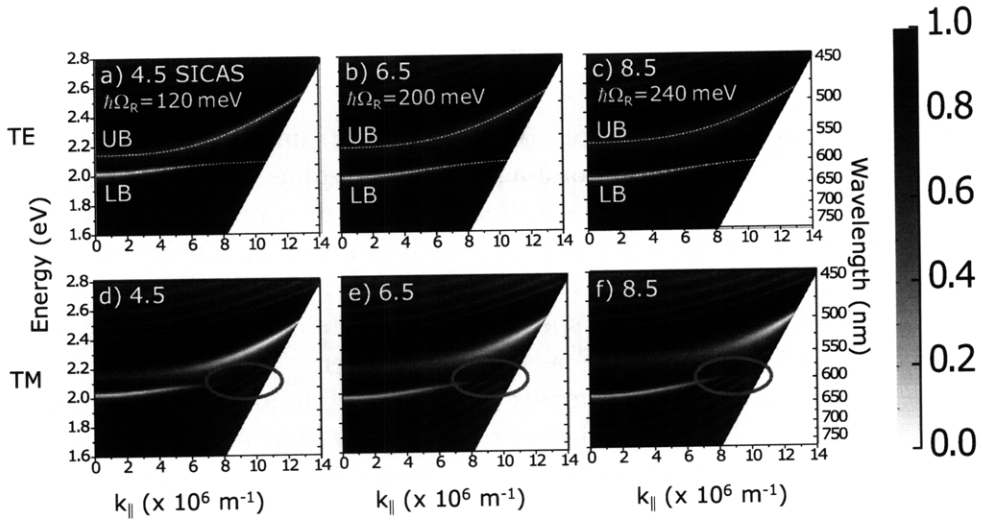

Figure 3-5: Predicted reflectivity of (4.5, 6.5, and 8.5) SICAS device versus in-plane wave-vector (i.e., external probe angle) for TE (a, b, and c) and TM (d, e, and f) polarization, respectively. The predictions are calculated using Kramers-Krönig-derived optical constants of the respective J-aggregate active layer, shown in Figure 3-4(b, c). The TE-polarized spectrum is shown with a fit to the general two-level-system eigenenergies. In TM polarization, due to the narrowing of the DBR stop band and the large Rabi splitting, the first few Bragg modes of the DBR cross the exciton resonance at large angles [150, 158].

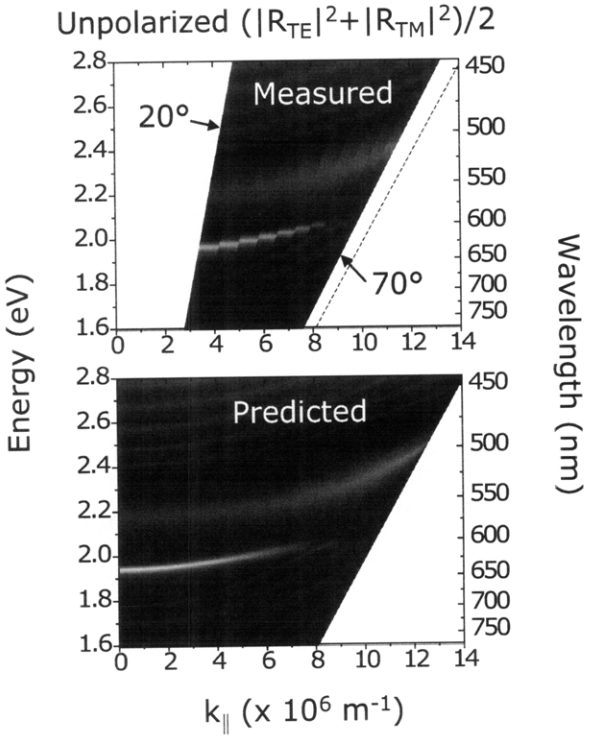

Figure 3-6: Comparison of measured and predicted unpolarized reflectivity for 8.5 SICAS sample (50% TE and 50% TM).

Notably, in the TM dispersion, narrowing of the DBR stopband at large angles results in the first few Bragg modes crossing through the exciton resonance, as previously described by Savona *et al.* and shown in CdTe inorganic microcavities by Richard *et al.* [150, 158]

The unpolarized reflectivity versus angle is measured for the microcavity samples using a Cary variable-angle spectral reflectance accessory to verify the accuracy of the T-matrix-calculated exciton-polariton dispersion relation (see Figure 3-4 for the 8.5 SICAS sample's measured optical data). The results are plotted in Figure 3-6. The predicted reflectivity dispersion relation (for unpolarized light, given by assuming 50% TE and 50% TM incident light) shows good agreement with the measured reflectivity, including the splitting of the TE and TM modes at large angle and the crossing of the first few Bragg modes in TM with the J-aggregate exciton resonance at $\lambda = 595$nm.

3.4 Simulating Complex Device Structures

As mentioned earlier in this chapter, LDT coupled with an exact dielectric function of the J-aggregate active layer can enable one to design and investigate the linear optical response of complex structures. This is especially useful in cases where using a simpler model of the dielectric function would not accurately describe the lower-branch exciton-polariton's response. Additionally, these complex structures may not currently be feasible with existing fabrication technology, meaning that the ability to simulate the devices can aid in deciding which fabrication methods should be developed next (e.g., integrating J-aggregate thin films and other organic materials in device structures where sputtering on top of the organic layer is required can be particularly challenging).

One such example of a complex device simulated using LDT and the exact dielectric function of the J-aggregate is presented here. By numerically simulating a high quality factor cavity utilizing multiple J-aggregate layers, we can extract a theoretical limit for the lower branch linewidth of devices utilizing the TDBC LBL J-aggregate thin films. As demonstrated by Houdre *et al.*, for large values of Rabi splitting, the exciton-polariton resonances are spectrally separated from the inhomogeneously broadened exciton resonance, such that the linewidths of the polariton resonances are determined by the homogeneously broadened tails of the exciton dielectric function [69]. By using dispersion-free spacer layers, three 6.5 SICAS J-aggregate layers, and two high quality DBR mirrors in a simulated cavity shown in the inset of Figure 3-7, we calculate the absorption of the structure (plotted in Figure 3-7) and find a theoretical LB exciton-polariton linewidth of 8.4meV (cavity $Q > 3000$, determined by simulating without the J-aggregate layers). This linewidth value is two to three times smaller than those used in recent theoretical papers on J-aggregate exciton-polaritons [4, 114, 129, 191]. Significantly, this value for the lower polariton linewidth is consistent with the linewidth for the Lorentzian in Figure 3-1 fit to the low-energy side of the dielectric response function, which was about 14 meV–the linewidth of the coupled light-matter system on resonance is simply the average of the linewidth of

the cavity and the linewidth of the exciton transition coupled to the cavity. Since $\gamma_{cav} \ll \gamma_{ex}$ for this cavity, the polariton linewidth should be about $\frac{1}{2}\gamma_{ex}$.

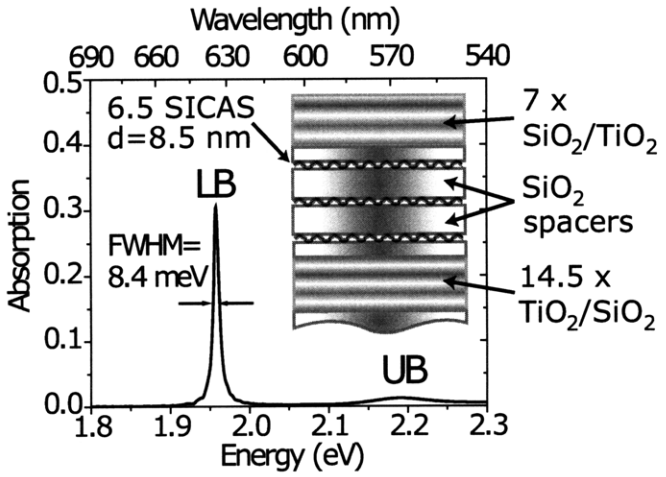

Figure 3-7: Simulated absorption spectrum of lower and upper branches for device structure in the inset, using dispersion-free SiO_2 spacer layers and the 6.5 SICAS layer properties from Figure 3-4(a). With a high quality microcavity ($Q > 3000$) and large Rabi splitting ($\hbar\Omega_R = 220$meV) from multiple J-aggregate layers at cavity anti-nodes, a theoretical linewidth of 8.4meV for the lower branch can be achieved.

As demonstrated, LDT can accurately model the linear optical properties of strongly coupled J-aggregate microcavity exciton-polariton devices when the spectrally-resolved complex index of refraction is utilized. Using a model-free Kramers-Krönig regression, the J-aggregate thin film index of refraction is accurately determined and then combined with published dielectric functions for the other microcavity device constituents to accurately predict the linear optical response of J-aggregate microcavity exciton-polariton devices. This demonstrates that the LDT method is a valuable theoretical tool for deriving the minimum exciton-polariton linewidth in J-aggregate-based devices, a key parameter for modeling dynamics, and can assist in design of the next generation of strongly-coupled J-aggregate structures that exhibit giant Rabi splitting.

Having fully explored the linear optical response of J-aggregate thin films on their own and in device structures, we now return to examining the dynamics of excitations that we began in Section 2.3. With the techniques developed in the investigation of linear optical properties and knowledge of the dynamics provided by

photoluminescence and pump-probe spectroscopy, we can begin to examine in organic strongly-coupled systems the device physics discussed in the theory of operation of polariton lasers (Section 1.2).

Chapter 4

Higher-Q Double-DBR J-Aggregate Microcavity Exciton-Polariton Devices

For most of the last decade of research in organic exciton-polariton devices, the microcavities utilized have included at least one metal mirror (typically silver), which limits the quality factor of the microcavity to about $Q \approx 150 - 200$ [63, 105, 107, 189]. In the few cases in which a higher quality microcavity was fabricated, the organic active layer was either a J aggregate, which provides pumping difficulties as will be described below, or the active material was not a J aggregate, but no comprehensive occupation studies of exciton-polaritons in the lower branch were performed [40, 169]. As shown in recent studies of polariton condensation in inorganic exciton-polariton devices, studying the distribution of exciton-polaritons in the lower branch (by looking at PL emission versus angle) is important in determining the dynamics of polariton relaxation [76].

The issue with low-Q metal or metal-DBR microcavities is that the moderate reflectivity provided by the metal mirror has enough of an extinction coefficient to provide considerable reflectivity (i.e., impedence mismatch between the cavity material and the mirror) but not enough to prevent some penetration of the mode into the mirror and thus loss due to absorption by the metal.

The microcavity Q is important, especially for exciton-polaritons, because loss through photon decay out of the cavity is usually the fastest of the various loss processes. Even for the case of J aggregates, which as described in Chapter 2 have a shorter lifetime due to excitation coherence across multiple molecules, the loss of exctions due to decay processes in the material is usually considerably slower than the loss of photons from the cavity. We can determine the cavity lifetime from the Q in the following way: one can derive the lifetime of a cavity photon by computing the frequency (or energy) spread of the mode at a given resonance frequency (energy). For example, assuming $E_{cav} = 2\,\text{eV}$, a Q of 200 would imply that $\Delta E = 10\,\text{meV}$, which is related to the cavity photon lifetime by:

$$\begin{aligned} \tau_{cav} &= \frac{1}{\Delta\omega} = \frac{\hbar}{\Delta E} \\ &= \frac{\hbar}{10\,\text{meV}} \approx 400\,\text{fs} \end{aligned} \tag{4.1}$$

Therefore, for a microcavity with at least one metal mirror, the lifetime of the cavity photon will usually be at best around one half of a picosecond, and more likely that value will be smaller, around 100 femtoseconds or less. Recalling the discussion of the Boltzmann equations governing polariton relaxation in Chapter 1, if the loss process of polaritons from cavity photon decay is very fast, then polaritons will not be able to thermalize (i.e., lose energy by interacting with phonons) before they decay via cavity loss.

For this reason, in this chapter, the materials engineering and device design involved in creating higher-quality organic microcavity exciton-polariton devices will be addressed. A double-DBR microcavity exciton-polariton device containing a thin film of J aggregates will be demonstrated, and the exciton-polariton occupation distribution of the lower branch will be measured using angle and polarization-resolved photoluminescence (PL).

4.1 Experimental Details

4.1.1 Device Structure and Deposition Procedure

Device Structure and Materials

The structure for the higher-quality-factor J-aggregate microcavity exciton-polariton devices fabricated here is shown in Figure 4-1. The structure is very similar to the structure of devices shown in Chapter 3 except for a few important changes: the top mirror is a sputtered-metal-oxide DBR, the top spacer layer is graded in thickness and doped with the laser dye DCM (4-(dicyanomethylene)-2-methyl-6-(4-dimethylaminostyryl)-4H-pyran), and the J-aggregating cyanine dye has been changed from TDBC (or BIC) to THIATS. The bottom DBRs used were the same commercial DBRs as those used in the devices in Chapter 3. The bottom DBR has 14.5 pairs of TiO_2/SiO_2, and the top DBR has 10 pairs of TiO_2/SiO_2; the DBR layers surrounding the cavity are both TiO_2.

The purpose of the first change, as explained above, is to create higher quality microcavities with longer photon lifetimes. The use of a sputtered mirror allows for precise thickness control since the growth rate of sputtered films is very stable as long as the power supply and gas flow controlling the plasma in the sputterer are also stable. Modern thermal evaporation systems may be able to produce similar thickness precisions, but in this case sputtering was chosen due to machine availability. To enable the deposition of precise thicknesses by the sputterer over many hours of slow film growth, which is crucial in fabricating high reflectivity DBRs on organic materials which are susceptible to sputtering damage and overheating and cannot be annealed at high temperatures, a custom automated sputtering system was built in our lab. The automation system connects all of the necessary components on the sputterer through a custom-built controller to a PC, which has a control program for the sputtering process in LabVIEW. Once the growth rates are calibrated, a program for a DBR, or any series of film thicknesses for that matter, can be entered and run without further user input. This automation system has enabled the fabrication of

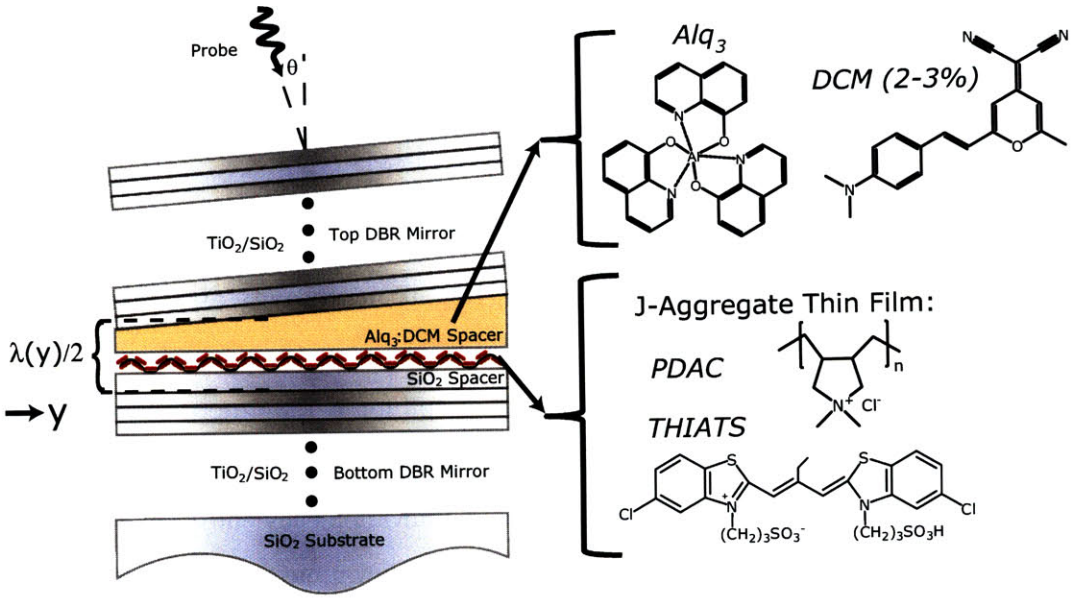

Figure 4-1: Structure of double-DBR structure with graded spacer layer to provide multiple microcavity tunings on a single substrate. The top, graded spacer layer consists of Alq_3 doped $2-3\%$ by weight with the laser dye DCM. The J-aggregate layer is a spin-self-assembled PDAC/THIATS film. The molecular diagrams of the above molecules are shown.

DBRs for this chapter's devices and many other devices in the lab.

The second change described above in the device structure was motivated by needing a way to pump the exciton-polariton system non-resonantly by, for example, using a laser at an energy much higher than the cavity and exciton resonances that are coupled to form the exciton-polariton states. In inorganic quantum-well-based exciton-polariton devices, such non-resonant pumping is trivial thanks to the continuum of absorption at energies above the exciton resonance. Due to the considerable density of states in the conduction and valuence bands of a typical semiconductor, the joint density of states responsible for absorption above the exciton resonance in a quantum well is very large, causing an absorption coefficient even higher than that of the exciton itself. In organic systems, however, especially in the case of J aggregates, this continuum of absorption above the exciton resonance does not exist. Therefore, to mimic the high-energy absorption continuum of a quantum well, energy down-conversion was built into the top cavity spacer of the device shown in Figure 4-1.

Figure 4-2 demonstrates this down-conversion mechanism by plotting the absorption and emission of the materials utilized in the top spacer layer and the absorption of the active material in the exciton-polaritons system, THIATS J aggregates.

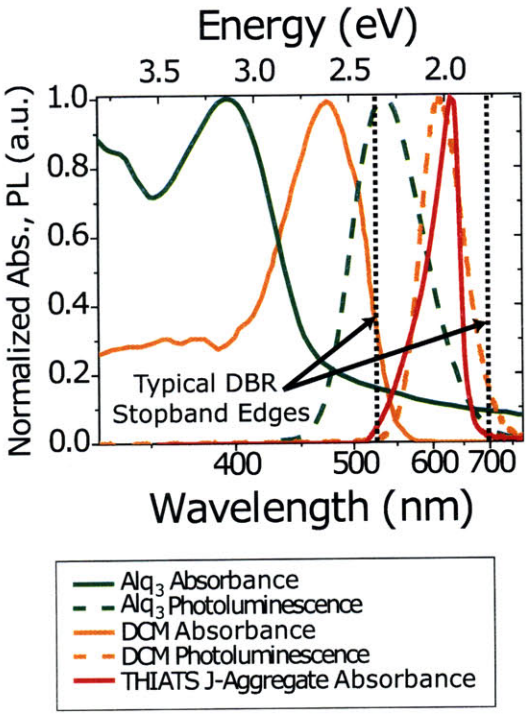

Figure 4-2: Normalized absorbance and PL spectra of Alq_3 and DCM and absorbance spectrum of THIATS J-aggregate thin film [116, 128]. The DCM is doped into the Alq_3 film at $2-3\%$ by weight. Therefore, when the Alq_3 is excited, the excitons are transferred to the DCM dopants by Förster energy transfer. The DCM excitons then either energy transfer to the J-aggregates (if within about $5-10$ nm or radiate into the microcavity. The DCM luminescence inside the cavity is absorbed by the J-aggregate film and also leaks out of the lower DBR sideband.

THIATS[1] is similar in structure to TDBC except for the important difference that THIATS has two sulfur atoms replacing two of the nitrogens that are present in TDBC. THIATS J aggregates additionally have a slight red shift in their resonance frequency from TDBC. Recently, a stability study of a dye similar to THIATS, but with a J-aggregate resonance in the near-infrared (NIR), was performed in comparison

[1](Benzothiazolium, 5-chloro-2-[2-[[5-chloro-3-(3-sulfopropyl)-2(3H)-benzothiazolylidene]methyl]-1-buten-1-yl]-3-(3-sulfopropyl)-, inner salt, compounded with N,N-diethylethanamine (1:1)] obtained from H.W. Sands, CAS 23568-98-1.

to TDBC [197]. The authors found that the THIATS-like dye was considerably more stable. In our experiences with THIATS, we have seen a similarly robust performance in comparison to TDBC. Since the two dye structures (that of THIATS and the NIR dye) are very similar, especially in that they are both thiacyanines (i.e., the same end structures with the two sulfurs), it is likely that the same photobleaching chemistry applies to both dyes as well, accounting for the stability increase of THIATS with respect to TDBC. This increased photostability may be due to a reduced susceptibility to singlet oxygen, which has been known to significantly degrade cyanines in writeable CDs [68]. Tertiary amines (i.e., nitrogens with three bonds to carbon atoms) are particularly susceptible to singlet oxygen reactions, which may explain why cyanines in general are susceptible to singlet oxygen and why this susceptibility is reduced in thiacyanines, where two of the tertiary amines have been replaced by sulfur atoms [81, 163].

Deposition of Graded Top Spacer Layer

In the devices demonstrated in Chapter 3, a single detuning of the cavity and exciton was fabricated for each of the demonstrated devices. To enable the investigation of multiple detunings on the same substrate and therefore reduce changes from variation in the J-aggregate films, the devices in this chapter are fabricated with a graded top spacer layer. A graded-thickness film is grown in thermal evaporation by using a fixed shadow mask with a rotating substrate holder. The fixed shadow mask is designed such that at different radii on the substrate, a different amount of the rotation path is blocked by the fixed shadow mask.

A schematic and photograph of the fixed shadow mask used in fabricating the graded top spacer layer in the microcavities here is shown in Figure 4-3.

With the design shown in Figure 4-3, the fraction of film thickness grown (given by thickness with the mask divided by thickness grown if unmasked) is:

$$t_{frac} = 1 - \frac{2}{\pi} \arcsin\left(\frac{d}{2R}\right) \tag{4.2}$$

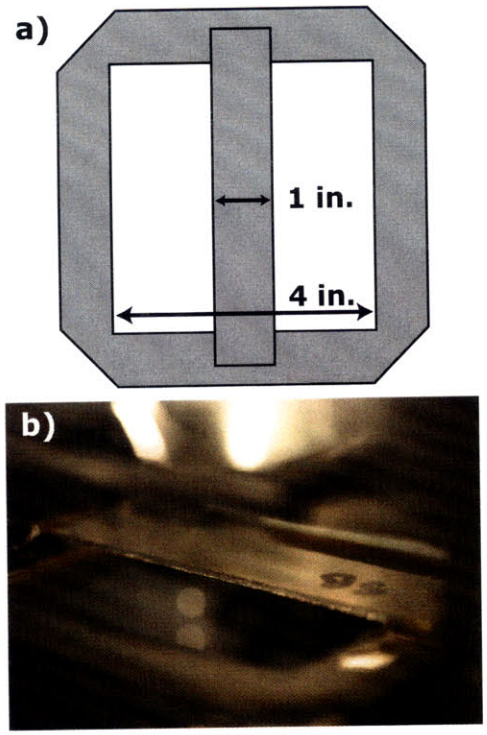

Figure 4-3: (a) Fixed mask design for growing thickness gradient. (b) Photograph of mask on thermal evaporator transfer arm inside LOOE growth lab high-vacuum transfer line. The mask is left on the transfer arm and placed in front of a rotating substrate holder, masking off a part of the growth path.

where d is the width of the fixed mask shown in Figure 4-3(a), and R is the radius from the center of the substrate's circle of rotation (assumed to be coincident with the center of the fixed mask). Figure 4-4(a) shows a 3D plot of the fraction of film grown (i.e., the fraction of what would be grown without the fixed shadow mask) on a 1 inch square substrate placed with its bottom edge $\frac{1}{2}$ inch from the center of the substrate holder. Figure 4-4(b) shows a top-down view of the predicted thickness fraction, and Figure 4-4(c) shows a photograph of a silicon substrate grown in the same deposition as that in which the top cavity spacer was grown on the DBR samples; the interference pattern caused by the thickness variation matches the predicted thicknesses, and very good agreement between the predicted and measured thicknesses on the witness sample was found through ellipsometry at $\lambda = 633$ nm.

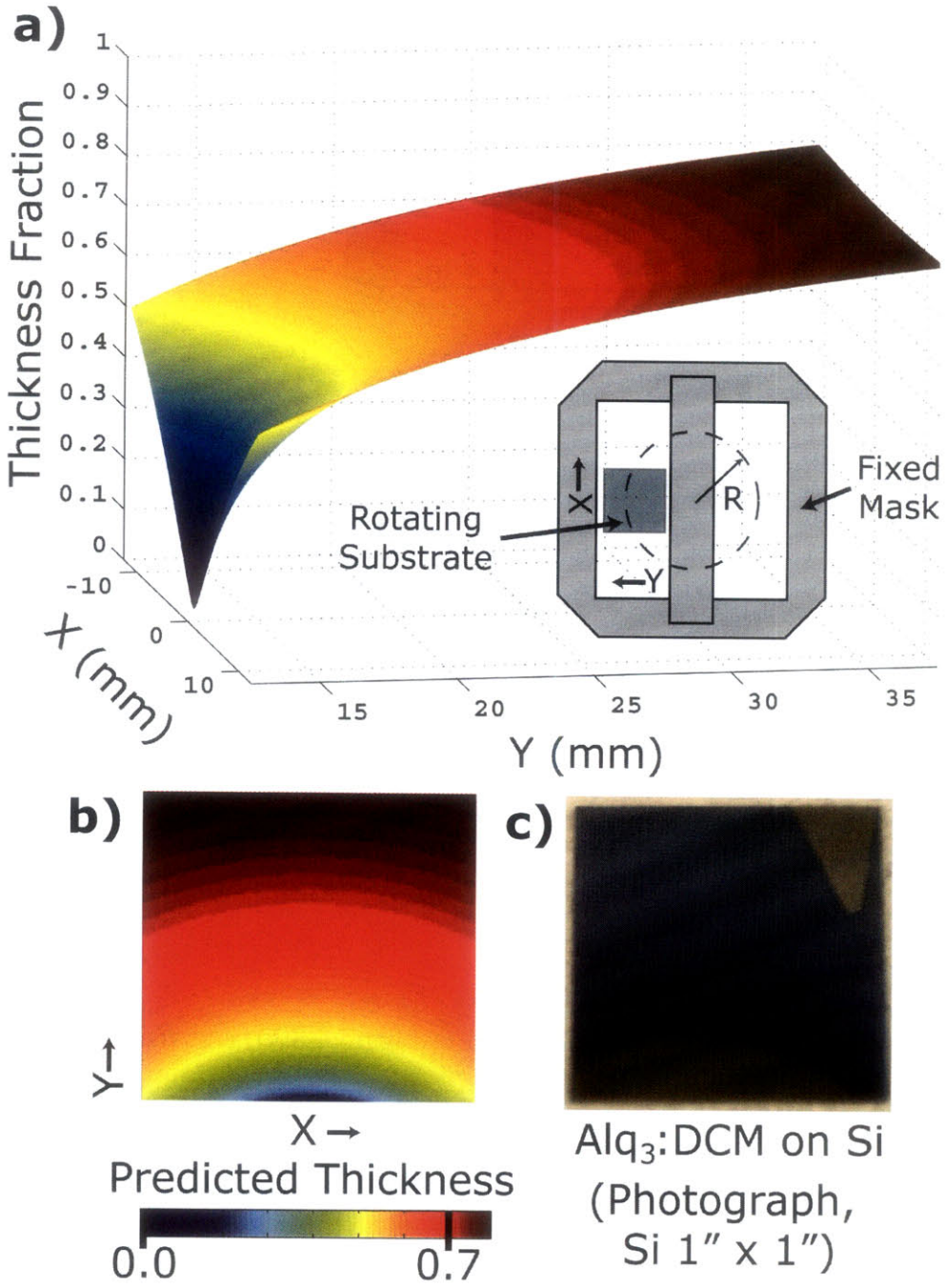

Figure 4-4: (a) Calculated thickness fraction of film grown with fixed mask on a one-inch square substrate. Inset shows one-inch square substrate and rotation path compared to mask design. (b) Top-down view of film thickness fraction predicted for a one-inch square substrate, with color bar showing the corresponding fraction. (c) Photograph of one-inch square piece of silicon onto which was thermally evaporated through the fixed mask in Figure 4-3 a thin film of Alq_3 doped with $2-3\%$ DCM.

Spin Self-Assembly of J-Aggregate Thin Film

In previous chapters, the J-aggregate thin films were grown by layer-by-layer (LBL) deposition in which the substrates were immersed into the growth solutions for a period of time, usually 5 to 15 minutes for each growth step. While this method was shown to produced uniform films with nanoscale thickness control and minimal scattering (shown by the good agreement of the measured and predicted transmittance from the Kramers-Krönig-derived index of refraction), there are some drawbacks to general use of the LBL method in a laboratory setting. For starters, to grow multilayer films, an automated dip-coating system is a necessity due to the several hours required for a deposition (since LBL is diffusion limited in the growth solution), meaning that the process is very inefficient if performed manually. Secondly, due to the immersion of not only the substrates but also the substrate holder into the growth solutions, after even a single deposition cycle (SICAS), the growth solutions are cross-contaminated. Once a recipe has been determined, this is not too much of a concern, but in determining recipes this cross-contamination leads to considerable uncertainty in engineering of the LBL thin film. And finally, in most dip coaters, the growth solution containers are non-Teflon plastic (limiting etch-cleaning options) and therefore a risk of cross-contamination when changing from one dye to another since the dyes tend to adsorb to the rougher plastic surface and resist cleaning more than for a typical Pyrex beaker.

To address these shortcomings, in this study, a spin self-assembly (SSA) process was developed for PDAC/THIATS J-aggregate thin films. SSA of polyelectrolyte thin films was first introduced in the early 2000s and has been utilized to make both thin films comprised of all polyelectrolytes and thin films of polyelectrolytes and oppositely charged particles (quantum dot, molecule, etc.) [28, 32, 33, 74, 101, 102, 127, 143]. Figure 4-5 shows a schematic of the SSA process. The process is very similar to the LBL process in theory of operation; oppositely charged layers are sequentially adsorbed with the excess loosely-bound material rinsed, allowing for nanoscale thickness precision.

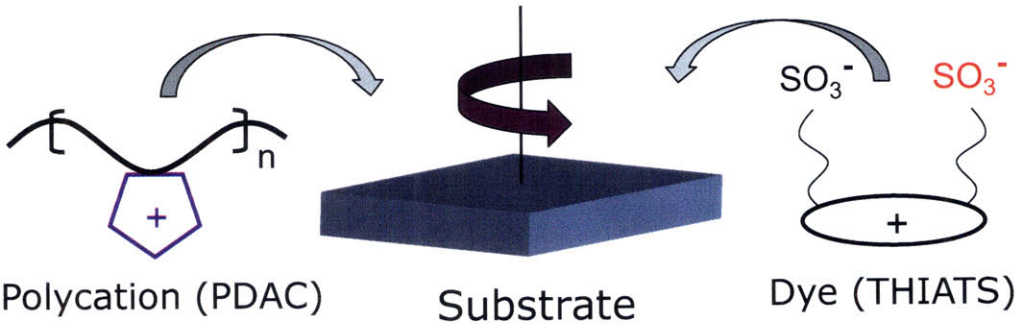

Figure 4-5: Schematic of spin self-assembly (SSA) process. Solutions of the polycation (PDAC) and anionic, J-aggregating dye THIATS are alternately spun-cast onto the substrate. After each spin step, the substrate is rinsed twice with deionized water while slowly spinning amd then accelerated to a higher angular velocity to dry.

The SSA process is performed on a typical spin coater. Prior to deposition, the glass or silicon substrates were cleaned using sonication in (individually) Micro-90 detergent, water, and then acetone followed by immersion in boiling isopropanol. The cleaning process was finished with a six minute oxygen plasma cleaning in a Plasma Preen oxygen plasma system. For each growth step (i.e., anionic or cationic solution "immersion"), the growth solution is placed onto the substrate, and the substrate is immediately accelerated at 1000 RPM/s (used for all steps below) to an angular velocity of 3000 RPM, which is maintained for 15 s. The substrate is then decelerated to 500 RPM for 10 s and doused with deionized water (at least 5 mL for each quarter square inch of substrate). Sufficient rinse amounts are important for consistency in deposition in order to adequately remove excess material, and a low pressure of rinse water should be used to prevent uneven removal of material (e.g., pouring from a beaker instead of squirting from a large syringe was found to provide best film quality). A slow rate of spinning was used for the rinse as opposed to a full stop to prevent water from flowing into the motor of the spinner. The substrate was then accelerated again to 3000 RPM for 15 s, decelerated to 500 RPM for 10 s to be rinsed again, and finally accelerated to 3000 RPM for 30 s for a final drying step.

A full SICAS is comprised of the above procedure performed for each growth solution (i.e., twice for a typical single anion/single cation film). One potential benefit

of SSA is that integration with deposition of spun-cast non-ionic materials (such as poly(vinyl alcohol), or PVA) or materials in other solvents is straightforward.

For SSA of J-aggregate thin films, it was found that dyes with greater water solubility are most compatible with SSA (as opposed to needing instead the immersion part of the LBL process) since the greater solubility in water seems to correspond to a greater degree of dissociation of the dye molecules. Therefore, a solution of THIATS self-assembles in an SSA film better than a TDBC solution of the same concentration due to the greater water solubility of THIATS. Similarly, adding $0.01 - 0.1$ M salt (sodium chloride) to the THIATS solution inhibits SSA film formation by screening the charge on the THIATS (which in turn allows the THIATS to J-aggregate in solution and eventually crash out if the salt concentration is raised all the way up to 0.1 M or higher). The PDAC growth solution is a 3 mM solution of high-molecular-weight PDAC (poly(diallyldimethylammonium chloride), $M_w = 4-5\times10^5$), obtained from Sigma Aldrich. The THIATS growth solution was 100 μM in concentration, made from diluting a 2 $\frac{\text{mg}}{\text{mL}}$ stock solution of THIATS in DI water.

Figure 4-6 shows the reflectance and transmittance of three SSA PDAC/THIATS films on glass with different numbers of SICAS; the SICAS unit is still used since for simple two-component films, the number of growth cycles in both LBL and SSA entail the same number of cation/anion processing steps.

The thickness of a 6.5 SICAS SSA PDAC/THIATS film deposited onto a known thickness of SiO_2 on a silicon substrate with a known index of refraction was determined using a Gaertner ellipsometer at $\lambda = 830$ nm. The thickness was found to be 6.6 ± 0.3 nm. From this number and the trends shown in previous studies of SSA film growth, we estimate that each SICAS corresponds to $\Delta d = 1.1$ nm [32, 33]. Based on this estimate, the films shown in Figure 4-6 are assumed to have thicknesses $d = (4.4, 6.6, 8.8)$ nm for 4.5, 6.5, 8.5 SICAS, respectively. With an estimate of the film thicknesses, we can then determine the complex index of refraction for each of the films as demonstrated in Chapter 2. The results of the quasi-Kramers-Krönig regressions for the three films measured in Figure 4-6 are shown in Figure 4-7.

A slight red shift as more layers are deposited is observed in the derived n, κ, and

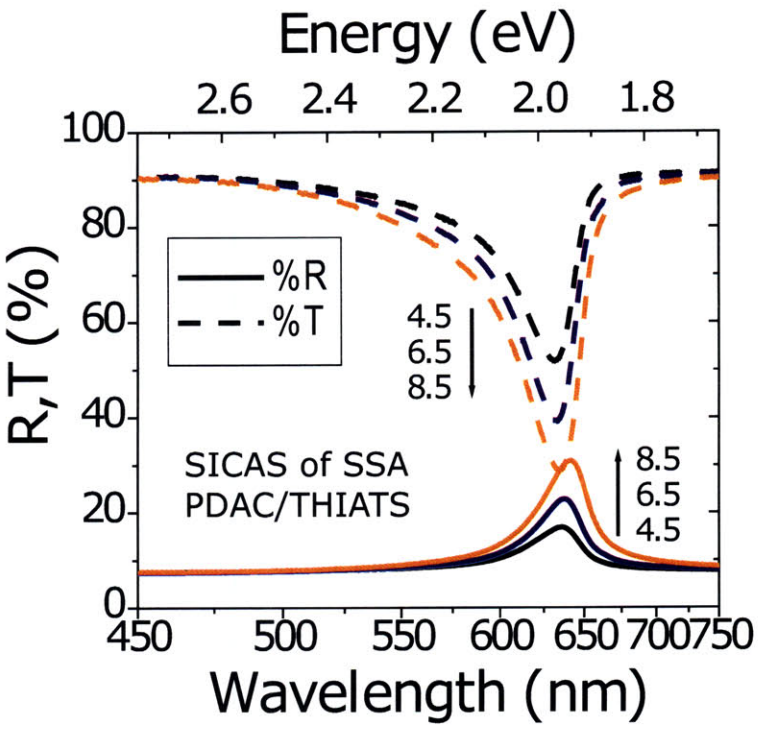

Figure 4-6: Reflectance and transmittance measurements of 4.5, 6.5, and 8.5 SICAS PDAC/THIATS SSA thin films on glass.

a slight increase in the dye density is also indicated by the slight increase in peak κ. The greater dye density in the 8.5 SICAS film likely causes a greater degree of aggregation, which is consistent with a red-shift in the peak; additionally, a greater dye density may also lead to a red-shift in the peak due to solid-state solvation [117].

Figure 4-8 shows the absorbance of the PDAC/THIATS films calculated from the derived extinction coefficient (plotted in Figure 4-7) along with the PL spectra collected at normal incidence from the same films. The films were excited with a CW 20 mW, $\lambda = 532$ nm diode-pumped solid-state laser focused into a 100 μm diameter spot. The emission was collected by a multimode fiber bundle with 19 fibers, each with a diameter (core+cladding) of 245 μm. A 150 grooves/mm grating was used in a SpectraPro 300i spectrometer with CCD and slit width set at 25 μm, to give roughly 0.5 nm resolution in the spectrum.

As is typical for a J-aggregate, the PL spectra show very little Stokes' shift from the absorption. This amount of Stokes' shift is an important figure of merit for exciton-

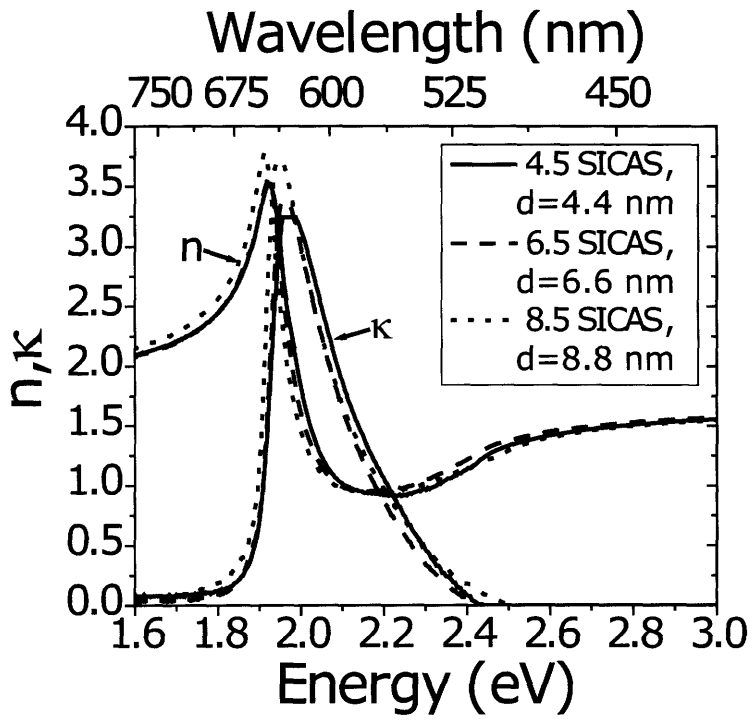

Figure 4-7: Complex index of refraction for 4.5, 6.5, and 8.5 SICAS PDAC/THIATS SSA thin films derived via quasi-Kramers-Krönig regression performed on reflectance measurements shown in Figure 4-6. The indicated thicknesses are based on ellipsometry measurements performed at $\lambda = 830$ nm for a 6.5 SICAS film on an Si/SiO_2 substrate, which indicated a thickness of $d = 6.6$ nm, leading to the estimate of 1.1 nm per SICAS deposited.

polariton devices since a Stokes' shift of the excitation away from the strongly-coupled resonance can serve as an efficient decay mechanism.

In the process of fabricating a microcavity exciton-polariton device, a (nearly) critically-coupled resonator (CCR) is formed near the resonance of the J aggregate. The degree of critical coupling depends on the bottom spacer of the cavity and the linewidth and thickness of the absorbing film. When the impedences of the various layers are set correctly, full critical coupling can be achieved, meaning that the reflectance at the critically-coupled resonance at normal incidence will be zero, and all normally-incident light at that resonant energy will be absorbed by the absorbing layer (assuming that the mirror is not lossy) [186]. Figure 4-9(a) shows a photograph of three DBRs in the process of fabricating the device structure shown in Figure 4-1.

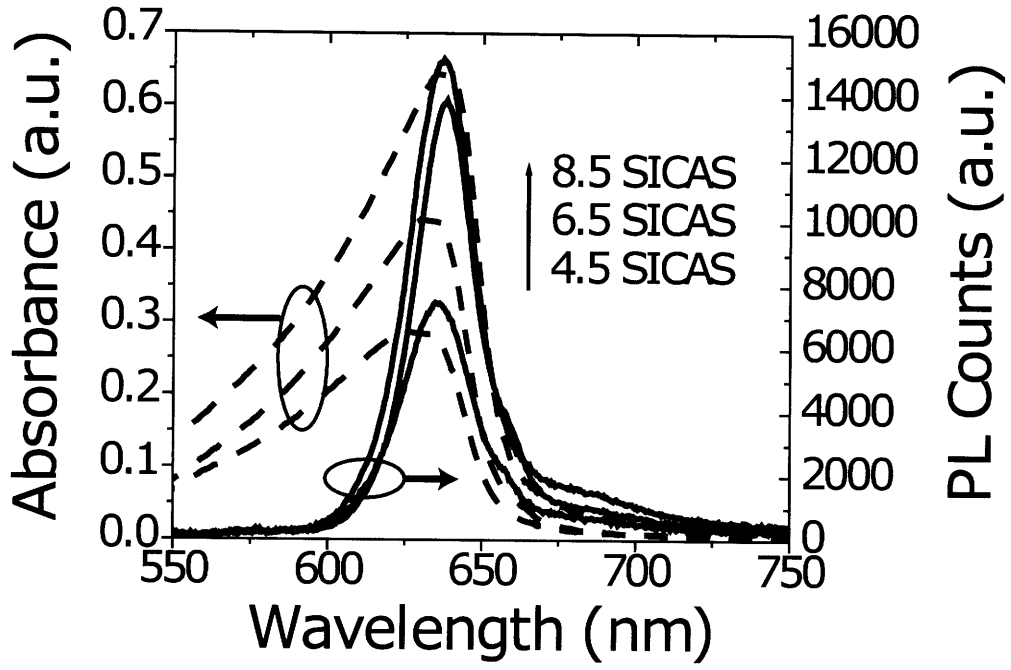

Figure 4-8: Absorbance and PL for various thicknesses of PDAC/THIATS SSA J-aggregate thin films. The absorbance shown is calculated from the derived κ from Figure 4-7 and assumed film thickness d ($Abs. = \frac{4\pi\kappa}{\lambda}d$). For the PL, the films were excited with a $\lambda = 532$ nm laser at an angle with the PL collected at normal.

The DBRs have been coated with a sputtered SiO_2 layer with thickness $d_{SiO_2} = 128.4 \pm 0.3$ nm to form the bottom cavity spacer. PDAC/THIATS SSA films of 6.5 SICAS each were then deposited individually onto each substrate, forming a nearly critically-coupled resonator on each, as shown in the reflectance spectra in Figure 4-9(b). Significantly, the reflectance spectra from all three samples overlap in the absorption region of the PDAC/THIATS film (around $\lambda = 600 - 630$ nm), indicating the consistency of the SSA film deposition process. The structures are not truly CCRs due to the slight overgrowth of the bottom cavity spacer layer (located directly underneath the J-aggregate film), which prevents perfect impedence matching.

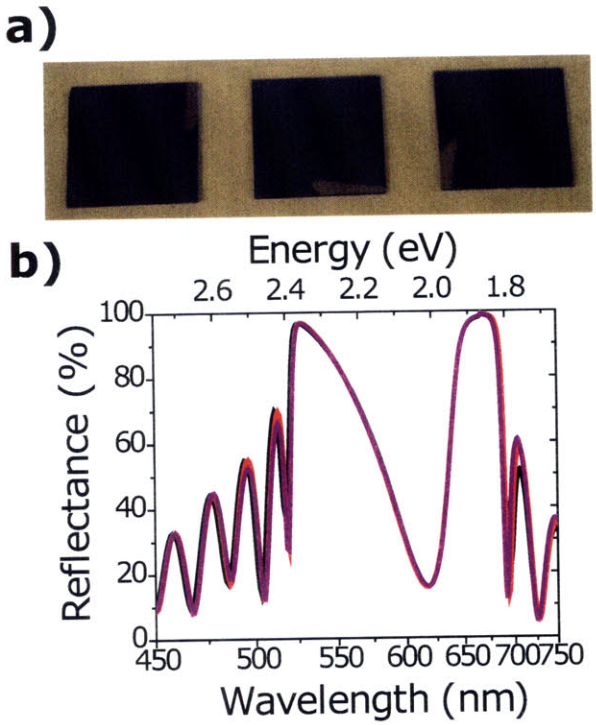

Figure 4-9: (a) Photograph of samples after 6.5 SICAS PDAC/THIATS SSA step in deposition of structure shown in Figure 4-1. (b) Measured reflectance of samples shown in (a). At this step, with a J-aggregate thin film on top of a spacer and DBR, the samples are (nearly) critically-coupled resonators [186]. The overlapping reflectance curves show the consistency of the SSA process across multiple samples.

4.1.2 Photoluminescence Measurement Setup

Due to the ability of the excitonic part of the exciton-polariton to interact with the environment (e.g., phonon scattering) and other excitons or exciton-polaritons, it is possible for exciton-polaritons to scatter between different systems on the continuum of exciton-polariton modes in the dispersion–this is precisely the motivation for trying to relax all of the exciton-polaritons into the lowest energy on the lower branch. For this reason, the occupation of exciton-polaritons in the various states along the continuum of modes is of paramount importance, and the most effective way to probe this occupation is to examine the PL from exciton-polariton devices versus angle.

As described in Chapter 1, the planar microcavity exciton-polariton system is actually a continuum of strongly-coupled light-matter systems due to the continuum

of microcavity modes that are coupled to the dipoles in the material. The planar microcavity has a minimum-energy mode corresponding to normal incidence at the mirror surface, and as an angle is swept out from normal, the energy of the microcavity resonance rises until either the mirror stopband is reached (such as in the case of DBRs), or until at large angle the microcavity dispersion approaches the linear dispersion relation of the material inside the cavity (which is the limiting case of the TEM mode propagating down the waveguide). Therefore, if the microcavity resonance is matched to the exciton resonance at normal incidence, then at larger angles the exciton-polariton system at each angle is positively detuned to a greater and greater degree (i.e., the cavity energy is higher than the exciton energy).

In this chapter, the PL of exciton-polariton devices was probed using the setup shown in Figure 4-10. A fiber attached to a rotational stage collected the PL from the sample, which was mounted on a separate set of micrometers, which were used to vary the position of the laser excitation spot on the sample. The Alq_3 in the top spacer layer of the microcavity was excited by a 4 mW, $\lambda = 408$ nm CW laser. The laser was focused into a roughly 100 μm-diameter spot, and the emission was collected through a long-pass filter with cut-off wavelength $\lambda_{cut-off} = 450$ nm in order to filter out the laser line. The angle of collection was swept out at 0.5° increments with the use of an automated system described below.

Figure 4-11 shows photographs of the PL setup, showing the sample holder and long-pass filter and fiber alignment. Between the front of the filter and sample is an open post holder that is used to hold a linear polarizer when the individual TE/TM-polarized emission is measured.

As mentioned earlier, an automated system was used to sweep out angles at 0.5° increments. This automation allowed for precise measurements of large ranges of angles without the need for any user interaction, helping to keep the alignment of the optics and therefore input power constant for each angle measurement. Figure 4-12 shows a the geometry of the angle-translation setup. Through simple geometry, a relation can be made between the length of wire reeled in by the motor and the angle swept out by the arm connected to the rotational stage. An elastic is used to

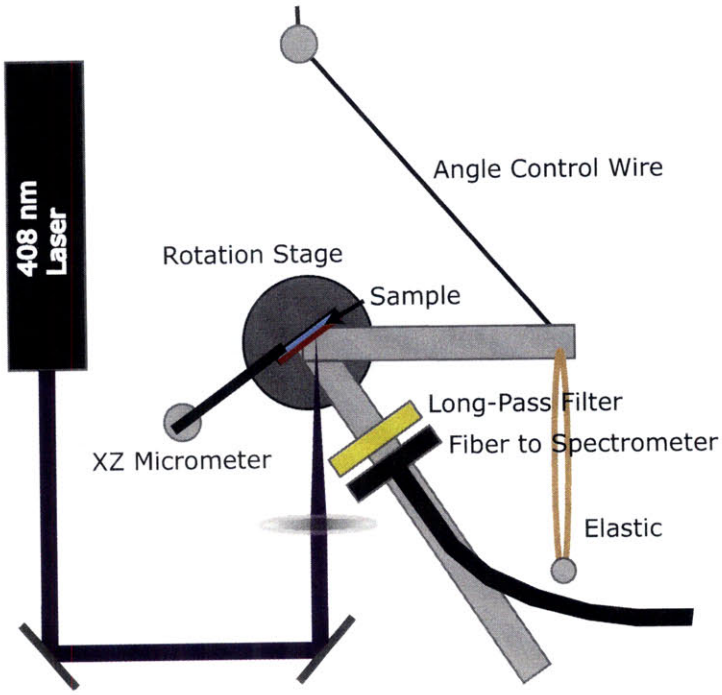

Figure 4-10: Schematic of angle-resolved photoluminescence measurement setup. The sample is mounted on a 2D micrometer stage (XZ, where X is parallel to the sample and Z is normal to the page) above the center of a rotation stage. The rotation stage has two radially-directed rods attached. On one rod is mounted a long-pass filter to block reflected laser excitation and a multimode fiber connected to a spectrometer. The other rod has an elastic band connected to the table and a wire guided through a fixed point and then connected to a motorized spool. When the wire is wound a known amount, the angle of the fiber is changed a known amount relative to the sample surface. The laser excitation is initially at a higher height than the target spot on the sample and is guided at about a $10 - 15°$ decline by the mirrors to the sample, passing through a focusing lens. The decline in the beam path allows for all angles to be measured without coupling the excitation into the fiber.

pull against the motor, thereby holding the arm's angle steady. The elastic does not, however, provide enough torque to the arm to overcome the resistance of the halted motor and unreel the wire. Precise lengths can be reeled by the DC motor since the motor shaft has been geared down four times at a ratio of 5:1 for a total of 625:1. This gearing also helps greatly to resist unreeling of the wire.

The length h can be related to the angle of the post from $\theta = 0°$. We know that the projection of the R post parallel to the D length is $R \sin\theta$. A right triangle

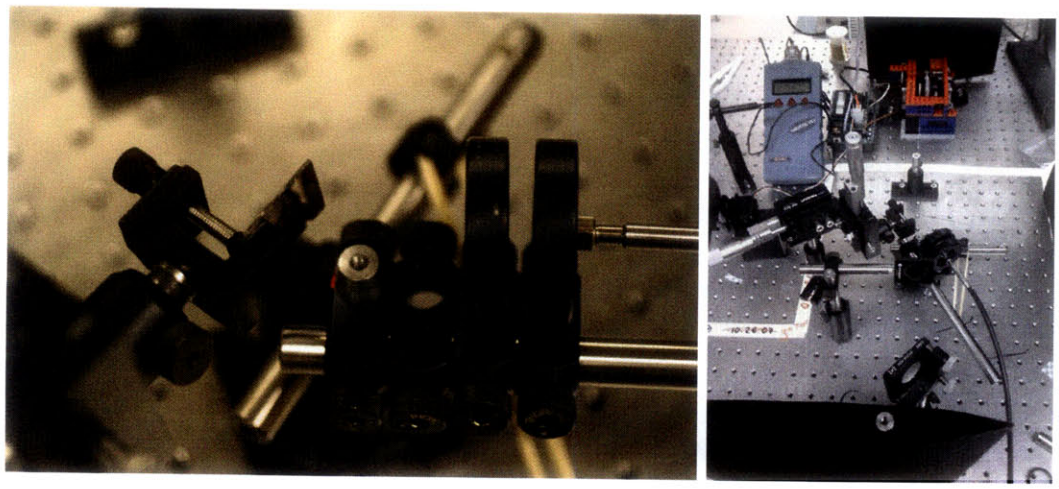

Figure 4-11: Photograph of sample holder, long-pass filter, and optical fiber shown in schematic in Figure 4-10.

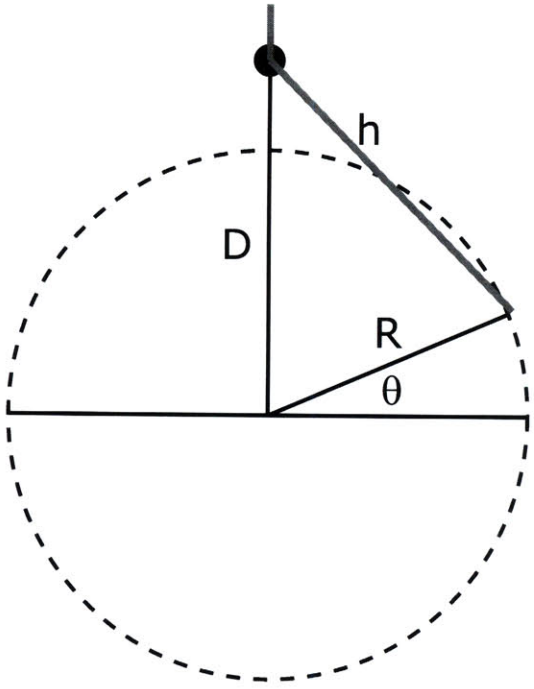

Figure 4-12: Schematic of geometry of angular collection control based on spooling a known length of wire corresponding to setup shown in Figure 4-10. h is the length of the wire between the fixed post and rotating post. R is the length of the rotating post. D is the distance between the axis of rotation and fixed post.

made by drawing a straight line to the D length from the end of the R post has sides of length $R\cos\theta$ and $D - R\sin\theta$ and h. We can therefore solve for h using the

Pythagorean theorem and relate h directly to θ:

$$\begin{aligned} h &= \sqrt{R^2\cos^2\theta + (D - R\sin\theta)^2} \\ &= \sqrt{R^2(\cos^2\theta + \sin^2\theta) + D^2 - 2DR\sin\theta} \\ &= \sqrt{R^2 + D^2 - 2DR\sin\theta} \end{aligned} \tag{4.3}$$

We can therefore calculate the change in h that happens in moving from one angle to another, which gives the amount of wire that needs to be spooled or unspooled when moving the rotation stage.

4.2 Measured Photoluminescence Dispersion: Angle and Position

The measured normal-incidence PL from points across the sample is plotted in Figure 4-13 along with fits to determine the cavity resonance at each point, assuming a J-aggregate resonance of $\lambda_{J-Agg} = 630$ nm and $\hbar\Omega_R = 80$ meV. These parameters were initially chosen due to their fit to the angle-resolved PL shown below. The numbers are explained further by mathematically bleaching in T-matrix simulations the complex index of refraction derived by Kramers-Krönig regression and shown in Figure 4-7 above. This bleaching fit is described further below.

The Y values given correspond to an alignment of the sample as shown in Figure 4-4. The X value for all the Y positions was roughly $X = 0$, meaning the middle of the sample.

The displayed fits are to the two-level exciton-polariton model discussed in Chapter 1. The eigenenergies of the lower and upper exciton-polariton modes, E_- and E_+, respectively, are given by:

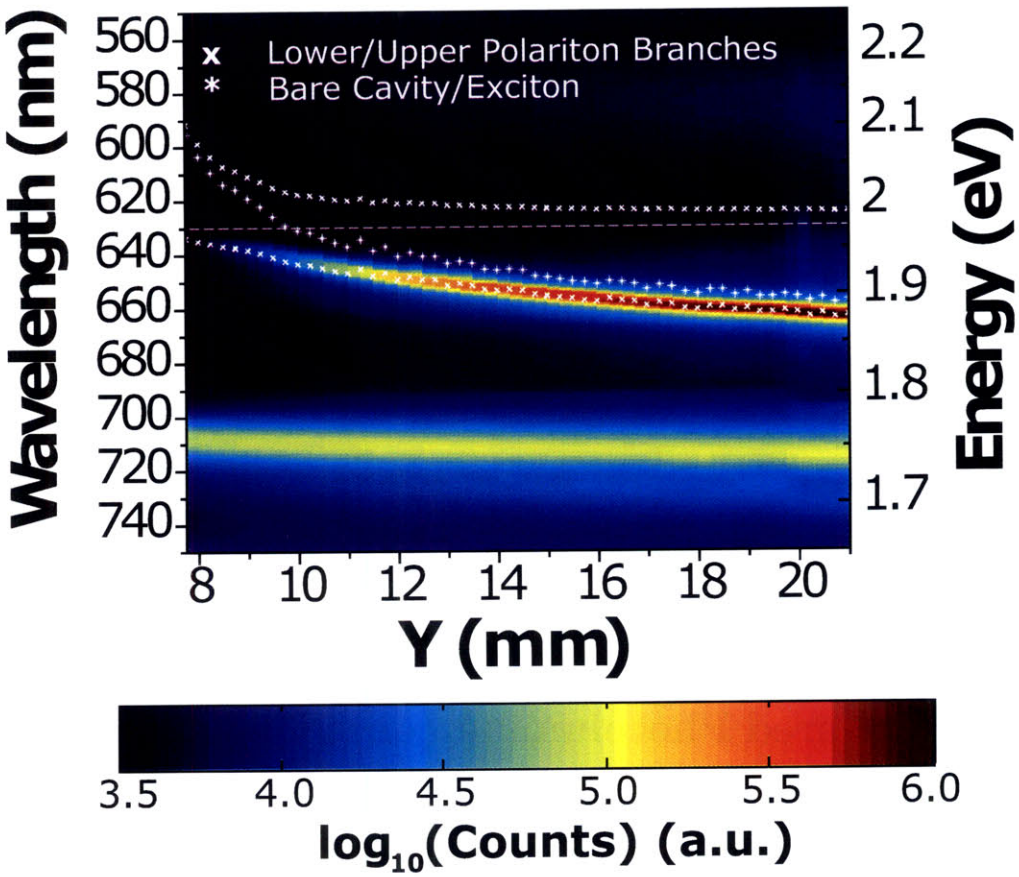

Figure 4-13: Photoluminescence at normal incidence measured across sample. For each position, the cavity resonance was determined by fitting the lower-branch exciton-polariton energy predicted by the two-level exciton-polariton model with $\Omega_R = 80$ meV and $\lambda_{J-Agg} = 630$ nm to the measured spectra. The exciton-polariton eigenenergies ('**x**') and bare exciton and cavity resonances ('$*$') are shown.

$$E_{\pm} = \frac{1}{2}(E_{cav} + E_{J-Agg}) \pm \frac{1}{2}\sqrt{\hbar\Omega_R^2 + (E_{cav} - E_{J-Agg})^2} \tag{4.4}$$

where the cavity energy as a function of angle is given by:

$$E_{cav}(\theta) = \frac{E_{cav}(0°)}{\sqrt{1 - \frac{\sin^2\theta}{n_{eff}^2}}} \tag{4.5}$$

The cavity resonance energy at each point on the sample is found by fitting Eq. 4.4

with the measured lower-branch exciton-polariton eigenenergy and the other parameters as stated above. The cavity resonance wavelengths found through this fitting method do not clearly fit the trend in top spacer thicknesses predicted and confirmed for the silicon test substrate in Figure 4-4. This is likely due in part to the need to balance the effects of the bottom spacer thickness on the cavity resonance energy with the effects of the varying top spacer layer thickness. Additionally, damage to the top spacer layer from sputtering the top mirror likely distorted the thickness profile predicted and measured in Figure 4-4 for a sample that had not undergone sputtering.

Detailed angle and polarization-resolved PL spectra were measured for two positions (referred to subsequently as Positions A and B) on the sample, both with negative detuning of the cavity at normal incidence with respect to the J-aggregate exciton resonance. Both sets of data have been corrected to indicate emission per solid angle inside the cavity by dividing the observed counts by the cosine of the external angle; this accounts for the change in solid angle going from inside to outside the cavity due to Snell's Law (see Lambert's Cosine Law or Stokker-Cheregi *et al.* [173]). The PL spectra of Position A, which has a smaller negative detuning, is shown in Figure 4-14, with plots (a), (b), and (c) corresponding to unpolarized, TE-polarized, and TM-polarized, respectively. The fit to Eq. 4.4 is shown, using $\lambda_{cav} = 644.5$ nm and $n_{eff} = 1.8$. With $\lambda_{J-Agg} = 630$ nm, this corresponds to a detuning of $\Delta E = -44$ meV. This was the smallest negative detuning probed due to the sharp drop-off in luminescence (shown in Figure 4-13) as the cavity resonance approaches that of the exciton at zero detuning.

In order to examine how the relative detuning affects relative exciton-polariton occupation in the lower branch, a second position with larger negative detuning was also probed. Figure 4-15 shows the angle and polarization-resolved PL spectra for the second spot. The fit to Eq. 4.4 is shown, using $\lambda_{cav} = 657$ nm and $n_{eff} = 1.85$. This value for the cavity resonance corresponds to a detuning of $\Delta E = -81$ meV.

The parameters used to fit Eq. 4.4 to the data in Figures 4-13, 4-14, and 4-15 are found to match those required to fit the angle-resolved absorption spectra predicted by T-matrix simulations when the quasi-Kramers-Krönig-derived complex

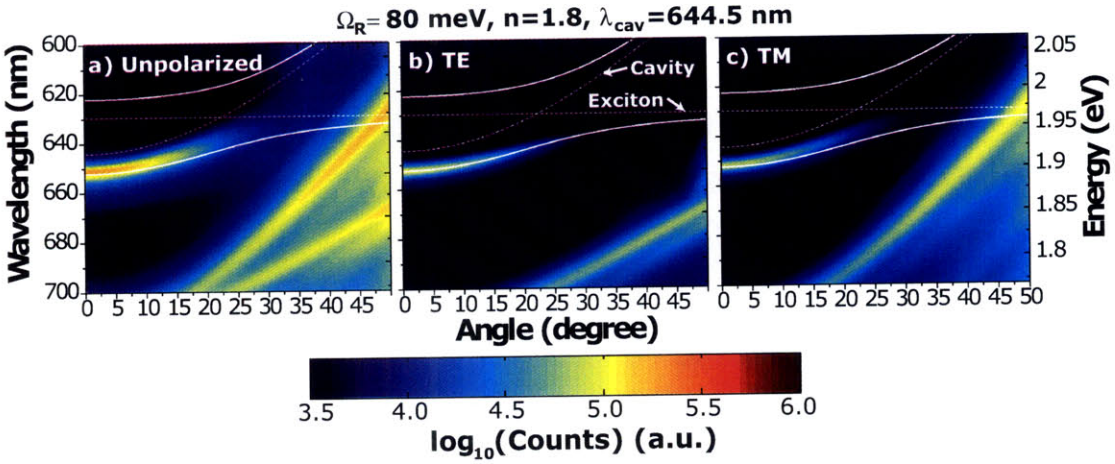

Figure 4-14: Photoluminescence from lower-branch exciton-polariton from position with smaller negative detuning (Position A). The values of the two-level model fitting parameters (Ω_R, λ_{cav}, and n, the effective cavity index) are shown. Plots (a, b, and c) show unpolarized, TE-polarized, and TM-polarized emission, respectively, along with the two-level model fit to the lower-branch exciton-polariton. Angular data were collected every 0.5°. The counts were divided by $\cos(\theta_{ext})$ to account for the change in external solid angle measured caused by Snell's law.

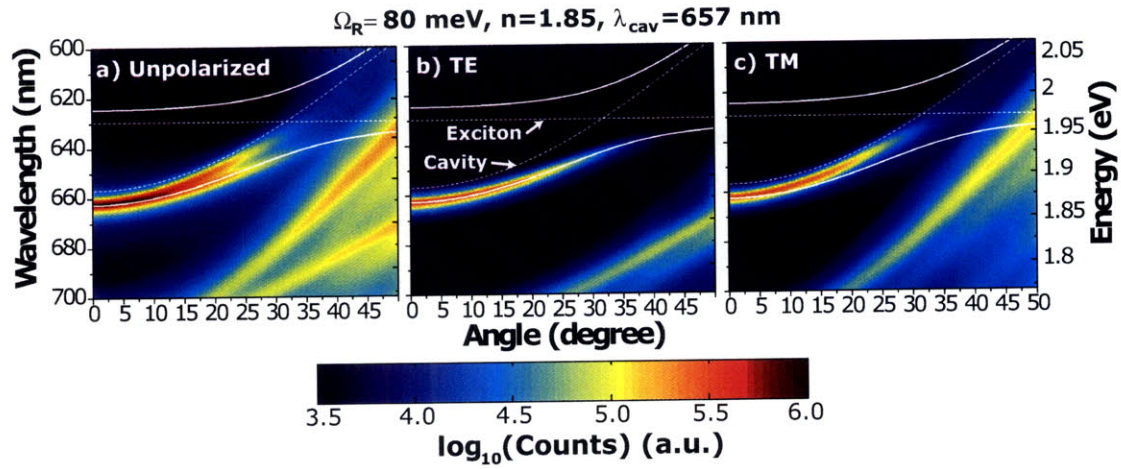

Figure 4-15: Photoluminescence from lower-branch exciton-polariton from position with larger negative detuning (Position B). The values of the two-level model fitting parameters (Ω_R, λ_{cav}, and n, the effective cavity index) are shown. Plots (a, b, and c) show unpolarized, TE-polarized, and TM-polarized emission, respectively, along with the two-level model fit to the lower-branch exciton-polariton. Angular data were collected every 0.5°. The counts were divided by $\cos(\theta_{ext})$ to account for the change in external solid angle measured caused by Snell's law.

index of refraction for the 6.5 SICAS film in Figure 4-7 is bleached by 50% and blue-shifted by $\Delta\lambda = 3$ nm. The bleaching is due to either direct damage from heating or impact during sputtering, or more likely the constant illumination of the devices undergoing the sputtering of the top mirror by emission from the plasma. The emission from the plasma excites the Alq_3:DCM film, which subsequently emits at the J-aggregate's resonance, causing the J-aggregate thin film to continually undergo turnovers for the several hours of sputtering. In addition to bleaching the resonance, a slight blue-shift of the resonance occurs, which is accounted for phenomenologically; likely causes of the blue-shift in the J-aggregate resonance include a slightly different local environment of the dipoles and a reduced number of coupled molecules in each aggregate, recalling that the coupling between molecules is responsible for the red-shift of the J-aggregate resonance from the molecule's resonance.

The bleaching is carried out mathematically by first calculating $\chi(\omega) = (n + i\kappa)^2 - 1$. The variation of the real part of χ around $n_{offset}^2 - 1$ and magnitude of the imaginary part of χ are then reduced by 50% (using $n_{offset} = 1.7$, the value used in the Kramers-Krönig regression originally). This bleached χ is then converted back to n and κ, which are blue-shifted $\Delta\lambda = 3$ nm by simply shifting the n, κ vectors. Since the shift is smaller or of comparable magnitude to the feature linewidths in the index of refraction, shifting by wavelength instead of energy does not cause much change to the linewidths. Figure 4-16 shows the bleached and blue-shifted index of refraction used in the T-matrix simulations of the device.

Using the modified n, κ shown in Figure 4-16, we can simulate the absorption spectrum of the full device structure with T-matrices, as was discussed in Chapter 3. Carrying out such a simulation with the same published values for the indices of Alq_3 and TiO_2 used in Chapter 3, the absorption spectra are calculated for unpolarized (i.e., half TE and half TM) and TE light; these are shown in Figure 4-17 with a fit to Eq. 4.4. The spectra were calculated for 0.1° increments in angle and 0.1 nm increments in wavelength, with values for the various indices of refraction for the materials in the structure linearly interpolated between the nanometer-resolved data points.

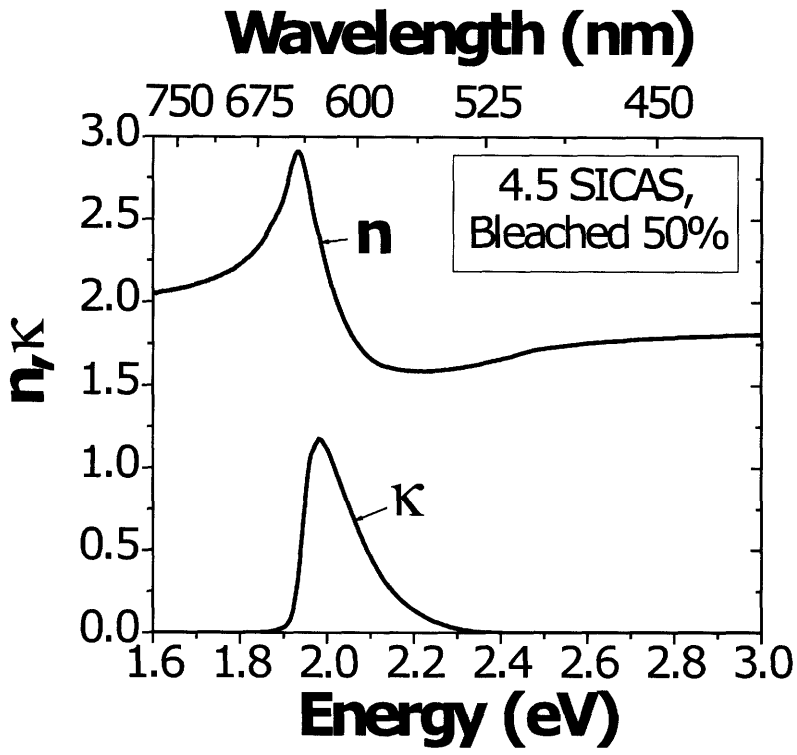

Figure 4-16: Predicted complex index of refraction of 4.5 SICAS film, shown in Figure 4-7, bleached by 50% and blue-shifted by $\Delta\lambda = 3$ nm, which accounts for a slight shift in the J-aggregate peak due to bleaching some of the monomers in each aggregate. The calculation is performed by first calculating $\chi(\omega) = (n + i\kappa)^2 - 1$, then reducing the variation of the real part around $n^2_{offset} - 1$ and magnitude of the imaginary part by 50% (using $n_{offset} = 1.7$, the value used in the Kramers-Krönig regression originally).

With a top spacer layer thickness of $d_{top} = 105$ nm, the resulting spectra fit the two-level model with parameters $\hbar\Omega_R = 80$ meV, $\lambda_{J-Agg} = 630$ nm, $\lambda_{cav} = 645$ nm, and $n_{eff} = 1.85$, nearly identical to those parameters for Position A above. This indicates that the slightly higher n_{eff} for the cavity than the $n_{eff} = 1.7$ used in Chapter 3 is a product of the linear optical properties of the device, likely caused by the lower branch being closer to the edge of the DBR stopband, where the phase of the DBR reflectivity is no longer just $\pm\pi$. The linear optical modeling here indicates that the value of the Rabi splitting observed, $\hbar\Omega_R = 80$ meV, is due to a bleaching of the J-aggregate thin film by 50%. Additionally, the angle and polarization-resolved dispersion observed was shown to match that predicted by the T-matrix models. Con-

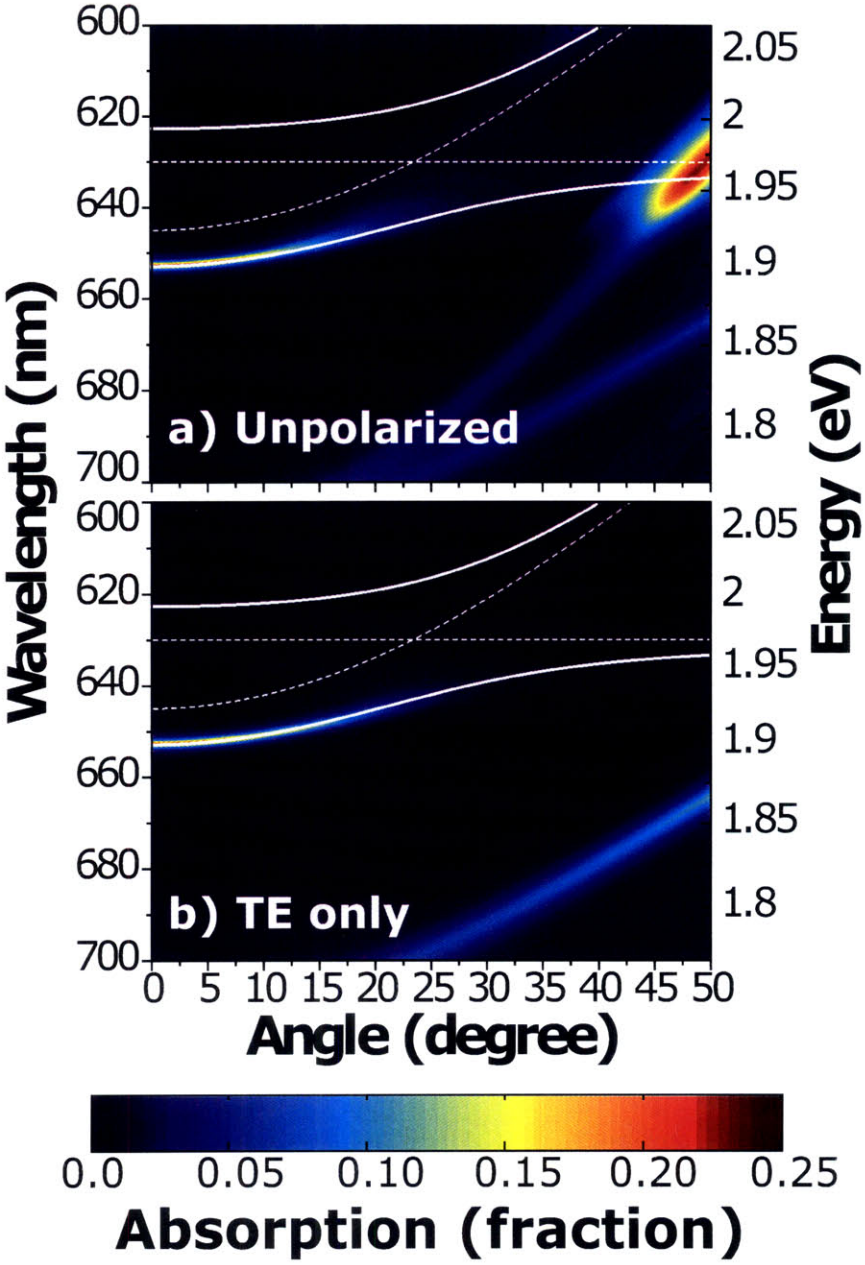

Figure 4-17: Absorption fraction for TE and unpolarized ($\frac{1}{2}(A_{TE} + A_{TM})$) light using T-matrix model of structure with bleached complex index of refraction shown in Figure 4-16. The two-level model fit uses $\hbar\Omega_R = 80$ meV, $\lambda_{J-Agg} = 630$ nm, $\lambda_{cav} = 645$ nm, and $n_{eff} = 1.85$.

firming that the measured PL indeed match that expected for a THIATS J-aggregate exciton-polariton system, we can now analyze the magnitude of PL measured in the spectra of Figure 4-14 and 4-15.

4.3 Analysis of Photoluminescence Data

The first step in converting the measured exciton-polariton PL to relative exciton-polariton occupation numbers, after correcting for the $\cos\theta_{ext}$ in the measurement itself, is to determine the photon fraction at each angle for each detuning. The photon fraction in the lower branch is found by determining the Hopfield coefficients for the exciton-polariton lower branch. The Hopfield coefficients, $X_{\mathbf{k}}$ and $C_{\mathbf{k}}$, are connected to the fraction of exciton and photon for each exciton-polariton state in the dispersion. The coefficients obey the formula [79]:

$$|X_{\mathbf{k}}|^2 + |C_{\mathbf{k}}|^2 = 1 \tag{4.6}$$

The Hopfield coefficients are calculated from the Rabi splitting, detuning between exciton and cavity photon at a given angle (i.e., $\mathbf{k}$), and the energies of the upper and lower exciton-polaritons and bare states [79]:

$$|C_{\mathbf{k}}|^2 = \frac{E_U(\mathbf{k})E_X(\mathbf{k}) - E_L(\mathbf{k})E_C(\mathbf{k})}{(E_C(\mathbf{k}) + E_X(\mathbf{k}))\sqrt{(E_C(\mathbf{k}) - E_X(\mathbf{k}))^2 + \hbar^2\Omega_R^2}} \tag{4.7}$$

$$|X_{\mathbf{k}}|^2 = \frac{E_U(\mathbf{k})E_C(\mathbf{k}) - E_L(\mathbf{k})E_X(\mathbf{k})}{(E_C(\mathbf{k}) + E_X(\mathbf{k}))\sqrt{(E_C(\mathbf{k}) - E_X(\mathbf{k}))^2 + \hbar^2\Omega_R^2}} \tag{4.8}$$

In the lower polariton branch, $|C_{\mathbf{k}}|^2$ gives the photon fraction, and $|X_{\mathbf{k}}|^2$ gives the exciton fraction. In the upper branch, the coefficients are reversed. The fits to Eq. 4.4 for Positions A and B give the upper and lower polariton dispersions, E_U and E_L, respectively, as well as the bare cavity and exciton energies versus angle, E_C and E_X, respectively. The Rabi splitting is also determined in the fitting procedure done to produce the fits in Figures 4-14 and 4-15. The in-plane momentum, as described in Chapter 1, is related to the external angle by $k_{\|} = k_0 \sin\theta_{ext}$. Figure 4-18 shows the photon fraction calculated for Positions A and B using Eq. 4.7.

Also plotted in Figure 4-18 is the energy versus angle of the emission peak of the TE-polarized lower-branch PL emission plotted in Figures 4-14(b) and 4-15(b)

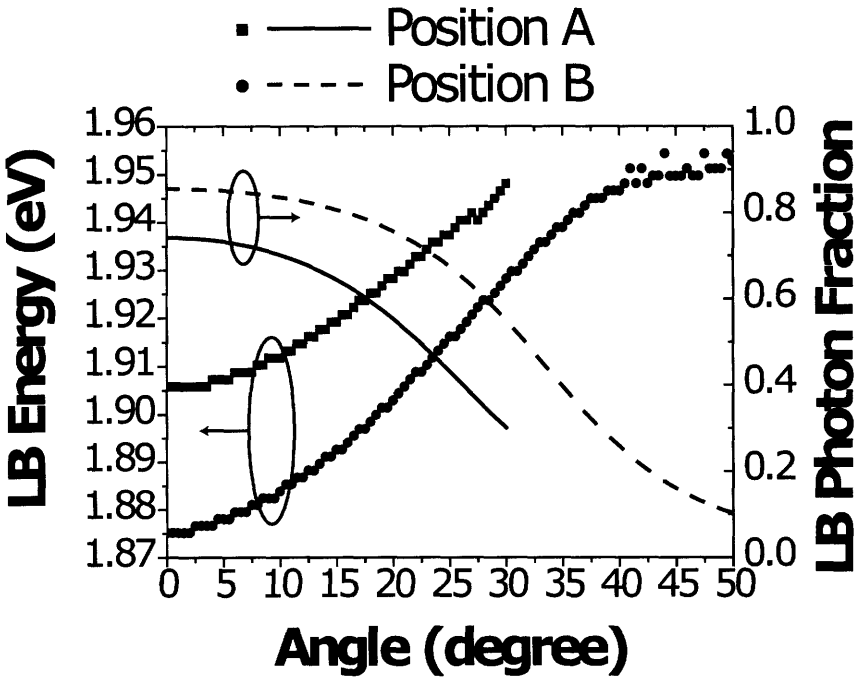

Figure 4-18: Photon fraction and energy of lower-branch exciton-polariton for measured angle-resolved PL spectra from Position A and B, shown in Figures 4-14 and 4-15, respectively. To determine the polariton occupation from measured PL, the counts measured (already scaled by $\cos(\theta_{ext})$) must be divided by the photon fraction to account for increased PL decay from states with a larger photon component. The photon fraction in the lower branch is given by the square of the magnitude of the Hopfield coefficient, $|C_{\mathbf{k}}|^2$.

for Positions A and B, respectively. Particle distributions are usually graphed on a set of axes that relates the logarithm of the occupation to the energy such that the slope of the distribution can be compared to a known distribution function such as Maxwell-Boltzmann. For the sake of accuracy, we use the exact energy of the maximum, but this just ends up being the same as the two-level model dispersion fit for the TE-polarized PL.

With the data in Figure 4-18, the measured PL of the TE-polarized lower-branch exciton-polariton can be scaled by dividing by the photon fraction and plotted versus energy; the division by the photon fraction accounts for the increased likelihood of polariton decay due to cavity photon emission, which is what we are measuring, when

the polariton has a larger photon fraction. Figure 4-19 plots the occupation ("scaled counts") distribution of lower-branch exciton-polaritons at the two positions along with a Maxwell-Boltzmann distribution at $T = 300$ K as a reference.

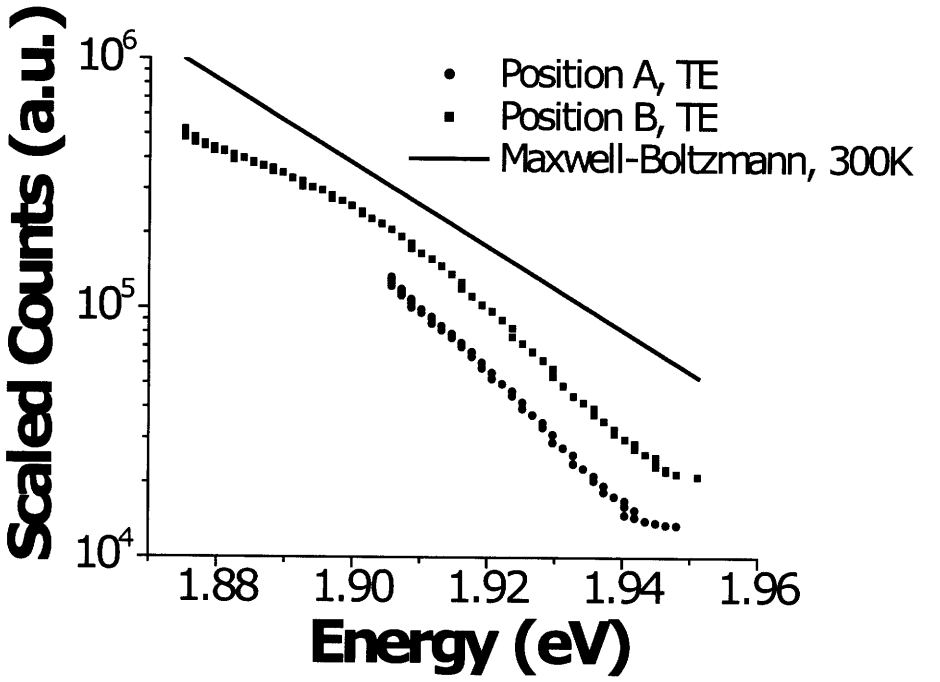

Figure 4-19: Relative occupation of lower-branch exciton-polariton versus energy given by scaling the TE-polarized PL by the photon fraction shown in Figure 4-18. A Maxwell-Boltzmann distribution at $T = 300$ K is shown by the solid line as a comparison. The distribution is somewhat non-thermal, likely due to different amounts of direct pumping of the lower-branch photonic component by the DCM molecules radiating within the cavity.

Figure 4-19 indicates that the distribution of exciton-polaritons in both Position A and B does not exactly match the thermal distribution given by the Maxwell-Boltzmann function. This near-thermal distribution is likely the result of using mostly intracavity resonant radiative pumping via the DCM molecules to populate the lower-branch exciton-polariton. Although some of the exciton-polaritons in the PL spectra were likely formed by scattering from the uncoupled THIATS excitons that had absorbed the DCM pump, the overlap of the DCM spectra with the lower-branch exciton-polariton also allows for the DCM to directly emit photons into the

exciton-polariton states without first scattering from the J-aggregate exciton reservoir's uncoupled states. Future devices could still utilize the non-resonant pump scheme demonstrated here but with a thin film of J-aggregates dispersed in a thicker polymer matrix instead of in a thin LBL/SSA film. The polymer matrix could also have the non-resonant pump dye dispersed in it, which would allow for population of J-aggregate excitons quickly via Förster resonant energy transfer (FRET) instead of by spontaneous emission of the pump dye within the cavity. Additionally, the J aggregates in these devices could be pumped directly through the upper branch in the $\lambda = 550 - 600$ nm part of the visible spectrum.

In this chapter, double-DBR J-aggregate microcavity exciton-polariton devices have been demonstrated that incorporate sputtered-metal-oxide top DBRs to produce higher quality factor microcavities than the all-metal or metal-DBR microcavities typically used in organic exciton-polariton devices. Additionally, a top cavity spacer was demonstrated which mimics the continuum of high-energy absorption present in inorganic quantum well systems and allows for strong pumping of J-aggregate exciton-polaritons. Finally, due to choice of a more robust J-aggregate and the ability to strongly pump the exciton-polariton system, detailed angle and polarization-resolved PL spectra were collected in order to investigate the relative occupation of exciton-polariton states in the dispersion for the first time, revealing a near-thermal distribution with deviations which were likely in part caused by the population of lower-branch exciton-polaritons by both scattering from the exciton reservoir and direct intracavity radiative pumping by DCM molecules.

4.4 Pumping at Higher Powers

An additional set of experiments performed on the samples fabricated in this chapter involved pumping the devices with a range of input intensities to observe the input-output characteristics of these J-aggregate microcavity exciton-polaritons pumped via intracavity DCM emission. Figure 4-20 shows a plot of the logarithm of measured PL for a spot on the sample versus wavelength and input energy density. The pump

is a laser with $\lambda = 408$ nm center wavelength, pulse length of 150 fs, and a repetition rate of 1 kHz. The spot size is an unfocused circle $1 - 2$ mm in diameter.

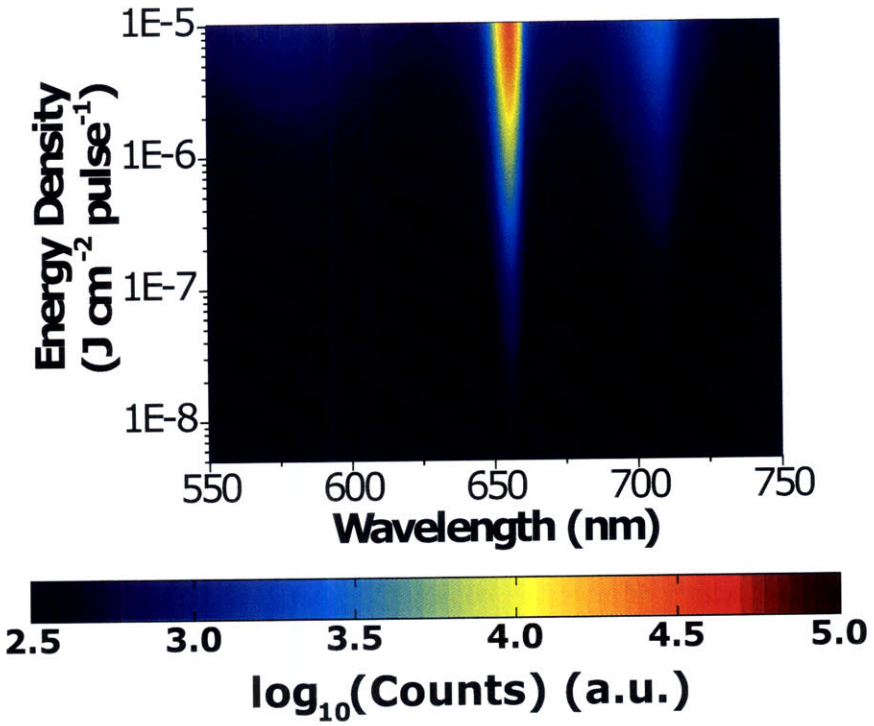

Figure 4-20: Lower-branch exciton-polariton PL from a single spot versus energy density of pump. The pump has a $\lambda = 408$ nm center wavelength with a pulse length of 150 fs and a repetition rate of 1 kHz. The spot size is a circle $1 - 2$ mm in diameter. The lower-branch exciton-polariton for the measured spot is at $\lambda_- = 656$ nm. Background emission from the DCM escaping out of the cavity can be seen both in the DBR stopband and at the edges of the DBR stopband, with strong attenuation corresponding to the J-aggregate absorption.

The lower-branch exciton-polariton is at $\lambda_- = 656$ nm. Notably, the lower-branch does not shift at all during the measurements, indicating that the THIATS J-aggregates do not photobleach during the pumping any more than the bleaching which already occurred during the device fabrication. Additionally, a faint outline of the DCM emission spectra can be observed at high powers, likely due to some of the DCM molecules being able to emit faintly outside the exciton-polariton lower-branch. The DCM background emission, however, is strongly attenuated at the energies of the J-aggregate absorption. Finally, owing to the fairly wide bandwidth of DCM emission,

the lower-energy sideband of the DBR mirrors can be used to probe the input-output emission characteristics of just the DCM molecules radiating in non-strongly-coupled modes.

Figure 4-21 plots observed counts from the lower-branch exciton-polariton peak and DBR-sideband peak in Figure 4-20 versus input energy density. The filled-in points show measurements as the input energy was increased from minimum to maximum energy, and the empty points show the measured counts as the input energy density was decreased from maximum energy back to the minimum input energy density. The two sets of points overlap, indicating that no significant photobleaching of any of the device constituents occurred.

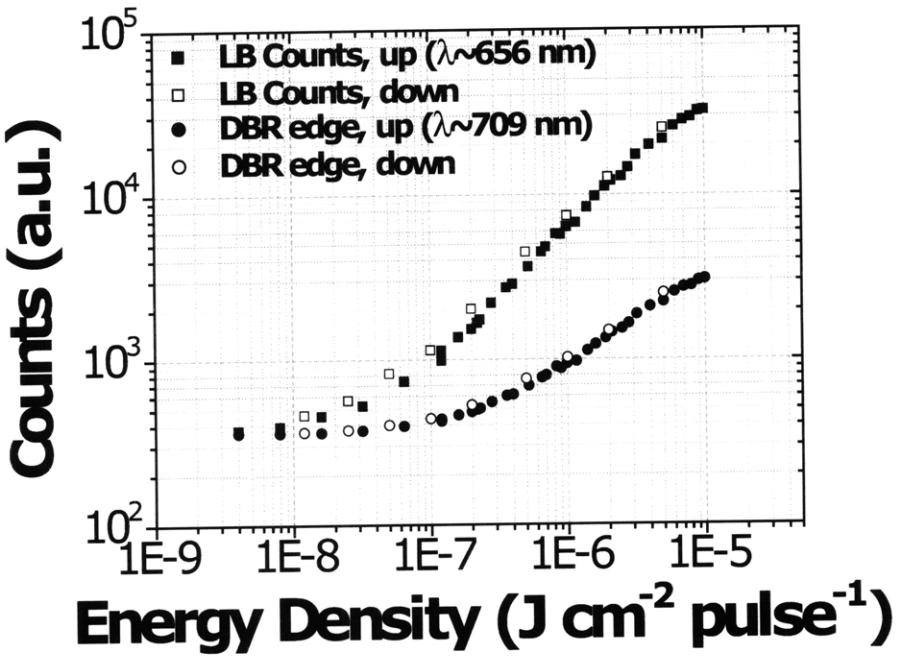

Figure 4-21: Measured PL counts from same spot as in Figure 4-20. The peak counts of the lower-branch exciton-polariton ($\lambda = 656$ nm) emission and DBR edge emission ($\lambda = 709$ nm) are plotted. Both plots show a distinct change in slope at an input energy density of about 0.1 $\frac{\mu J}{cm^2 pulse}$, likely due to amplified spontaneous emission in the DCM, which also causes an eventual roll-off in the emission at higher energy densities.

A pronounced knee in the input-output characteristics of both the DBR-sideband

and lower-branch exciton-polariton peak are visible at an input energy density of about 0.1 $\frac{\mu J}{cm^2 pulse}$. At high input energy densities, the measured counts of both roll-off as well. These observations, since they occur in both the strongly-coupled state's emission and the uncoupled DBR-sideband emission of the DCM, are consistent with amplified spontaneous emission (ASE) in the Alq_3:DCM top cavity spacer layer [149]. Since the top spacer layer does not provide sufficient gain to overcome the various losses in the cavity (absorption by the strongly-coupled J-ggregate exciton-polaritons and mirror losses), the DCM does not reach a lasing threshold, but instead the ASE serves to at first increase the intensity of DCM emission into the vertical cavity modes and then cause a roll-off in the emission as energy is dumped into waveguided modes at higher input energy densities. This serves as a rather stark reminder of the already-high performance of organic laser dyes as discussed in Chapter 1, but it also raises an intriguing theoretical question. Generally, exciton-polariton lasing is thought to occur due to final-state stimulation of an exciton-polariton state from an exciton reservoir at higher energy, with the polariton relaxation occurring via phonons or polariton-polariton scattering. But is "final-state" stimulation via the strongly-coupled cavity photon also an option if the gain of DCM or some other laser dye is used to pump the strongly-coupled lower-branch exciton-polariton? Such a topic may be a source for future theoretical and experimental studies of exciton-polaritons in organic systems.

Chapter 5

Laterally-Patterned Organic Microcavity Devices

Recent research efforts in microcavity exciton-polariton devices based on inorganic active materials such as GaAs or CdTe quantum wells has focused on the lateral patterning of microcavity exciton-polariton systems [55]. Such 0D cavities allow for symmetry-breaking of the in-plane wave vector, opening new pathways for parametric generation of photon pairs [9]. For the same reason, laterally-patterned organic microcavity exciton-polariton devices are also of interest. In addition, recently, low-threshold lasing was demonstrated from pillars formed by thermally evaporating thin films of Alq_3 (aluminum tris(8-hydroxyquinoline)) doped with the laser dye DCM (4-(dicyanomethylene)-2-methyl-6-(4-dimethylaminostyryl)-4H-pyran) through thin nickel shadow masks with square, 5×5 μm^2 openings [98–100, 175]. In this chapter, a different approach to laterally patterning organic microcavities, applicable either to traditional lasers or exciton-polariton devices, is demonstrated. PDMS lift-off patterning of the organic microcavity spacer layer is used to laterally define the microcavity resonance energy. The PDMS lift-off patterning method was demonstrated by our lab as a way to pattern organic layers or electrodes for OLED fabrication [200, 201]. A thin film of thermally-evaporated TPD (N-bis(3-methylphenyl)-N,N -diphenyl-1,1-biphenyl-4,4-diamine) doped with DCM is patterned using PDMS lift-off patterning, forming embossed pillars of varying diameter down to 5 μm in the TPD

film with a thickness of 20-25 nm; a shift in the microcavity resonance of about 30 nm is observed, consistent with the shift expected for a $\lambda/2n$ metal-DBR microcavity.

While the shadow-mask approach is attractive for its apparent simplicity, the authors in the studies cited above are pushing the lower-resolution limits of shadow-masking as lateral pattern sizes approach 1 μm due to simple mechanical constraints in scaling the shadow masks themselves. These mechanical constraints are a significant hurdle in OLED manufacturing, as scaling up the lateral dimensions of a mask require a scaling of the thickness of the mask as well. Since the OLED pixel dimension does not scale in this process, an increase in the thickness of the mask would lead to less uniformity in the patterned organic layer due to shadowing by the mask sidewalls. The same issue occurs when scaling down the lateral feature size without scaling the other dimensions of the mask, since maintaining a uniform evaporated feature thickness at a small lateral dimension requires eventually making the shadow mask thinner, which is not mechanically feasible. PDMS lift-off patterning offers a path around this scaling issue since it is a subtractive patterning technique, meaning that a thin film can be deposited through blanket evaporation without any shadow mask. Additionally, smaller features than are achievable through shadow masking are theoretically feasible even with PDMS due to the generally low aspect ratio in PDMS needed for embossing small features on the patterned organic film since the features in the PDMS are a negative image of the desired pattern (i.e., micron-sized holes instead of pillars).

5.1 Experimental Details–Demonstration Device Structure and Fabrication

Figure 5-1(a) shows the structure of the patterned demonstration microcavity devices fabricated in this chapter. Part (b) of the same figure shows a schematic of the PDMS lift-off patterning process, where a TPD film is lifted off by a patterned PDMS stamp, leaving behind islands of TPD that serve to vary the microcavity resonance energy

in those positions. Finally, part (c) of the figure shows the molecular diagrams of the constituent materials.

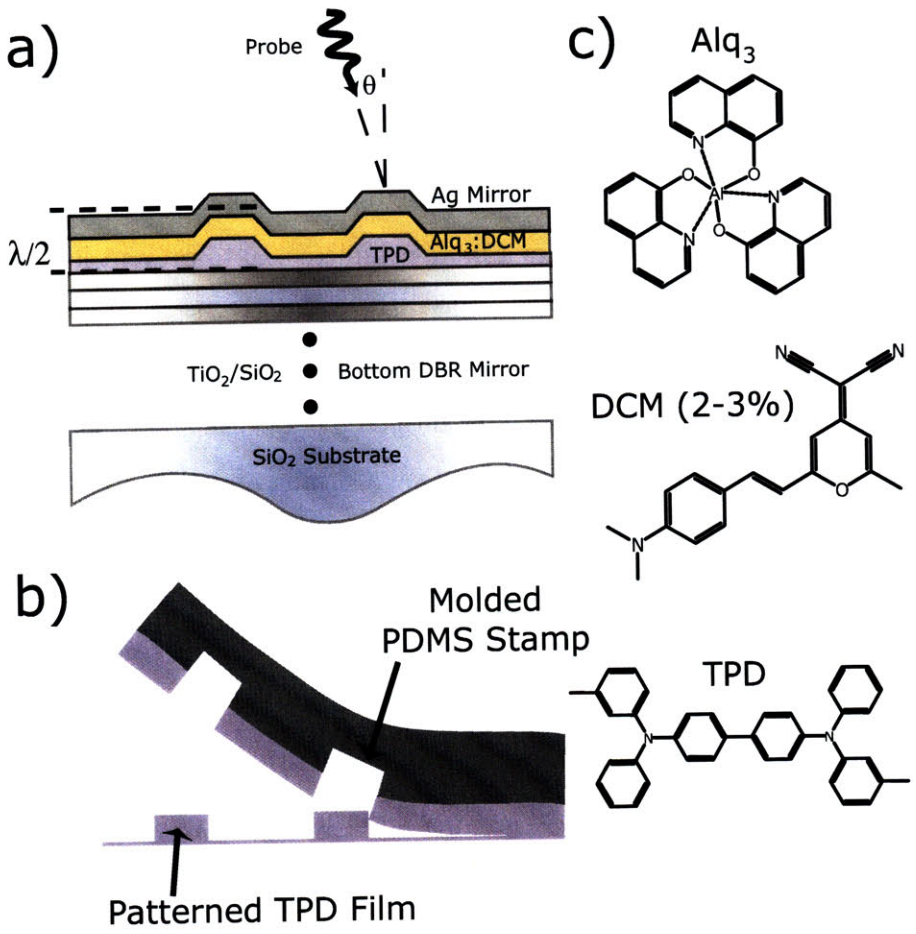

Figure 5-1: (a) Patterned microcavity structure. (b) PDMS lift-off patterning process. (c) Molecular structures of constituent materials.

The substrate is a commercially-obtained DBR, the same as those used in the devices in Chapters 3 and 4. The deposited TPD film is doped with DCM $2-3\%$ by weight so that DCM is present throughout the microcavity, which would be required for future laser fabrication applications. After the TPD deposition, the samples are brought out of the high-vacuum evaporator and into a laminar flow hood for the stamping step. The laminar flow hood environment was used to prevent dust from building up on the sample. While the stamping in this case was performed outside of the inert nitrogen gloveboxes in our lab's growth facilities, this step can be performed

in the gloveboxes to prevent oxygen exposure in the organic layers.

Figure 5-2 shows a photograph of the apparatus used for making PDMS stamps from a patterned silicon master that is a full wafer. The silicon master wafer is placed at the bottom of a plastic petri dish, and a ring made from a sheet of transparency film is placed around the edge of the wafer. The top of the apparatus is then placed on the transparency film, which provides a more complete seal to prevent leaking of the uncured PDMS. The top portion is a smaller-diameter petri dish with a hole melted out of the bottom to allow for pouring of the uncured PDMS onto the wafer, and the screws act as weights to hold the seal between the top petri dish and transparency and wafer. The PDMS is Sylgard 184 made by Dow Corning and mixed in a 10:1 ratio, base to curing agent. The PDMS is mixed thoroughly until opaque with bubbles and then degassed in a vacuum desiccator. Finally, the PDMS is poured into the molding apparatus and cured for 6 hours, from oven turn-on, at 60°C. The second photograph in Figure 5-2 shows the silicon master used for making the PDMS stamps used in patterning the organic layers. Each set of 7 columns on the silicon master are pillars made by reactive ion etching with SF_6, $1.5 - 2$ μm in height. The columns, left to right, are pillars with diameters of 50, 25, 20, 15, 10, 5 and 5 μm. The pillars are formed in a square grid with spacing 100 μm, except for the last column of 5 μm pillars, where the spacing is 50 μm.

The PDMS lift-off patterning step consists of placing the stamp onto the substrate and allowing the stamp to sit for several minutes to make conformal contact with the evaporated organic film under the stamp's own weight. For the devices in this chapter, a time of 5 minutes was used. After the contact time, the stamp is peeled off, starting at one of the short edges. The substrates are then returned to the high-vacuum thermal evaporator. A film of Alq_3 doped with DCM is evaporated onto the remaining TPD film, followed by a thin silver mirror, which provides the second mirror for the microcavity.

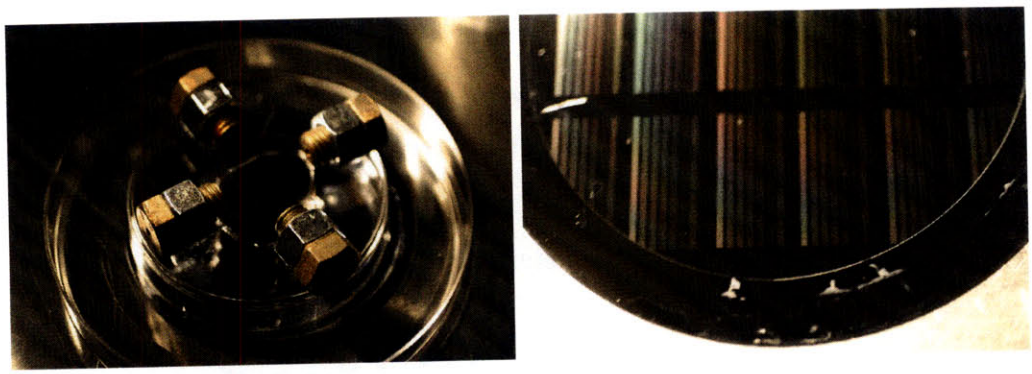

Figure 5-2: Photographs of PDMS casting apparatus which sits atop a 4-inch-diameter silicon wafer and silicon wafer for molding PDMS stamps used to pattern microcavities. A ring made of transparency film helps form a seal between the edge of the plastic petri dish and silicon wafer with the help of the screws used as weights. PDMS (Sylgard 184 from Dow Corning, 10:1 base:curing agent mix) is poured through the hole cut in the petri dish onto the silicon mold and cured in an oven at 60°C for 6 hours (about 30 minutes to 1 hour warm-up time included). The silicon master has 7 columns of pillars made by reactive ion etching with SF_6, $1.5 - 2$ μm in height. The columns, left to right, are pillars with diameters of 50, 25, 20, 15, 10, 5 and 5 μm. The pillars are formed in a square grid with spacing 100 μm, except for the last column of 5 μm pillars, where the spacing is 50 μm.

5.2 Laterally-Patterned Device Photoluminescence

Figure 5-3 shows two photographs of finished devices, with the lateral patterns in the microcavities visible by eye. Also visible are curves likely caused by the surface dynamics of the peeling process, similar to the "coffee rings" which occur when drops of liquids, such as coffee, dry on a surface.

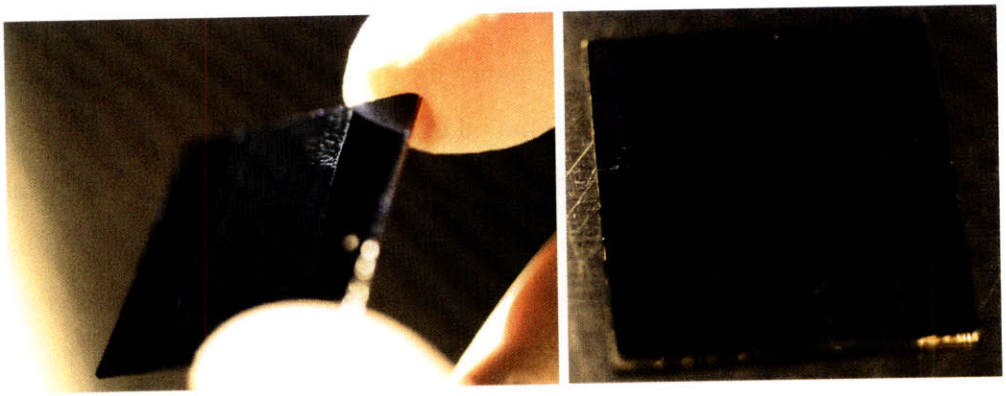

Figure 5-3: Photographs of finished devices, with patterned cavities visible by eye.

The finished devices are optically excited with a $\lambda = 408$ nm light source to

measure the photoluminescence from the patterned microcavities and the background PL from the areas where TPD was lifted off. Figure 5-4(a) shows the PL spectrum measured from the square grid of 5 μm pillars with a spacing of 50 μm. The PL emission spectrum of DCM is also plotted in dashed line. Figure 5-4(b) shows that circular pillar microcavities with a diameter of 5 μm were fabricated.

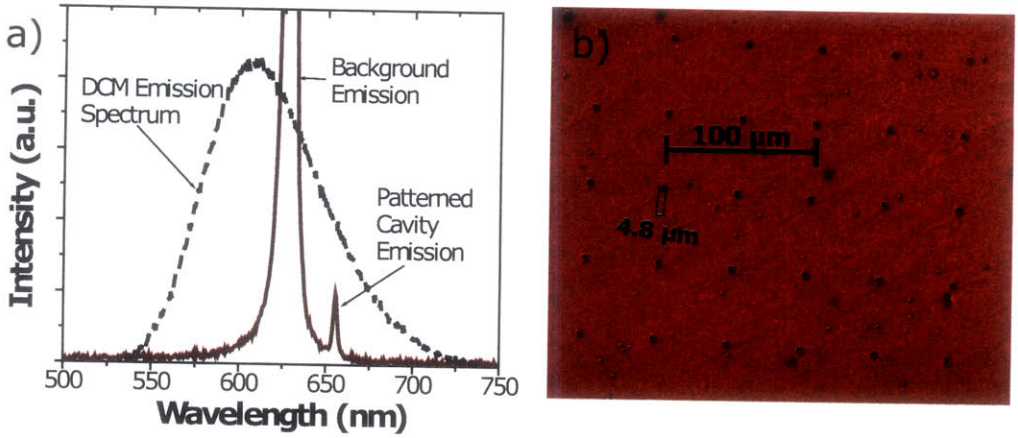

Figure 5-4: (a) Emission spectrum of DCM, lifted-off background, and patterned microcavities when excited with $\lambda = 408$ nm. (b) Microscope image of emission from patterned region showing 5 μm pillars.

The microcavity layers were grown slightly thicker than the targeted amount, which led to the peak in DCM emission being lined up with the emission from the lifted off areas. Nevertheless, emission from both the lifted-off background ($\lambda \approx 630$ nm) and patterned areas ($\lambda \approx 655$ nm) of the sample is observed, as seen in Figure 5-4(a). This shift in wavelength of the cavity resonance by about $25-30$ nm is consistent with the shift expected for lifting off $20-25$ nm of TPD in a metal-DBR microcavity, since a considerable amount of the cavity mode penetrates into the metal mirror, causing the phase shift in reflection to contribute significantly to the Fabry-Perot resonance condition. For a double-DBR microcavity, a greater shift would be expected since the resonance condition of the cavity depends more on the thicknesses of the layers of material between the mirrors as long as the resonance frequency is sufficiently far from the stopband edges of the DBR (where the phase shift of reflection diverges from $\pm\pi$). This amount of lifted-off TPD is consistent with that observed by Yu in

her thesis work on PDMS lift-off patterning. A greater amount of lifted-off material, and therefore shift in the cavity resonance, can be achieved by changing the TPD layer to a different organic material, such as TAZ (3-(Biphenyl-4-yl)-4-phenyl-5-(4-tert-butylphenyl)-1,2,4- triazole), which was shown by Yu [200] to allow for lifted-off amounts of nearly 100 nm or more, since that was the maximum thickness tested.

Although a shift in the microcavity PL resonance was demonstrated in the devices fabricated above, no confinement effects were seen in the PL. This is due to the combination of the lateral size used (minimum 5 μm diameter) and the low quality factor of the metal-DBR microcavities, which have a Q of $100 - 200$ and therefore linewidth of $\Delta\lambda \approx 3 - 6$ nm. Assuming that in these structures the electric field amplitude is zero at the edge of the pillars, which is reasonable since the curved top metal mirror would have some effect on the edges of the pillars, the dispersion of microcavity resonance energies would be given by [61]:

$$E_{cav} = \sqrt{E_0^2 + \frac{\hbar^2 c^2}{n_{eff}^2} \frac{x_{n_\phi, n_r}^2}{R^2}} \tag{5.1}$$

where E_0 is the resonance energy of the same cavity with no lateral confinement (i.e., in the case of these devices, outside of the area patterned by the stamp), n_{eff} is the effective index of refraction inside the microcavity, R is the radius of the cylindrical microcavities, and x_{n_ϕ, n_r} are the n_r^{th} zeros of the Bessel functions $J_{n_\phi}(x_{n_\phi, n_r} r/R)$. For a cylindrical microcavity with diameter 5 μm, these modes will be separated by at most about $\Delta\lambda \approx 2$ nm, meaning that a higher Q microcavity would be needed to make out the quantization of microcavity resonance due to lateral confinement. Additionally, the presence of the background emission from lifted-off areas makes such identification more difficult since the background emission would likely swamp out the emission from the quantized modes. Lastly, the PL was collected from many patterned microcavities, all excited by a large laser excitation spot. Future work should utilize materials such as TAZ that allow for greater amounts of lift-off of the organic microcavity spacer layer. Additionally, a microscope objective should be used to collect emission from a single microcavity, and finally, smaller-diameter

cavities should be patterned. The last change will require the use of a chrome-mask instead of a 50,800-dpi printed transparency mask as used here, for which 5 μm is already below the specified resolution of features.

In conclusion, laterally-patterned organic microcavities were demonstrated showing the successful patterning of single-micron-scale features using the PDMS lift-off patterning technique. This work demonstrates that organic devices laterally patterned on the size scale of the wavelength of visible light are achievable with PDMS lift-off patterning, meaning that 0D microcavities can be fabricated in these systems, either for use in traditional laser devices using organic laser dyes or in exciton-polariton devices using J aggregates or other active materials.

Chapter 6

Conclusion: Outlook for J-Aggregate and Organic Exciton-Polariton Devices

In this thesis, the linear and nonlinear optical properties of J-aggregate thin films have been investigated (Chapters 2 and 3), higher-Q microcavity double-DBR J-aggregate exciton-polariton devices were fabricated and their PL spectra examined (Chapter 4), and a method of fabricating single-micron-scale laterally-patterned organic microcavities was demonstrated (Chapter 5). In addition, in Chapter 1, the literature on exciton-polaritons in both inorganic and organic systems was reviewed, including a comparison of the threshold of traditional organic lasers to what might be expected for organic exciton-polariton lasers. As an overall conclusion to the work presented in this thesis, I will discuss my own take on the outlook of research in devices based on J-aggregate materials and in organic exciton-polariton devices.

6.1 Outlook for J-Aggregate-based Devices

Throughout the research presented in the previous chapters, the photostability of the J-aggregate active materials was a continual challenge, especially when photoluminescence or other types of strong optical excitation was utilized, such as in the

pump-probe work. TDBC (or BIC) in particular was found to be particularly susceptible to photobleaching, which motivated my use of THIATS in the devices shown in Chapter 4. Though, while I found THIATS to be more stable than TDBC, it still bleached during the top-mirror sputtering and tended to bleach substantially when I tried direct pumping of the J-aggregate layer in the Chapter 4 devices. Where THIATS outlasted TDBC was specifically in holding up during pumping by down-conversion through the Alq_3:DCM layer; TDBC, in a similar device pumped by only Alq_3 (DCM was unnecessary thanks to the bluer resonance of TDBC than that of THIATS) and presented in the thesis of Tischler [188], could be bleached completely by the Alq_3 emission within the cavity.

The issue with cyanines in general, however, has been their susceptibility to photodegredation by the same singlet oxygen that their excitation tends to produce. This was as true with the original CD-recordables (CDRs) using cyanines as it is with the J-aggregate exciton-polariton devices demonstrated in this thesis using cyanines. In the case of CDRs, cyanines have persisted only with the help of stabilization by nickel metal-chelates, which both quench singlet oxygen and the excited states of the cyanines that give rise to singlet oxygen. It may be that the photostability lifetime of cyanines in devices requiring luminescence may be extended by reducing the threat of singlet oxygen (with metal-chelate dopants and choice of cyanine family with fewer singlet-oxygen reactive sites, like the thiacyanines), but I think that in order to have a significant role in technology as either light sources or nonlinear optical materials, the set of J-aggregating dyes will need to be extended to dye families that are more photostable.

That cyanines are utilized as J-aggregating dyes is really just an accident of history. One of the only technological applications that has utilized J aggregates extensively has been narrow-wavelength-range sensitizers for silver halide emulsions for use in scientific applications such as photography in astronomy. While this type of application kept J aggregates in use since their discovery, increases in stability were not required due to the single-shot use of the materials in such applications. And, since only cyanines were known to J aggregate, few if any further materials sets have

been developed synthetically strictly for the purpose of making J aggregates. Despite the limitation of cyanine dye's photostability, the strong dipole-dipole coupling in J aggregation has been recognized in the past two decades as a promising tool for realizing a variety of physical phenomena, especially due to the long range coherent quantum state that is implicit in the aggregate's physics. Thus, with some creative chemistry with various dye families to enable the brickwork self-assembly of J aggregation, many more J aggregates may be realized in the coming years that have the same strong optical response and have increased stability, allowing for J aggregates to make an imprint on various photonic technologies in the next decades.

6.2 Outlook for Organic Exciton-Polariton Devices

Aside from the stability issues discussed above for J aggregates, the outlook for organic exciton-polariton devices depends strongly on the type of device considered. For starters, one should distinguish between devices that are based on simply high-Q microcavities and ones that rely on polariton-polariton interactions or the physics of polaritons as quasiparticles. The distinction is somewhat artificial and simply a matter of semantics, though it can be understood to hinge on what the exciton-exciton interaction is in organic exciton-polariton systems since that interaction governs how polaritons interact with one another.

In the former category would be placed nonlinear optical switches (i.e., optically-bistable devices) utilizing strongly-coupled organic materials as the saturable absorber/dispersive medium. In these systems, the use of a strongly nonlinear material with narrow resonance (e.g., J aggregates) with the feedback of a high-quality microcavity enables nonlinearities achievable at low excitation intensities. Since exciton-exciton interactions are not invoked to create a superfluid state or some type of scattering, one can view the presence of exciton-polaritons in these systems as incidental– moving from weak to strong coupling simply causes a lowering of the required excitation intensity.

In the latter category would be placed polariton optical parametric oscillators

(OPOs) and polariton lasers, which rely on polariton-polariton interactions to create a macroscopic coherent population that in the case of the polariton laser may also have the properties of a superfluid. In these devices, the exciton-exciton interaction is a critical component of the physics and is the least understood for organic exciton-polaritons.

As discussed in Chapter 1, both the four-level system inherent in most organic laser dyes and exciton-polariton lasers are inversionless, requiring only enough pumping to overcome decay processes and therefore maintain a coherent population. For exciton-polaritons to cause any lowering of the lasing threshold comparable to that which occurs in inorganic systems, the increased physical size of the polariton over a single exciton's cross-section will have to give enough of a boost to overcome the increased loss due to efficient decay via the cavity. If one takes the theoretical predictions of polariton superfluidity transition density in GaN as an estimate for that in organic systems, the threshold of an exciton-polariton laser *at best* would be equal to that of most organic VCSELs. What those predictions hinge on, however, is the interparticle interaction potential, which is very likely quite different for Frenkel excitons than for Wannier-Mott excitons. Thus, to truly gauge the potential of organic exciton-polaritons as low-threshold lasers, the weakly-interacting Bose gas or Dicke models will need to be adapted for interacting Frenkel-type exciton active materials.

The outlook for polariton OPOs has the same if not greater dependence on understanding the interaction of Frenkel-exciton-polaritons since the device is fundamentally based on scattering events between two polaritons (i.e., the exciton components of two polaritons), though the strong exciton-exciton annihilation that occurs in organic materials makes such the realization of polariton OPOs in organic systems seem unlikely. Only a single published pump-probe experiment has been done on organic exciton-polariton systems in an OPO-type configuration as noted earlier in the thesis, but the use of a CT exciton coupled to the cavity likely doomed any possible population build-up in the system due to fast CT-to-singlet exciton scattering in the active material.

Despite the lack of theorertical understanding that persists and makes the outlook

for organic exciton-polariton devices unclear, two specific areas come to mind that would still warrant experimental investigation without further theoretical developments. First, hybrid organic-inorganic exciton-polariton devices have already been demonstrated, but the dynamics of energy transfer via the strongly-coupled shared cavity mode have not been thoroughly investigated. Such a structure could allow for the efficient conversion of electrically-injected excitons in the inorganic material to excitons in the organic material. Second, although polariton lasing has not been achieved in organic structures by relaxation of excitations in the strongly-coupled material, the PL spectra shown in Chapter 4 in this thesis suggest that a laser could be made in a strongly-coupled structure that lases in the strongly-coupled mode, with gain provided by a laser dye in the spacer materials. What such lasing might imply for coherence amongst the excitons in the strongly-coupled material would be a worthwhile investigation in and of itself, including determining the effects of the strong coupling on the laser threshold and investigating any exciton-exciton or polariton-polariton interactions that may occur as well.

6.3 Conclusion

In conclusion, the outlook for J-aggregate materials will depend on advances in dye chemistry in the coming decades; making J-aggregating materials from stable dye families may bridge the gap between the physics research of the past two decades and actual technological applications. For organic exciton-polaritons, with what we now understand about the physics of such systems, investigations in long-range energy transfer via polaritons and the effects of strong coupling on traditional lasing still may yield technological applications. Judging from inorganic exciton-polariton laser theory, it is unlikely that organic exciton-polariton lasers will have lower thresholds than existing organic solid-state dye lasers, and organic polariton OPOs thus far seem unlikely due to exciton-exciton annihilation, but in both cases theoretical investigations of Bose gases with Frenkel-type exciton interaction potentials would yield important information, and in such investigations the actual homogeneous broadening

of J-aggregate thin films reported in this thesis would be an important parameter.

Overall, the device and engineering advances described in this thesis will enable more accurate theoretical investigations in the dyanmics of exciton-polaritons in organic systems, and the materials and fabrication advances described, specifically higher-Q microcavities and lateral-patterning of single-micron-scale structures, will enable further experimental investigations into the dynamics of organic strongly-coupled light-matter systems.

Appendix A

Authored and Co-Authored Papers Relating to Thesis

The work in Chapter 2 was published in Bradley *et al.* [23] and occurred at the end of the study published in Tischler *et al.* [189]. The study in Chapter 3 was published in Bradley *et al.* [24]. Relating to the CCRs described in Chapter 4 was the published work in Tischler *et al.* [186], and a review article of all of the above was published in Tischler *et al.* [187].

The linear optical modeling with T-matrices described in Chapters 2 and 3 was also used in the study by Wood *et al.*, in press in *Advanced Materials* as of early 2009, and a study by Mei *et al.*, which has been submitted and is in the review process.

Bibliography

[1] V. M. Agranovich, D. M. Basko, G. C. La Rocca, and F. Bassani. Excitons and optical nonlinearities in hybrid organic-inorganic nanostructures. *J. Phys.-Condes. Matter*, 10(42):9369–9400, 1998.

[2] V. M. Agranovich and G. C. La Rocca. Electronic excitations in organic microcavities with strong light-matter coupling. *Solid State Commun.*, 135(9-10): 544–553, 2005.

[3] V. M. Agranovich, M. Litinskaia, and D. G. Lidzey. Microcavity polaritons in materials with weak intermolecular interaction. *Phys. Status Solidi B-Basic Res.*, 234(1):130–138, 2002.

[4] V. M. Agranovich, M. Litinskaia, and D. G. Lidzey. Cavity polaritons in microcavities containing disordered organic semiconductors. *Phys. Rev. B*, 67(8): 085311–085310, 2003.

[5] Katsuhiko Ariga, Yuri Lvov, and Toyoki Kunitake. Assembling alternate dye-polyion molecular films by electrostatic layer-by-layer adsorption. *J. Am. Chem. Soc.*, 119(9):2224–2231, 1997.

[6] A. Armitage, D. Lidzey, D. D. C. Bradley, T. Virgili, M. S. Skolnick, and S. Walker. Modelling of asymmetric excitons in organic microcavities. *Synth. Met.*, 111:377–379, 2000.

[7] Tolga Atay, Qiang Zhang, Arto Nurmikko, Jonathan Tischler, Scott Bradley, and Vladimir Bulović. Ultrafast exciton response of high optical density j-aggregates from ultrathin films of cyanine dyes. In *CLEO/QELS 2006*, Long Beach, CA, May 23, 2006.

[8] Tolga Atay, Qiang Zhang, Arto Nurmikko, Jonathan Tischler, Scott Bradley, and Vladimir Bulović. Ultrafast exciton response of high optical density j-aggregates from ultrathin films of cyanine dyes. In *MRS Fall 2006*, Boston, MA, November 29, 2006.

[9] D. Bajoni, E. Peter, P. Senellart, J. L. Smirr, I. Sagnes, A. Lemaitre, and J. Bloch. Polariton parametric luminescence in a single micropillar. *Appl. Phys. Lett.*, 90(5), 2007.

[10] D. Bajoni, E. Semenova, A. Lemaitre, S. Bouchoule, E. Wertz, P. Senellart, and J. Bloch. Polariton light-emitting diode in a gaas-based microcavity. *Phys. Rev. B*, 77(11), 2008.

[11] D. Bajoni, P. Senellart, A. Lemaitre, and J. Bloch. Photon lasing in gaas microcavity: Similarities with a polariton condensate. *Phys. Rev. B*, 76(20), 2007.

[12] D. Bajoni, E. Wertz, P. Senellart, A. Miard, E. Semenova, A. Lemaitre, I. Sagnes, S. Bouchoule, and J. Bloch. Excitonic polaritons in semiconductor micropillars. pages 933–943, 2008.

[13] D. B. Balagurov, G. C. La Rocca, and V. M. Agranovich. Coherent-potential-approximation study of excitonic absorption in orientationally disordered molecular aggregates. *Phys. Rev. B*, 68(4):045418, Jul 2003.

[14] M. A. Baldo, R. J. Holmes, and S. R. Forrest. Prospects for electrically pumped organic lasers. *Phys. Rev. B*, 66(3):035321, Jul 2002.

[15] R. Balili, V. Hartwell, D. Snoke, L. Pfeiffer, and K. West. Bose-einstein condensation of microcavity polaritons in a trap. *Science*, 316(5827):1007–1010, 2007.

[16] J. J. Baumberg and P. G. Lagoudakis. Parametric amplification and polariton liquids in semiconductor microcavities. *Physica Status Solidi B-Basic Solid State Physics*, 242(11):2210–2223, 2005.

[17] J. J. Baumberg, P. G. Savvidis, R. M. Stevenson, A. I. Tartakovskii, M. S. Skolnick, D. M. Whittaker, and J. S. Roberts. Parametric oscillation in a vertical microcavity: A polariton condensate or micro-optical parametric oscillation. *Phys. Rev. B*, 62(24):R16247–R16250, 2000.

[18] D. Baxter, M. S. Skolnick, A. Armitage, V. N. Astratov, D. M. Whittaker, T. A. Fisher, J. S. Roberts, D. J. Mowbray, and M. A. Kaliteevski. Polarization-dependent phenomena in the reflectivity spectra of semiconductor quantum microcavities. *Phys. Rev. B*, 56(16):10032–10035, 1997.

[19] M. Bednarz, V. A. Malyshev, and J. Knoester. Temperature dependent fluorescence in disordered frenkel chains: Interplay of equilibration and local band-edge level structure. *Phys. Rev. Lett.*, 91(21):217401, Nov 2003.

[20] F. Boeuf, R. Andre, R. Romestain, L. Dang, E. Peronne, J. F. Lampin, D. Hulin, and A. Alexandrou. Evidence of polariton stimulation in semiconductor microcavities. *Phys. Status Solidi A*, pages 29–33, 2001.

[21] F. Boeuf, R. Andre, R. Romestain, L. St Dang, E. Peronne, J. F. Lampin, D. Hulin, and A. Alexandrou. Mechanism of polariton-stimulation in a cdte-based microcavity. pages 129–132, 2000.

[22] Eugene G. Bortchagovsky and Ulrich C. Fischer. Method for determination of the dielectric function of a thin absorbing film on variable substrates from transmission spectra. *Appl. Opt.*, 42(34):6915–6918, 2003.

[23] M. S. Bradley, J. R. Tischler, and V. Bulovic. Layer-by-layer j-aggregate thin films with a peak absorption constant of 10(6) cm(-1). *Adv. Mater.*, 17(15): 1881–1886, 2005.

[24] M. S. Bradley, J. R. Tischler, Y. Shirasaki, and V. Bulovic. Predicting the linear optical response of j-aggregate microcavity exciton-polariton devices. *Phys. Rev. B*, 78(19):193305, 2008.

[25] V. Bulović, V. G. Kozlov, V. B. Khalfin, and S. R. Forrest. Transform-Limited, Narrow-Linewidth Lasing Action in Organic Semiconductor Microcavities. *Science*, 279(5350):553–555, 1998. URL `http://www.sciencemag.org/cgi/content/abstract/279/5350/553`.

[26] R. Butte, G. Delalleau, A. I. Tartakovskii, M. S. Skolnick, V. N. Astratov, J. J. Baumberg, G. Malpuech, A. Di Carlo, A. V. Kavokin, and J. S. Roberts. Transition from strong to weak coupling and the onset of lasing in semiconductor microcavities. *Phys. Rev. B*, 65(20), 2002.

[27] R. Butte, M. Emam-Ismail, A. Lemaitre, R. M. Stevenson, M. S. Skolnick, D. M. Whittaker, A. I. Tartakovskii, J. J. Baumberg, P. G. Savvidis, and J. S. Roberts. Pump angle and laser energy dependence of stimulated scattering in microcavities. pages 333–338, 2002.

[28] V. E. Campbell, P. A. Chiarelli, S. Kaur, and M. S. Johal. Coadsorption of a polyanion and an azobenzene dye in self-assembled and spin-assembled polyelectrolyte multilayers. *Chem. Mater.*, 17(1):186–190, 2005.

[29] A. Camposeo, L. Persano, P. Del Carro, T. Virgili, R. Cingolani, and D. Pisignano. Polarization splitting in organic-based microcavities working in the strong coupling regime. *Org. Electron.*, 8(2-3):114–119, 2007.

[30] H. Cao, S. Pau, J. M. Jacobson, G. Björk, Y. Yamamoto, and A. Imamo˘glu. Transition from a microcavity exciton polariton to a photon laser. *Phys. Rev. A*, 55(6):4632–4635, Jun 1997.

[31] S. C. Chiao, B. G. Bovard, and H. A. Macleod. Optical-constant calculation over an extended spectral region - application to titanium-dioxide film. *Appl. Opt.*, 34(31):7355–7360, 1995.

[32] P. A. Chiarelli, M. S. Johal, D. J. Holmes, J. L. Casson, J. M. Robinson, and H. L. Wang. Polyelectrolyte spin-assembly. *Langmuir*, 18(1):168–173, 2002.

[33] Jinhan Cho, Kookheon Char, Jong-Dal Hong, and Ki-Bong Lee. Fabrication of highly ordered multilayer films using a spin self-assembly method. *Adv. Mater.*, 13(14):1076–1078, 2001.

[34] J. Chovan, I. E. Perakis, S. Ceccarelli, and D. G. Lidzey. Controlling the interactions between polaritons and molecular vibrations in strongly coupled organic semiconductor microcavities. *Phys. Rev. B*, 78(4), 2008.

[35] G. Christmann, R. Butte, E. Feltin, J. F. Carlin, and N. Grandjean. Room temperature polariton lasing in a gan/algan multiple quantum well microcavity. *Appl. Phys. Lett.*, 93(5), 2008.

[36] S. Christopoulos, G. B. H. von Hogersthal, A. J. D. Grundy, P. G. Lagoudakis, A. V. Kavokin, J. J. Baumberg, G. Christmann, R. Butte, E. Feltin, J. F. Carlin, and N. Grandjean. Room-temperature polariton lasing in semiconductor microcavities. *Phys. Rev. Lett.*, 98(12), 2007.

[37] Shun Lien Chuang. *Physics of Optoelectronic Devices.* Wiley-Interscience, New York, 1995.

[38] Claude Cohen-Tannoudji, Jacques Dupont-Roc, and Gilbert Grynberg. *Atom-Photon Interactions.* Wiley-VCH, Weinheim, 2004.

[39] L. A. Coldren and S. W. Corzine. *Diode Lasers and Photonic Integrated Circuits.* John Wiley & Sons, Inc., New York, 1995.

[40] L. G. Connolly, D. G. Lidzey, R. Butte, A. M. Adawi, D. M. Whittaker, M. S. Skolnick, and R. Airey. Strong coupling in high-finesse organic semiconductor microcavities. *Applied Physics Letters*, 83(26):5377–5379, 2003. URL `http://link.aip.org/link/?APL/83/5377/1`.

[41] M. Cooper, A. Ebner, M. Briggs, M. Burrows, N. Gardner, R. Richardson, and R. West. Cy3b (tm): Improving the performance of cyanine dyes. *J. Fluoresc.*, 14(2):145–150, 2004.

[42] L. Dahne, A. Horvath, and G. Weiser. Optical properties of a streptocyanine dye single crystal with tubelike aggregation: bis(dimethylamino)-heptamethinium tetrafluoroborate bdh+bf-4. *Chem. Phys.*, 178(1-3):449–457, 1993.

[43] L. S. Dang, D. Heger, R. Andre, F. Boeuf, and R. Romestain. Stimulation of polariton photoluminescence in semiconductor microcavity. *Phys. Rev. Lett.*, 81(18):3920–3923, 1998.

[44] G. Decher. Polyelectrolyte multilayers, an overview. In Gero Decher and Joseph B. Schlenoff, editors, *Multilayer Thin Films*, pages 1–46. Wiley-VCH Verlag GmbH & Co. KGaA, Weinheim, 2002.

[45] G. Decher and J. D. Hong. Buildup of ultrathin multilayer films by a self-assembly process: Ii. consecutive adsorption of anionic and cationic bipolar amphiphiles and polyelectrolytes on charged surfaces. *Berichte der Bunsen-Gesellschaft*, 95(11):1430–1434, 1991.

[46] G. Decher, J. D. Hong, and J. Schmitt. Buildup of ultrathin multilayer films by a self-assembly process .3. consecutively alternating adsorption of anionic and cationic polyelectrolytes on charged surfaces. *Thin Solid Films*, 210(1-2): 831–835, 1992.

[47] Gero Decher. Fuzzy nanoassemblies: toward layered polymeric multicomposites. *Science*, 277(5330):1232–1237, 1997.

[48] Gero Decher and Jong Dal Hong. Buildup of ultrathin multilayer films by a self-assembly process. 1. consecutive adsorption of anionic and cationic bipolar amphiphiles on charged surfaces. *Makromolekulare Chemie, Macromolecular Symposia*, 46(Eur. Conf. Organ. Org. Thin Films, 3rd, 1990):321–327, 1991.

[49] Gero Decher and J. Schmitt. Fine-tuning of the film thickness of ultrathin multilayer films composed of consecutively alternating layers of anionic and cationic polyelectrolytes. *Progress in Colloid & Polymer Science*, 89(Trends Colloid Interface Sci. VI):160–164, 1992.

[50] H. Deng, G. Weihs, C. Santori, J. Bloch, and Y. Yamamoto. Condensation of semiconductor microcavity exciton polaritons. *Science*, 298(5591):199–202, 2002.

[51] A. B. Djurisic, T. Fritz, K. Leo, and E. H. Li. Improved method for determination of optical constants of organic thin films from reflection and transmission measurements. *Appl. Opt.*, 39(7):1174–1182, 2000.

[52] M.S. Dresselhaus. Solid state physics, 2001.

[53] Raymond S. Eachus, Alfred P. Marchetti, and Annabel A. Muenter. The photophysics of silver halide imaging materials. *Annu. Rev. Phys. Chem.*, 50(1): 117–144, 1999.

[54] P. R. Eastham and P. B. Littlewood. Bose condensation in a model microcavity. *Solid State Commun.*, 116(7):357–361, 2000.

[55] O. El Daif, A. Baas, T. Guillet, J. P. Brantut, R. I. Kaitouni, J. L. Staehli, F. Morier-Genoud, and B. Deveaud. Polariton quantum boxes in semiconductor microcavities. *Appl. Phys. Lett.*, 88(6), 2006.

[56] O. El Daif, G. Nardin, T. K. Paraiso, A. Baas, M. Richard, J. P. Brantut, T. Guillet, F. Morier-Genoud, and B. Deveaud-Pledran. Nonlinear relaxation of zero-dimension-trapped microcavity polaritons. *Appl. Phys. Lett.*, 92(8), 2008.

[57] D. Englund, A. Faraon, I. Fushman, N. Stoltz, P. Petroff, and J. Vuckovic. Controlling cavity reflectivity with a single quantum dot. *Nature*, 450:857–861, 2007.

[58] T. Feurer, Nikolay S. Stoyanov, David W. Ward, Joshua C. Vaughan, Eric R. Statz, and Keith A. Nelson. Terahertz polaritonics. *Annu. Rev. Mater. Res.*, 37 (1):317–350, 2007. URL `http://arjournals.annualreviews.org/doi/abs/10.1146/annurev.matsci.37.052506.084327`.

[59] J. M. Fink, M. Goppl, M. Baur, R. Bianchetti, P. J. Leek, A. Blais, and A. Wallraff. Climbing the jaynes-cummings ladder and observing its root n nonlinearity in a cavity qed system. *Nature*, 454(7202):315–318, 2008.

[60] Hiroshi Fukumoto and Yoshiro Yonezawa. Layer-by-layer self-assembly of polyelectrolyte and water soluble cyanine dye. *Thin Solid Films*, 327-329:748–751, 1998.

[61] T. Gutbrod, M. Bayer, A. Forchel, J. P. Reithmaier, T. L. Reinecke, S. Rudin, and P. A. Knipp. Weak and strong coupling of photons and excitons in photonic dots. *Phys. Rev. B*, 57(16):9950–9956, 1998.

[62] Peter L. Hagelstein, Stephen D. Senturia, and Terry P. Orlando. *Introductory Applied Quantum and Statistical Mechanics.* Wiley-Interscience, Hoboken, 2004.

[63] P. A. Hobson, W. L. Barnes, D. G. Lidzey, G. A. Gehring, D. M. Whittaker, M. S. Skolnick, and S. Walker. Strong exciton-photon coupling in a low-q all-metal mirror microcavity. *Appl. Phys. Lett.*, 81(19):3519–3521, 2002.

[64] R. J. Holmes and S. R. Forrest. Strong exciton-photon coupling and exciton hybridization in a thermally evaporated polycrystalline film of an organic small molecule. *Phys. Rev. Lett.*, 93(18):186404–186404, 2004.

[65] R. J. Holmes and S. R. Forrest. Strong exciton-photon coupling in organic materials. *Org. Electron.*, 8(2-3):77–93, 2007.

[66] R. J. Holmes, S. Kena-Cohen, V. M. Menon, and S. R. Forrest. Strong coupling and hybridization of frenkel and wannier-mott excitons in an organic-inorganic optical microcavity. *Phys. Rev. B*, 74(23), 2006.

[67] J. J. Hopfield. Theory of the contribution of excitons to the complex dielectric constant of crystals. *Physical Review*, 112(5):1555–1567, 1958.

[68] Hiroaki Horiuchi, Sachiko Ishibashi, Seiji Tobita, Mamoru Uchida, Masanori Sato, Ken-ichi Toriba, Kunihiko Otaguro, and Hiroshi Hiratsuka. Photodegradation processes of cyanine dyes in the film state induced by singlet molecular oxygen. *The Journal of Physical Chemistry B*, 107(31):7739–7746, 2003. URL `http://pubs.acs.org/doi/abs/10.1021/jp027299n`.

[69] R. Houdre, R. P. Stanley, and M. Ilegems. Vacuum-field rabi splitting in the presence of inhomogeneous broadening: Resolution of a homogeneous linewidth in an inhomogeneously broadened system. *Phys. Rev. A*, 53(4):2711–2715, 1996.

[70] A. Imamoglu, R. J. Ram, S. Pau, and Y. Yamamoto. Nonequilibrium condensates and lasers without inversion: Exciton-polariton lasers. *Phys. Rev. A*, 53 (6):4250–4253, 1996.

[71] E.T. Jaynes and F.W. Cummings. Comparison of quantum and semiclassical radiation theories with application to the beam maser. 51(1):89–109, Jan. 1963. ISSN 0018-9219.

[72] S. Jaziri, H. Abassi, K. Sellami, and R. Bennaceur. Bose-einstein condensation of polaritons in organic semiconducting microcavities. *Phys. Status Solidi A*, pages 441–445, 2002.

[73] Edwin E. Jelley. Spectral absorption and fluorescence of dyes in the molecular state. *Nature*, 138:1009–1010, 1936.

[74] M. S. Johal, J. L. Casson, P. A. Chiarelli, D. G. Liu, J. A. Shaw, J. M. Robinson, and H. L. Wang. Polyelectrolyte trilayer combinations using spin-assembly and ionic self-assembly. *Langmuir*, 19(21):8876–8881, 2003.

[75] R. Johne, D. D. Solnyshkov, and G. Malpuech. Theory of exciton-polariton lasing at room temperature in zno microcavities. *Appl. Phys. Lett.*, 93(21), 2008.

[76] J. Kasprzak, M. Richard, S. Kundermann, A. Baas, P. Jeambrun, J. M. J. Keeling, F. M. Marchetti, M. H. Szymanska, R. Andre, J. L. Staehli, V. Savona, P. B. Littlewood, B. Deveaud, and L. S. Dang. Bose-einstein condensation of exciton polaritons. *Nature*, 443(7110):409–414, 2006.

[77] A. Kavokin. Exciton-polaritons in microcavities: present and future. *Applied Physics a-Materials Science & Processing*, 89(2):241–246, 2007.

[78] A. Kavokin, G. Malpuech, and F. P. Laussy. Polariton laser and polariton superfluidity in microcavities. *Phys. Lett. A*, 306(4):187–199, 2003.

[79] Alexey Kavokin, Jeremy J. Baumberg, Guillaume Malpuech, and Fabrice P. Laussy. *Microcavities.* Oxford University Press, Oxford, 2007.

[80] Mitsuo Kawasaki, Tomoo Sato, and Takayo Yoshimoto. Controlled layering of two-dimensional j-aggregate of anionic cyanine dye on self-assembled cysteamine monolayer on au(111). *Langmuir*, 16(12):5409–5417, 2000.

[81] David R. Kearns. Physical and chemical properties of singlet molecular oxygen. *Chemical Reviews*, 71(4):395–427, 1971. URL `http://pubs.acs.org/doi/abs/10.1021/cr60272a004`.

[82] J. Keeling, F. M. Marchetti, M. H. Szymanska, and P. B. Littlewood. Collective coherence in planar semiconductor microcavities. *Semicond. Sci. Technol.*, 22 (5):R1–R26, 2007.

[83] S Kena-Cohen, M. Davanco, and S. R. Forrest. Strong exciton-photon coupling in an organic single crystal microcavity. *Physical Review Letters*, 101(11): 116401, 2008. URL `http://link.aps.org/abstract/PRL/v101/e116401`.

[84] S. Kena-Cohen and S. R. Forrest. Green polariton photoluminescence using the red-emitting phosphor ptoep. *Phys. Rev. B*, 76(7), 2007.

[85] A. A. Khalifa, A. P. D. Love, D. N. Krizhanovskii, M. S. Skolnick, and J. S. Roberts. Electroluminescence emission from polariton states in gaas-based semiconductor microcavities. *Appl. Phys. Lett.*, 92(6), 2008.

[86] G. Khitrova, H. M. Gibbs, F. Jahnke, M. Kira, and S. W. Koch. Nonlinear optics of normal-mode-coupling semiconductor microcavities. *Reviews of Modern Physics*, 71(5):1591–1639, 1999.

[87] G. Khitrova, H. M. Gibbs, M. Kira, S. W. Koch, and A. Scherer. Vacuum rabi splitting in semiconductors. *Nat. Phys.*, 2(2):81–90, 2006.

[88] H. J. Kimble. Structure and dynamics in cavity quantum electrodynamics. In P. R. Berman and David Bates, editors, *Cavity Quantum Electrodynamics*, Advances in Atomic, Molecular, and Optical Physics. Academic Press, Inc., San Diego, 1994.

[89] P. Kinsler and D. M. Whittaker. Linewidth narrowing of polaritons. *Phys. Rev. B*, 54(7):4988–4995, 1996.

[90] M. Kira, F. Jahnke, S. W. Koch, J. D. Berger, D. V. Wick, T. R. Nelson, G. Khitrova, and H. M. Gibbs. Quantum theory of nonlinear semiconductor microcavity luminescence explaining ıboserȷ experiments. *Phys. Rev. Lett.*, 79 (25):5170–5173, Dec 1997.

[91] J. Knoester. Modeling the optical properties of excitons in linear and tubular j-aggregates. *Int. J. Photoenergy*, 2006.

[92] T. Kobayashi, editor. *J-Aggregates.* World Scientific Publishing Co. Pte. Ltd., Singapore, 1996.

[93] Jin Au Kong. *Electromagnetic Wave Theory.* EMW Publishing, Cambridge, 2005.

[94] M. Koschorreck, R. Gehlhaar, V. G. Lyssenko, M. Swoboda, M. Hoffmann, and K. Leo. Dynamics of a high-q vertical-cavity organic laser. *Appl. Phys. Lett.*, 87(18):181108, 2005. URL `http://link.aip.org/link/?APL/87/181108/1`.

[95] J M Kosterlitz and D J Thouless. Ordering, metastability and phase transitions in two-dimensional systems. *Journal of Physics C: Solid State Physics*, 6(7): 1181–1203, 1973. URL `http://stacks.iop.org/0022-3719/6/1181`.

[96] V. G. Kozlov, V. Bulovic, P. E. Burrows, M. Baldo, V. B. Khalfin, G. Parthasarathy, S. R. Forrest, Y. You, and M. E. Thompson. Study of lasing action based on f[o-umlaut]rster energy transfer in optically pumped organic semiconductor thin films. *J. Appl. Phys.*, 84(8):4096–4108, 1998. URL `http://link.aip.org/link/?JAP/84/4096/1`.

[97] H. Kuhn, Dietmar Mbius, and Hermann Bcher. Spectroscopy of monolayer assemblies. In Arnold Weissberger and Bryant Rossiter, editors, *Physical Methods of Chemistry: Part IIIB Optical, Spectroscopic, and Radioactivity Methods*, Techniques of Chemistry. Wiley-Interscience, New York, 1972.

[98] M. Langner, R. Gehlhaar, S. I. Hintschich, H. Frob, H. Wendrock, V. G. Lyssenko, and K. Leo. Optical modes in wavelength-sized organic microcavity structures. pages 403–409, 2008.

[99] M. Langner, R. Gehlhaar, C. Schriever, H. Frob, V. G. Lyssenko, and K. Leo. Strong optical confinement and multimode emission of organic photonic dots. *Appl. Phys. Lett.*, 91(18), 2007.

[100] Maik Langner, Markas Sudzius, Susanne I. Hintschich, Hartmut Frob, Vadim G. Lyssenko, and Karl Leo. Sub-nanojule threshold lasing in 5 x 5 mu m[sup 2] organic photonic boxes. volume 6999, page 699902. SPIE, 2008. URL `http://link.aip.org/link/?PSI/6999/699902/1`.

[101] S. S. Lee, K. B. Lee, and J. D. Hong. Evidence for spin coating electrostatic self-assembly of polyelectrolytes. *Langmuir*, 19(18):7592–7596, 2003.

[102] C. J. Lefaux, J. A. Zimberlin, A. V. Dobrynin, and P. T. Mather. Polyelectrolyte spin assembly: Influence of ionic strength on the growth of multilayered thin films. *Journal of Polymer Science Part B-Polymer Physics*, 42(19):3654–3666, 2004.

[103] D. R. Lide, editor. *CRC Handbook of Chemistry and Physics.* CRC Press LLC, Boca Raton, FL, 81st edition, 2000.

[104] D. G. Lidzey, D. D. C. Bradley, M. S. Skolnick, T. Virgili, S. Walker, and D. M. Whittaker. Strong exciton-photon coupling in an organic semiconductor microcavity. *Nature*, 395(6697):53–55, 1998.

[105] D. G. Lidzey, D. D. C. Bradley, T. Virgili, A. Armitage, M. S. Skolnick, and S. Walker. Room temperature polariton emission from strongly coupled organic semiconductor microcavities. *Phys. Rev. Lett.*, 82(16):3316–3319, 1999.

[106] D. G. Lidzey, J. Wenus, D. M. Whittaker, G. Itskos, P. N. Stavrinou, D. D. C. Bradley, and R. Murray. Hybrid polaritons in strongly coupled microcavities: experiments and models. *J. Lumines.*, 110(4):347–353, 2004.

[107] D.G Lidzey, T Virgili, D.D.C Bradley, M.S Skolnick, S Walker, and D.M Whittaker. Observation of strong exciton-photon coupling in semiconductor microcavities containing organic dyes and j-aggregates. *Optical Materials*, 12(2-3):243 – 247, 1999. ISSN 0925-3467. URL `http://www.sciencedirect.com/science/article/B6TXP-3X4WCT0-D/2/945a145be1cd2c628706a26644c6e804`.

[108] M. Litinskaya. Exciton polariton kinematic interaction in crystalline organic microcavities. *Phys. Rev. B*, 77(15), 2008.

[109] M. Litinskaya. Propagation and localization of polaritons in disordered organic microcavities. *Phys. Lett. A*, 372(21):3898–3903, 2008.

[110] M. Litinskaya and P. Reineker. Loss of coherence of exciton polaritons in inhomogeneous organic microcavities. *Phys. Rev. B*, 74(16):165320, 2006.

[111] M. Litinskaya and P. Reineker. Balance between incoming and outgoing cavity polaritons in a disordered organic microcavity. *J. Lumines.*, 122:418–420, 2007.

[112] M. Litinskaya, P. Reineker, and V. M. Agranovich. Exciton-polaritons in a crystalline anisotropic organic microcavity. *Phys. Status Solidi A*, 201(4):646–654, 2004.

[113] M. Litinskaya, P. Reineker, and V. M. Agranovich. Fast polariton relaxation in strongly coupled organic microcavities. *J. Lumines.*, 110(4):364–372, 2004.

[114] M. Litinskaya, P. Reineker, and V. M. Agranovich. Exciton-polaritons in organic microcavities. *J. Lumines.*, 119:277–282, 2006.

[115] Z. T. Liu, C. C. Oey, A. B. Djurisic, C. Y. Kwong, C. H. Cheung, W. K. Chan, and P. C. Chui. Spectroscopic ellipsometry of the optical functions of some widely used organic light emitting diodes (oleds) materials. In A. C. Arias, N. Tessler, L. Burgi, and J. A. Emerson, editors, *Organic Thin-Film Electronics*, volume 871E, page I9.18.11, Warrendale, PA, 2005. Mater. Res. Soc. Symp. Proc.

[116] Conor Madigan and Vladimir Bulovic. Modeling of exciton diffusion in amorphous organic thin films. *Phys. Rev. Lett.*, 96(4):046404, 2006. URL `http://link.aps.org/abstract/PRL/v96/e046404`.

[117] Conor F. Madigan and Vladimir Bulović. Solid state solvation in amorphous organic thin films. *Phys. Rev. Lett.*, 91(24):247403, Dec 2003.

[118] G. Malpuech, A. Di Carlo, A. Kavokin, J. J. Baumberg, M. Zamfirescu, and P. Lugli. Room-temperature polariton lasers based on gan microcavities. *Appl. Phys. Lett.*, 81(3):412–414, 2002.

[119] G. Malpuech, A. Kavokin, A. Di Carlo, J. J. Baumberg, F. Compagnone, P. Lugli, and M. Zamfirescu. Polariton lasing due to the exciton-electron scattering in semiconductor microcavities. *Phys. Status Solidi A*, pages 181–186, 2002.

[120] G. Malpuech, A. V. Kavokin, and W. Langbein. Theory of propagation and scattering of exciton-polaritons in quantum wells. *Phys. Status Solidi A*, 190 (3):703–707, 2002.

[121] G. Malpuech, D. D. Solnyshkov, H. Ouerdane, M. M. Glazov, and I. Shelykh. Bose glass and superfluid phases of cavity polaritons. *Phys. Rev. Lett.*, 98(20), 2007.

[122] F. M. Marchetti, B. D. Simons, and P. B. Littlewood. Condensation of cavity polaritons in a disordered environment. *Phys. Rev. B*, 70(15), 2004.

[123] F. M. Marchetti, M. H. Szymanska, P. R. Eastham, B. D. Simons, and P. B. Littlewood. Condensation and lasing of microcavity polaritons: comparison between two models. *Solid State Commun.*, 134(1-2):111–115, 2005.

[124] F. M. Marchetti, M. H. Szymanska, J. M. J. Keeling, J. Kasprzak, R. Andre, P. B. Littlewood, and Le Si Dang. Phase diagram for condensation of microcavity polaritons: From theory to practice. *Physical Review B (Condensed Matter and Materials Physics)*, 77(23):235313, 2008. URL `http://link.aps.org/abstract/PRB/v77/e235313`.

[125] Donald W. Marquardt. An algorithm for least-squares estimation of nonlinear parameters. *Journal of the Society for Industrial and Applied Mathematics*, 11 (2):431–441, 1963.

[126] M. M. Melliti, R. Chtourou, J. Block, and V. Thierry-Mieg. Influence of disorder on microcavity polariton linewidths. *Physica E*, 30(1-2):17–20, 2005.

[127] M H Merrill and C T Sun. Fast, simple and efficient assembly of nanolayered materials and devices. *Nanotechnology*, 20(7):075606 (7pp), 2009. URL `http://stacks.iop.org/0957-4484/20/075606`.

[128] Martine. Meyer, Jean Claude. Mialocq, and Bruno. Perly. Photoinduced intramolecular charge transfer and trans-cis isomerization of the dcm styrene dye: picosecond and nanosecond laser spectroscopy, high-performance liquid chromatography, and nuclear magnetic resonance studies. *The Journal of Physical Chemistry*, 94(1):98–104, 1990. URL `http://pubs.acs.org/doi/abs/10.1021/j100364a015`.

[129] P. Michetti and G. C. La Rocca. Polariton states in disordered organic microcavities. *Phys. Rev. B*, 71(11):115320, 2005.

[130] P. Michetti and G. C. La Rocca. Photophysics of j-aggregate microcavities. *Phys. Status Solidi B*, 245(6):1055–1058, 2008.

[131] P. Michetti and G. C. La Rocca. Polariton dynamics in disordered microcavities. *Physica E-Low-Dimensional Systems & Nanostructures*, 40(6):1926–1929, 2008.

[132] P. Michetti and G. C. La Rocca. Simulation of j-aggregate microcavity photoluminescence. *Phys. Rev. B*, 77(19), 2008.

[133] P. Michetti and G. C. La Rocca. Exciton-phonon scattering and photoexcitation dynamics in j-aggregate microcavities. *Phys. Rev. B*, 79(3), 2009.

[134] K. Misawa, H. Ono, K. Minoshima, and T. Kobayashi. New fabrication method for highly oriented j-aggregates dispersed in polymer-films. *Appl. Phys. Lett.*, 63(5):577–579, 1993.

[135] Johannes Moll, Siegfried Daehne, James R. Durrant, and Douwe A. Wiersma. Optical dynamics of excitons in j aggregates of a carbocyanine dye. *J. Chem. Phys.*, 102(16):6362–6370, 1995.

[136] A. Naber, U. C. Fischer, S. Kirchner, T. Dziomba, G. Kollar, L. F. Chi, and H. Fuchs. Architecture and surface properties of monomolecular films of a cyanine dye and their light-induced modification. *J. Phys. Chem. B*, 103(14): 2709–2717, 1999.

[137] Robert Nitsche and Torsten Fritz. Determination of model-free kramers-kronig consistent optical constants of thin absorbing films from just one spectral measurement: Application to organic semiconductors. *Phys. Rev. B*, 70(19):195432–195414, 2004.

[138] D. F. O'Brien. J-aggregation in monomolecular layers of cyanine dyes. *Photogr. Sci. Eng.*, 18(1):16–21, 1974.

[139] K. Ohta and H. Ishida. Comparison among several numerical-integration methods for kramers-kronig transformation. *Appl. Spectrosc.*, 42(6):952–957, 1988.

[140] Michel Orrit, Dietmar Mbius, Urs Lehmann, and Horst Meyer. Reflection and transmission of light by dye monolayers. *J. Chem. Phys.*, 85(9):4966–4979, 1986.

[141] Ekmel Ozbay. Plasmonics: Merging Photonics and Electronics at Nanoscale Dimensions. *Science*, 311(5758):189–193, 2006. URL `http://www.sciencemag.org/cgi/content/abstract/311/5758/189`.

[142] G. Panzarini, L. C. Andreani, A. Armitage, D. Baxter, M. S. Skolnick, J. S. Roberts, V. N. Astratov, M. A. Kaliteevski, A. V. Kavokin, and M. R. Vladimirova. Polariton dispersion and polarisation splitting for quantum well excitons in single and coupled microcavities. *Phys. Status Solidi A*, 164(1): 91–94, 1997.

[143] J. Park, L. D. Fouche, and P. T. Hammond. Multicomponent patterning of layer-by-layer assembled polyelectrolyte/nanoparticle composite thin films with controlled alignment. *Adv. Mater.*, 17(21):2575–+, 2005.

[144] Stanley Pau, Hui Cao, Joseph Jacobson, Gunnar Björk, Yoshihisa Yamamoto, and Atac Imamoğlu. Observation of a laserlike transition in a microcavity exciton polariton system. *Phys. Rev. A*, 54(3):R1789–R1792, Sep 1996.

[145] O. G. Peterson, J. P. Webb, W. C. McColgin, and J. H. Eberly. Organic dye laser threshold. *J. Appl. Phys.*, 42(5):1917–1928, 1971. URL `http://link.aip.org/link/?JAP/42/1917/1`.

[146] C. Peyratout, E. Donath, and L. Daehne. Investigation of pseudoisocyanine aggregates formed on polystyrenesulfonate. *Photochem. Photobiol. Sci.*, 1(2): 87–91, 2002.

[147] R. N. Philp and D. R. Tilley. Exciton polaritons in thin films. *Phys. Rev. B*, 44(15):8170–8180, 1991.

[148] Martin Pope and Charles E. Swenberg. *Electronic Processes in Organic Crystals and Polymers.* Oxford University Press, 1999.

[149] K. Read, H. S. Karlsson, M. M. Murnane, H. C. Kapteyn, and R. Haight. Excitation dynamics of dye doped tris(8-hydroxy quinoline) aluminum films studied using time-resolved photoelectron spectroscopy. *Journal of Applied Physics*, 90 (1):294–300, 2001. URL `http://link.aip.org/link/?JAP/90/294/1`.

[150] M. Richard, R. Romestain, R. Andre, and L. S. Dang. Consequences of strong coupling between excitons and microcavity leaky modes. *Appl. Phys. Lett.*, 86 (7):071916, 2005.

[151] E. Rousseau, M. Van der Auweraer, and F. C. De Schryver. Steady-state and time-resolved spectroscopy of a self-assembled cyanine dye multilayer. *Langmuir*, 16(23):8865–8870, 2000.

[152] Els Rousseau, Marc M. Koetse, Mark Van der Auweraer, and Frans C. De Schryver. Comparison between j-aggregates in a self-assembled multilayer and polymer-bound j-aggregates in solution: a steady-state and time-resolved spectroscopic study. *Photochem. Photobiol. Sci.*, 1(6):395–406, 2002.

[153] M. Saba, C. Ciuti, J. Bloch, V. Thierry-Mieg, R. Andre, L. S. Dang, S. Kundermann, A. Mura, G. Bongiovanni, J. L. Staehli, and B. Deveaud. High-temperature ultrafast polariton parametric amplification in semiconductor microcavities. *Nature*, 414(6865):731–735, 2001.

[154] M. Saba, C. Ciuti, S. Kundermann, J. L. Staehli, and B. Deveaud. Towards a room-temperature polariton amplifier. *Semicond. Sci. Technol.*, 18(10):S325–S330, 2003.

[155] Bahaa E. A. Saleh and Malvin Carl Teich. *Fundamentals of Photonics.* Wiley-Interscience, New York, 1991.

[156] L. Sapienza, A. Vasanelli, R. Colombelli, C. Ciuti, Y. Chassagneux, C. Manquest, U. Gennser, and C. Sirtori. Electrically injected cavity polaritons. *Phys. Rev. Lett.*, 100(13), 2008.

[157] V. Savona, C. Piermarocchi, A. Quattropani, F. Tassone, and P. Schwendimann. Microscopic theory of motional narrowing of microcavity polaritons in a disordered potential. *Phys. Rev. Lett.*, 78(23):4470–4473, 1997.

[158] V. Savona, F. Tassone, C. Piermarocchi, A. Quattropani, and P. Schwendimann. Theory of polariton photoluminescence in arbitrary semiconductor microcavity structures. *Phys. Rev. B*, 53(19):13051–13062, 1996.

[159] P. G. Savvidis, J. J. Baumberg, R. M. Stevenson, M. S. Skolnick, D. M. Whittaker, and J. S. Roberts. Angle-resonant stimulated polariton amplifier. *Phys. Rev. Lett.*, 84(7):1547–1550, 2000.

[160] P. G. Savvidis, L. G. Connolly, M. S. Skolnick, D. G. Lidzey, and J. J. Baumberg. Ultrafast polariton dynamics in strongly coupled zinc porphyrin microcavities at room temperature. *Phys. Rev. B*, 74(11), 2006.

[161] G. Scheibe. *Z. Angew. Chem.*, 49:563, 1936.

[162] P. Schouwink, H. V. Berlepsch, L. Dahne, and R. F. Mahrt. Observation of strong exciton-photon coupling in an organic microcavity. *Chem. Phys. Lett.*, 344(3-4):352–356, 2001.

[163] Claude Schweitzer and Reinhard Schmidt. Physical mechanisms of generation and deactivation of singlet oxygen. *Chemical Reviews*, 103(5):1685–1758, 2003. URL `http://pubs.acs.org/doi/abs/10.1021/cr010371d`.

[164] P. Senellart and J. Bloch. Nonlinear emission of microcavity polaritons in the low density regime. *Phys. Rev. Lett.*, 82(6):1233–1236, 1999.

[165] I. Shcheblykin, A. Sliusarenko, N. Bataev, M. Van der Auweraer, O. Varnavsky, and A. Vitukhnovsky. Degradation of j-aggregates in solutions exposed to light. *Journal of Russian Laser Research*, 20(1):7–15, January 1999. URL `http://dx.doi.org/10.1007/BF02508790`.

[166] M. S. Skolnick, D. M. Whittaker, R. Butte, and A. I. Tartakovskii. Continuous wave stimulation in semiconductor microcavities in the strong coupling limit. *Semicond. Sci. Technol.*, 18(10):S301–S310, 2003.

[167] D. D. Solnyshkov, H. Ouerdane, M. M. Glazov, I. A. Shelykh, and G. Malpuech. Bose glass and superfluid phase transitions of exciton-polaritons in gan microcavities. *Solid State Commun.*, 144(9):390–394, 2007.

[168] D. D. Solnyshkov, I. A. Shelykh, M. M. Glazov, G. Malpuech, T. Amand, P. Renucci, X. Marie, and A. V. Kavokin. Nonlinear effects in spin relaxation of cavity polaritons. *Semiconductors (Translation of Fizika i Tekhnika Poluprovodnikov (Sankt-Peterburg))*, 41(9):1080–1091, 2007.

[169] Jung-Hoon Song, Y. He, A. V. Nurmikko, J. Tischler, and V. Bulovic. Exciton-polariton dynamics in a transparent organic semiconductor microcavity. *Phys. Rev. B*, 69(23):235330–235335, 2004.

[170] J. Spence. Spectral sensitization and special photographic materials for scientific use. *Appl. Opt.*, 11(1):4–12, 1972.

[171] R. Stepniewski, K. P. Korona, A. Wysmolek, J. M. Baranowski, K. Pakula, M. Potemski, G. Martinez, I. Grzegory, and S. Porowski. Polariton effects in reflectance and emission spectra of homoepitaxial gan. *Phys. Rev. B*, 56(23): 15151–15156, 1997.

[172] R. M. Stevenson, V. N. Astratov, M. S. Skolnick, D. M. Whittaker, M. Emam-Ismail, A. I. Tartakovskii, P. G. Savvidis, J. J. Baumberg, and J. S. Roberts. Continuous wave observation of massive polariton redistribution by stimulated scattering in semiconductor microcavities. *Phys. Rev. Lett.*, 85(17):3680–3683, 2000.

[173] F. Stokker-Cheregi, A. Vinattieri, F. Semond, M. Leroux, I. R. Sellers, J. Massies, D. Solnyshkov, G. Malpuech, M. Colocci, and M. Gurioli. Polariton relaxation bottleneck and its thermal suppression in bulk gan microcavities. *Appl. Phys. Lett.*, 92(4), 2008.

[174] Irina A. Struganova, Hyunsoo Lim, and Simone A. Morgan. The influence of inorganic salts and bases on the formation of the j-band in the absorption and fluorescence spectra of the diluted aqueous solutions of tdbc. *J. Phys. Chem. B*, 106(42):11047–11050, 2002.

[175] M. Sudzius, M. Langner, S. I. Hintschich, V. G. Lyssenko, H. Frob, and K. Leo. Multimode laser emission from laterally confined organic microcavities. *Appl. Phys. Lett.*, 94(6), 2009.

[176] A. Tagaya, T. Kobayashi, S. Nakatsuka, E. Nihei, K. Sasaki, and Y. Koike. High gain and high power organic dye-doped polymer optical fiber amplifiers: Absorption and emission cross sections and gain characteristics. *Jpn. J. Appl. Phys. Part 1 - Regul. Pap. Short Notes Rev. Pap.*, 36(5A):2705–2708, 1997.

[177] K. Tani, K. Matsuzaki, Y. Kodama, M. Fukita, T. Kodaira, H. Horiuchi, T. Okutsu, and H. Hiratsuka. Photophysical property of the j-aggregate thin film of an oxacyanine dye prepared by the spin-coating method and enhancement of its photostability by use of polydimethylsilane. *J. Photochem. Photobiol. A-Chem.*, 199(2-3):150–155, 2008.

[178] T. Tani, K. Seki, K. Yoshihara, and J. Hanna. Thin organic layers for photography and electronic devices. *Int. J. Photoenergy*, 2006.

[179] A. I. Tartakovskii, D. N. Krizhanovskii, and V. D. Kulakovskii. Polariton-polariton scattering in semiconductor microcavities: Distinctive features and similarities to the three-dimensional case. *Phys. Rev. B*, 62(20):R13298–R13301, 2000.

[180] A. I. Tartakovskii, D. N. Krizhanovskii, D. A. Kurysh, V. D. Kulakovskii, M. S. Skolnick, and J. S. Roberts. Polariton parametric scattering processes in semiconductor microcavities observed in continuous wave experiments. *Phys. Rev. B*, 65(8), 2002.

[181] A. I. Tartakovskii, V. D. Kulakovskii, D. N. Krizhanovskii, M. S. Skolnick, V. N. Astratov, A. Armitage, and J. S. Roberts. Nonlinearities in emission from the lower polariton branch of semiconductor microcavities. *Phys. Rev. B*, 60(16): R11293–R11296, 1999.

[182] F. Tassone, C. Piermarocchi, V. Savona, A. Quattropani, and P. Schwendimann. Bottleneck effects in the relaxation and photoluminescence of microcavity polaritons. *Phys. Rev. B*, 56(12):7554–7563, 1997.

[183] F. Tassone and Y. Yamamoto. Exciton-exciton scattering dynamics in a semiconductor microcavity and stimulated scattering into polaritons. *Phys. Rev. B*, 59(16):10830–10842, 1999.

[184] F. Tassone and Y. Yamamoto. Lasing and squeezing of composite bosons in a semiconductor microcavity. *Phys. Rev. A*, 62(6):063809, Nov 2000.

[185] Michael Tavis and Frederick W. Cummings. Exact solution for an n-molecule¯radiation-field hamiltonian. *Phys. Rev.*, 170(2):379–384, Jun 1968.

[186] J. R. Tischler, M. S. Bradley, and V. Bulovic. Critically coupled resonators in vertical geometry using a planar mirror and a 5 nm thick absorbing film. *Opt. Lett.*, 31(13):2045–2047, 2006.

[187] J. R. Tischler, M. S. Bradley, Q. Zhang, T. Atay, A. Nurmikko, and V. Bulovic. Solid state cavity qed: Strong coupling in organic thin films. *Org. Electron.*, 8 (2-3):94–113, 2007.

[188] Jonathan R. Tischler. *Solid State Cavity QED: Practical Applications of Strong Coupling of Light and Matter.* Doctor of philosophy, Massachusetts Intitute of Technology, 2007.

[189] Jonathan R. Tischler, M. Scott Bradley, Vladimir Bulovic, Jung Hoon Song, and Arto Nurmikko. Strong coupling in a microcavity led. *Phys. Rev. Lett.*, 95 (3):036401–036404, 2005.

[190] S. I. Tsintzos, N. T. Pelekanos, G. Konstantinidis, Z. Hatzopoulos, and P. G. Savvidis. A gaas polariton light-emitting diode operating near room temperature. *Nature*, 453(7193):372–375, 2008.

[191] Mirjam van Burgel, Douwe A. Wiersma, and Koos Duppen. The dynamics of one-dimensional excitons in liquids. *J. Chem. Phys.*, 102(1):20–33, 1995.

[192] Joseph T. Verdeyen. *Laser Electronics.* Prentice Hall, Upper Saddle River, 1995.

[193] T. Virgili, D. G. Lidzey, M. Grell, S. Walker, A. Asimakis, and D. D. C. Bradley. Completely polarized photoluminescence emission from a microcavity containing an aligned conjugated polymer. *Chem. Phys. Lett.*, 341(3-4):219–224, 2001.

[194] L. Ward. *The Optical Constants of Bulk Materials and Films.* IOP Publishing Ltd., Bristol, UK, 1994.

[195] C. Weisbuch, H. Benisty, and R. Houdre. Overview of fundamentals and applications of electrons, excitons and photons in confined structures. *J. Lumines.*, 85(4):271–293, 2000.

[196] C. Weisbuch, M. Nishioka, A. Ishikawa, and Y. Arakawa. Observation of the coupled exciton-photon mode splitting in a semiconductor quantum microcavity. *Phys. Rev. Lett.*, 69(23):3314–3317, 1992.

[197] J. Wenus, S. Ceccarelli, D. G. Lidzey, A. I. Tolmachev, J. L. Slominskii, and J. L. Bricks. Optical strong coupling in microcavities containing j-aggregates absorbing in near-infrared spectral range. *Org. Electron.*, 8(2-3):120–126, 2007.

[198] J. Wenus, R. Parashkov, S. Ceccarelli, A. Brehier, J. S. Lauret, M. S. Skolnick, E. Deleporte, and D. G. Lidzey. Hybrid organic-inorganic exciton-polaritons in a strongly coupled microcavity. *Phys. Rev. B*, 74(23), 2006.

[199] G. Wrigge, I. Gerhardt, J. Hwang, G. Zumofen, and V. Sandoghdar. Efficient coupling of photons to a single molecule and the observation of its resonance fluorescence. *Nat. Phys.*, 4(1):60–66, 2008.

[200] J. Yu. *Improving OLED Technology for Displays.* Doctoral thesis, Massachusetts Institute of Technology, 2008.

[201] J. Yu and V. Bulovic. Micropatterning metal electrode of organic light emitting devices using rapid polydimethylsiloxane lift-off. *Appl. Phys. Lett.*, 91(4), 2007.

[202] Y. F. Zhu, D. J. Gauthier, S. E. Morin, Q. L. Wu, H. J. Carmichael, and T. W. Mossberg. Vacuum rabi splitting as a feature of linear-dispersion theory - analysis and experimental-observations. *Phys. Rev. Lett.*, 64(21):2499–2502, 1990.

[203] Hashem Zoubi and G. C. La Rocca. Microscopic theory of anisotropic organic cavity exciton polaritons. *Phys. Rev. B*, 71(23):235316, Jun 2005.